LEABHARLANN CHOLÁISTE NA TRÍONÓIDE, BAILE ÁTHA CLIATH | TRINITY COLLEGE LIBRARY DUBLIN
Ollscoil Átha Cliath | The University of Dublin

Terms and Conditions of Use of Digitised Theses from Trinity College Library Dublin

Copyright statement

All material supplied by Trinity College Library is protected by copyright (under the Copyright and Related Rights Act, 2000 as amended) and other relevant Intellectual Property Rights. By accessing and using a Digitised Thesis from Trinity College Library you acknowledge that all Intellectual Property Rights in any Works supplied are the sole and exclusive property of the copyright and/or other IPR holder. Specific copyright holders may not be explicitly identified. Use of materials from other sources within a thesis should not be construed as a claim over them.

A non-exclusive, non-transferable licence is hereby granted to those using or reproducing, in whole or in part, the material for valid purposes, providing the copyright owners are acknowledged using the normal conventions. Where specific permission to use material is required, this is identified and such permission must be sought from the copyright holder or agency cited.

Liability statement

By using a Digitised Thesis, I accept that Trinity College Dublin bears no legal responsibility for the accuracy, legality or comprehensiveness of materials contained within the thesis, and that Trinity College Dublin accepts no liability for indirect, consequential, or incidental, damages or losses arising from use of the thesis for whatever reason. Information located in a thesis may be subject to specific use constraints, details of which may not be explicitly described. It is the responsibility of potential and actual users to be aware of such constraints and to abide by them. By making use of material from a digitised thesis, you accept these copyright and disclaimer provisions. Where it is brought to the attention of Trinity College Library that there may be a breach of copyright or other restraint, it is the policy to withdraw or take down access to a thesis while the issue is being resolved.

Access Agreement

By using a Digitised Thesis from Trinity College Library you are bound by the following Terms & Conditions. Please read them carefully.

I have read and I understand the following statement: All material supplied via a Digitised Thesis from Trinity College Library is protected by copyright and other intellectual property rights, and duplication or sale of all or part of any of a thesis is not permitted, except that material may be duplicated by you for your research use or for educational purposes in electronic or print form providing the copyright owners are acknowledged using the normal conventions. You must obtain permission for any other use. Electronic or print copies may not be offered, whether for sale or otherwise to anyone. This copy has been supplied on the understanding that it is copyright material and that no quotation from the thesis may be published without proper acknowledgement.

Step-induced defects in thin films and the effect on their electrical and magnetic properties

A thesis submitted to the University of
Dublin, Trinity College, in application for
the degree of Doctor of Philosophy
by

Askar Syrlybekov

School of Physics
Trinity College Dublin
March 2015

Ph.D. Physics

Declaration

This thesis is submitted by the under signed for the degree of Doctor in Philosophy at the University of Dublin.

It has been submitted as an exercise for a degree at any other university.

Apart from the advice, assistance and join effort mentioned in the acknowledgment and in the text, this thesis is entirely my own work. I agree that the library may lend or copy this thesis freely on request.

Dedicated to

My parents and family

Acknowledgment

It has been four and half years since I came to Trinity College to start my post-graduate study, during that time I improved my knowledge and skills in the field of nanotechnology and I would like to thank those people who have helped me during the post graduate study.

First of all, I would like to thank my supervisor Prof. Igor Shvets for giving me chance to join in his group. During the whole course of study, he has supported me with advice and suggestions.

Secondly, I would like to thank JSC "Center for International Programs" Ministry of Education and Science of the Republic of Kazakhstan for the stipend.

I am grateful to Dr. Sumesh Sofin and Rafael Ramos, who co-supervised during my first year and taught me how to use most of the experimental techniques used in this work. All of this knowledge help me to push my work in a right direction. I am also thankful to Prof. Mohamed Abid who taught me to make different devices and improved my knowledge to overcome difficulties. Thanks also to Prof. Han-Chun Wu for his fruitful advice on one of my project. I would like to thank Dr. Elisabetta Arca who has worked with me during the last year for the experimental measurements on the samples and giving scientific advice. Dr. Alexander Chaika for providing me with some samples for the electric and transport measurement which I have used in my thesis. Dr. Ruggero

Verre for the training on the AFM and giving ideas to improve the papers. Dr. Karsten for training on the XRD tool and helping me to sort out problems with the LabVIEW programmes. Ozhet with whom I shared an apartment in order to save some money to support my family. Oral for sharing those delicious dining hall lunches every day. Brendan O'Dowd for his help to download different software which made my life easy to write a thesis. David who shared the sputtering system with me even it was helpless. Dr Cormac for the many diverse talks and proof reading this thesis. Dr Tarek and Alan for their training on EBL. Hongjou for showing me how to use milling system. Dr Jose for teaching me how to use electron beam evaporation system and advice in the field of electron beam lithography. Brendan Balfin for his help fixing the high temperature furnace. Leo with whom I shared the cryostat and baking the MBE system. I would also like to thank all group members: Karsten, Elisabetta, Brendan O'Dowd, Brendan Balfin, Daragh, Emma, David, Leo, Bary, Olaf.

Finally, I would like to thank all of the staff of CRANN and School of Physics for doing all the administrative work: Samantha Williams, Robbie Gallagher, Ken Concannon, Mike Finneran and specially Ellen Lennon and Jeanette Cummins.

Summary

This thesis investigates step-induced defects in thin films and their effect on the electrical and magnetic properties. Stepped epitaxial Fe_3O_4 thin films with different thickness were fabricated and their magnetic properties were investigated. The magnetization measurements suggest that the steps induce an additional anisotropy, which has an easy axis perpendicular to steps and the hard axis along the steps. In addition, electrical analysis of a Fe_3O_4 film grown on stepped $SrTiO_3$ substrate revealed anisotropic resistive switching. When the current was directed parallel to the step-edge direction, lower voltages were required to switch to the lower conducting state than the case where current was perpendicular to the step-edges. This is attributed to the high density of anti-phase boundaries present at step edges. In order to control defect densities, a thorough study was carried out to control periodicity and height of the vicinal MgO (100) substrates which is instigated by annealing them at high temperature in air. Furthermore, transport measurements on trilayer graphene synthesized on vicinal cubic-SiC(001), clearly demonstrate that the self-aligned periodic nanodomain boundaries (NBs) induce a charge transport gap.

An investigation was carried out into the faceting of vicinal MgO (100) substrates which have a miscut in the $\langle 010 \rangle$ direction. The process, which results in a highly regular step and terrace structure, is carried out using a simple annealing procedure. It is shown that the periodicity and height of these structures can be controlled through choice of the annealing conditions and

miscut angle. The presence of impurities was examined before and after annealing and the presence of Al contamination, in the post-annealed samples was found to be essential for the formation of the step and terrace structure. The stability of the resultant structures when exposed to ambient conditions is discussed. The cause of the destruction of the surface morphology has been identified and a method to recover the faceted morphology has been proposed.

Chapter 5 examines the magnetic properties of expitaxially grown Fe_3O_4 of varying thickness on the stepped MgO (100) substrates. An anisotropy induced by the presence of the steps was observed which has an easy axis perpendicular to the step edges and hard axis along the step edges. Local transport measurements with nano-gap contacts were performed, with separate measurement investigating current directed both along a single step and perpendicular to a single step. The results suggest that a high density of APBs are formed at the step edges which are responsible for the step-induced anisotropy. Our local transport measurements also indicate that APBs distort the long range charge-ordering of magnetite.

Chapter 6 describes an investigation into a resistive switching (RS) of epitaxial Fe_3O_4 thin films grown on stepped $SrTiO_3$ substrates. We found that the steps induce an anisotropic behavior in resistive switching, where a lower switching voltage is required to switch from the high conducting state to the low conducting state when the electrical field is applied along the step. The anisotropic resistive switching behavior is attributed to the high density of anti-phase boundaries formed at step edges which distort the Verwey transition. Our experimental investigations suggest that the electrical-driven resistive switching in Fe_3O_4 is mainly due to the lattice distortion induced by the external electrical field which modifies the Verwey transition. A large number of switching cycles (I-V measurements) has been demonstrated for the case where the electric field was applied along the steps: more than 9,000 cycles were achieved without damaging the devices.

Chapter 7 deals with trilayer graphene synthesized on vicinal SiC(001)/Si(001) wafer which has a 2° miscut, using Si-atom sublimation. To study the samples' transport properties, devices with hall bar geometry fabricated on trilayer graphene sample. Our transport measurements clearly demonstrate that the GBs induce a charge transport gap larger than 0.7 eV, which agrees well with theory. Moreover, we propose a simple method to achieve a current on-off ratio of 10^4 by opening a transport gap in Bernal stacked trilayer graphene. More remarkably, the transport gap can persist even at 100 K. Our results pave the way to create new electronic nanostructures with high current on-off ratios using graphene on cubic SiC.

Finally, chapter 8 gives a summary of the work and outlines some preliminary results that form the part of potential future investigations.

Publications

1. Han-Chun Wu, Mourad Abid, Ye-Cun Wu, Cormac O Coileain, **Askar Syrlybekov**, Jun Feng Han, Cheng Lin Heng, Huajun Liu, Mohamed Abid and Igor Shvets,

   Enhanced Shubnikov–De Haas Oscillation in Nitrogen-Doped Graphene,

   ACS Nano, 9 (7), 7207–7214, (2015)

2. Han-Chun Wu, Alexander N. Chaika, Tsung-Wei Huang, **Askar Syrlybekov**, Mourad Abid, Victor Yu. Aristov, Olga V., et al.

   Transport Gap Opening and High On-Off Current Ratio in Trilayer Graphene with Self-Aligned Nanodomain Boundaries

   ACS Nano, (Accepted)

3. **Askar Syrlybekov**, Han-Chun Wu, Ozhet Mauit, Ye-Cun Wu, Pierce Maguire, Abbas Khalid, Cormac Ó Coileáin, Leo Farrell, Cheng-Lin Heng, Mohamed Abid, Huajun Liu, Li Yang, Hong-Zhou Zhang and Igor V. Shvets

   Electrical-field-driven metal–insulator transition tuned with self-aligned atomic defects

   Nanoscale, 7, 14055-14061, (2015)

4. Han-Chun Wu, Ozhet Mauit, Cormac O Coileain, **Askar Syrlybekov**, Abbas Khalid, Anas Mouti, Mourad Abid, Hong-Zhou Zhang, Mohamed Abid and Igor V. Shvets

   Magnetic and transport properties of epitaxial thin film $MgFe_2O_4$ *grown on MgO (100) by molecular beam epitaxy*

   Sci. Rep. 4, 7012 (2014)

5. Han-Chun Wu, **Askar Syrlybekov**, Ozhet Mauit, Anas Mouti, Cormac Ó Coileáin, Mourad Abid, Mohamed Abid and Igor V. Shvets
   Magnetic and transport properties of epitaxial stepped Fe_3O_4 *(100) thin films*
   Appl. Phys. Lett. 105, 132408 (2014)
6. **Askar Syrlybekov**, Elisabetta Arca, Ruggero. Verre, Cormac O Coileain, Olzat Toktarbaiuly, Abbas Khalid, Hong-Zhou Zhang and Igor V. Shvets.
   Induced morphological changes of vicinal MgO (100) under high temperature anneal: step formation and surface stability.
   Surf. Interface Anal. (Accepted)

7. Han-Chun Wu, Cormac Ó Coileáin, Mourad Abid, Ozhet Mauit, **Askar Syrlybekov**, Abbas Khalid, Hongjun Xu, Riley Gatensby, Jing Jing Wang, Huajun Liu, Georg S. Duesberg, Hong-Zhou Zhang, Mohamed Abid and Igor V. Shvets
   Tunneling magnetoresistance effect in $Fe_3O_4/MoS_2/Fe_3O_4$ *junctions*
   Sci. Rep. (Submitted)

8. **Askar Syrlybekov**, Elisabetta Arca, Ruggero Verre, Cormac O Coileain, Sumesh Sofin, Rafael Ramos, Olzat Toktarbaiuly, Abbas Khalid, Hong-Zhou Zhang and Igor V. Shvets.
   Faceting of $SrTiO_3$
   (To be submitted to Journal of Applied Physics)

List of Abbreviations:

AS – Along the step

AF – Antiferromagnetic

AFM – Atomic Force Microscope

APB – Anti-phase boundary

APD – Anti-phase domain

ARPES - Angle-resolved photoemission spectroscopy

CCR – Closed cycle refrigeration

EBL – Electron beam lithography

FLG – Few layer graphene

FM – ferromagnetic

GBs – Grain boundaries

MBE – Molecular beam epitaxial

MI – Metal insulator

MIM – Metal insulator metal

PPMS – Physical properties measurement system

PS – Perpendicular to the step

RS – Resistive switching

SE – Step edge

SEM – Scanning electron microscope

TEM – Transmission electron microscope

T_C – Curie temperature

T_V– Verwey transition

UHV – Ultra high vacuum

XRD – X-ray diffraction

XRR – X-ray reflection

LEEM – Low Energy Electron Microscope

LEED – Low Energy Electron Diffraction

VSM – Vibrating sample magnetometer

List of Figures

List of Tables

Contents

3 Experimental tools 32

4 Induced morphological changes on vicinal MgO (100) subjected to high temperature annealing: step formation and surface stability 52

Chapter 1

Introduction

Recently, there has been considerable interest in the growth of magnetic thin films on vicinal surfaces owing to the intriguing physics involved and the technological potential of these films [1-4]. The studies on vicinal surfaces have been carried out mainly to understand the effect of lateral modulation of the electronic structure induced by step edges on the magnetic anisotropies [1, 4]. Moreover, latest studies have shown that the presence of arrays of steps can influence the magnetic, electronic and transport properties of the films grown on top of the vicinal surface [5-7]. Magnetic properties of epitaxial thin films grown on vicinal MgO surfaces attract a lot of attention both from the fundamental and applied points of view [3, 7, 8]. For example, the magnetic anisotropy of a Fe_3O_4 film is affected by the presence of regular atomic step-edge arrays: an anisotropic magnetoresistance (MR) in Fe_3O_4 thin films grown on vicinal MgO (100) substrates is observed. The difference in MR is because of the density of the anti-phase boundaries (APBs) aligned along the atomic step edges [7, 9, 10]. All of these studies have used vicinal substrates where the step height does not exceed a few angstroms and the terrace width is smaller than 30 nm. In order to expand the application of vicinal surfaces they need to be annealed at high temperature. This causes both the step height and terrace width to increase, with the latter able to reach the sub-100nm range [11]. By selectively choosing annealing temperature, the terrace widths (i.e. step densities) and step heights of substrates can be fully controlled.

One of the possible candidates for a stepped surface is vicinal Magnesium Oxide (MgO). MgO is an important technological material. MgO crystallizes in the rock-salt structure with unit cell length of 4.212 Å, it has a wide band gap of 7.8 eV, it is electrically insulating, and it is known for its high melting temperature (above 2800°C). It is also known for being a typical highly ionic oxide, due to the large electronegativity difference between magnesium and oxygen. Due to the basic character of its surface, it has found application in heterogeneous catalysis [12, 13]. It is also very often used as substrate for growth of epitaxial films of metals [14-16], metal oxides [17, 18], resistive switching materials [19, 20], magnetic tunnel junctions (MTJs) [21, 22], high temperature oxide superconductors [23, 24] and ferroelectric pervoskites [25].

Magnetite, Fe_3O_4, is a good candidate for RRAM devices [26]. Fe_3O_4 undergoes a metal–insulator transition at the Verwey temperature (T_V ~ 120 K) [27]. Above T_V, Fe_3O_4 has a cubic structure and is moderately conducting, transforming to a distorted cubic structure below T_V, which is insulating [28]. A. Fursina et al. have shown that epitaxial Fe_3O_4 grown on flat single crystal MgO (100) substrates exhibits resistance switching when a large in-plane electric field is applied [20, 29]. Epitaxial growth of Fe_3O_4 thin films can be readily achieved on MgO substrates due to the small lattice mismatch of −0.34%. The epitaxial growth of Fe_3O_4 on MgO suffers from the formation of (APBs), which are formed as a natural growth defect due to differences in the translational and rotational symmetry between Fe_3O_4 and MgO [30, 31].

Trilayer graphene exhibits distinct electronic properties that are of interest both for fundamental science and for technological applications [32-38]. The ability of graphene to open a band gap is the central problem in this field [39-44]. However, unlike bilayer graphene, trilayer graphene typically exhibits Bernal stacking order and remains metallic upon the application of an electric field perpendicular to the graphene layers [33, 45-48]. On the other hand, grain boundaries (GB), commonly present in graphene [49-54], can remarkably modify the electronic transport [53, 54]. Recent theoretical investigations show that transport gaps can be introduced and tuned by engineering periodic GBs into the graphene layers [55]. However, there is no direct experimental evidence for the existence of a transport gap.

All the above mentioned characteristics make stepped surfaces very interesting templates for research studies from the fundamental point of view as well as for electronic applications. Therefore, it would be interesting to study the effect of stepped surfaces on magnetic and electric properties of a material. The periodicity of stepped surfaces can be controlled which allows the preparation of templates with differing step densities for these studies. The stepped surfaces may play an important role in the electric field breakdown of a material, which can be crucial for the stability of memory devices and reducing the required switching voltage. Moreover, stepped surfaces have shown an anisotropic resistive switching effect, where a lower switching voltage is required to enable the lower conducting state along the steps than that required perpendicular to the steps. This is attributed to the high density of anti-phase boundaries present at step edges. Furthermore, stepped SiC surfaces can be used as a substrates for the growth of trilayer graphene and can induce defects which will can modify its transport properties. Furthermore, stepped surfaces can be used as templates for producing different ordered nanoparticle arrangements of Ag and Au [56, 57], nanostructures [58], and Co and Fe nanowires [59-61].

1.1 Outline of this thesis

Chapter 2: In this chapter we introduce vicinal surfaces and crystal structures of MgO. Further we provide an overview of the general properties of thin film Fe_3O_4. We give a general description of its crystal structure, metal to insulator transition (Verwey transition) and formation of (APBs) when grown on MgO substrates, its magnetization and its resistive switching behaviour. We then give a general introduction to trilayer graphene, along with details of the synthesis and surface structure of trilayer graphene.

Chapter 3: In this chapter we discuss the experimental tools that have been used in this work. In section 3.2 and 3.3 details of the high temperature furnace and MBE system are given. In section 3.4 description of ex-situ and in-situ characterization tools are provided including details of high resolution X-ray diffraction (HRXRD), atomic force microscope (AFM), scanning electron microscope (SEM), transmission electron microscope (TEM), closed cycle refrigeration (CCR), physical property measurement system (PPMS) and finally a description of the various lithography techniques.

Chapter 4: In this chapter we present the results of induced morphological changes of vicinal MgO (100) under high temperature annealing, detailing the step formation and surface stability of MgO. Vicinal MgO (100) single crystal substrates, upon annealing in air, produced regular step and terrace structures on the surface. Samples have been annealed in the temperature range 1100°C-1580°C for 3 hours. Surfaces were characterized by AFM, XRD, TEM, and XPS, in order to assess the roles of contaminants, temperature, and miscut angle on the final morphology. The formation of thick layers of contaminants on the surfaces upon exposure to ambient conditions has been investigated, and a method to recover the faceted morphology has been proposed.

Chapter 5: In this chapter we report the fabrication of different thicknesses of expitaxially grown Fe_3O_4 thin films on step surfaces. Details of their magnetic properties are also presented. The morphology of Fe_3O_4 thin films were characterized by AFM and high resolution STEM. The magnetization measurements show that the steps induce additional anisotropy which has its easy axis perpendicular to steps and the hard axis along the steps. Local transport measurements with nano-gap suggest that the step induced anisotropy is mainly due to APBs formed at the step edges.

Chapter 6: In this chapter we present the anisotropic resistive switching effect of Fe_3O_4 thin film grown on stepped $SrTiO_3$ (100) substrate with the miscut along the <010> direction. Resistive switching effect have been seen below the Verwey temperature. Switching along the steps required lower voltages to switch to the lower conducting state than perpendicular to the steps. This is attributed to the high density of anti-phase boundaries present at step edges. To demonstrate the stability of the devices, a large number of switching cycles (for the electric field applied along the steps) was performed. More than 9,000 cycles were carried out without damaging the devices. Observed differences in resistive switching along the steps and perpendicular to the steps have been discussed.

Chapter 7: In this chapter, we present transport measurements on trilayer graphene synthesized on vicinal cubic-SiC(001). Our transport measurements clearly demonstrate a GB induced charge transport gap of large than 0.7 eV which agrees well with theory. More remarkably, the transport gap can persist even at 100 K. Our results pave the way to create new electronic nanostructures with high current on-off ratios using graphene on cubic SiC.

Chapter 8: In this chapter we conclude the main results of the thesis. We also show the preliminary results of nanoribbons with three layers of $WS_2/MoS_2/WS_2$

on stepped Al_2O_3 substrates. The terrace region was covered by multilayers and step regions were not covered by multilayers.

References

[1] V. Usov, S. Murphy, I.V. Shvets, J. Appl. Phys., 95 (2004) 7312-7314.

[2] B. Degroote, M. Major, J. Meersschaut, J. Dekoster, G. Langouche, Surf. Sci., 482–485, Part 2 (2001) 1090-1094.

[3] B.B. Maranville, A.L. Shapiro, F. Hellman, D.M. Schaadt, E.T. Yu, Appl. Phys. Lett., 81 (2002) 517-519.

[4] A. Encinas, F. Nguyen Van Dau, M. Sussiau, A. Schuhl, and P. Galtiera, J. Appl. Phys. 81, 4482 (1997).

[5] H. Zheng, L. Salamanca-Riba, R. Ramesh, H. Li, Appl. Phys. Lett., 85 (2004) 2905-2907.

[6] R. Ramos, S.K. Arora, I.V. Shvets, J. Appl. Phys., 105 (2009) 07B108.

[7] V.O. Golub, V.V. Dzyublyuk, A.I. Tovstolytkin, S.K. Arora, R. Ramos, R.G.S. Sofin, I.V. Shvets, J. Appl. Phys., 107 (2010).

[8] L. McGuigan, R.C. Barklie, R.G.S. Sofin, S.K. Arora, I.V. Shvets, Phys. Rev. B, 77 (2008) 174424.

[9] S.K. Arora, R.G.S. Sofin, I.V. Shvets, Phys. Rev. B, 72 (2005) 134404.

[10] R.G.S. Sofin, S.K. Arora, I.V. Shvets, J. Magn. Magn. Mater., 316 (2007) e969-e972.

[11] R. Verre, R.G.S. Sofin, V. Usov, K. Fleischer, D. Fox, G. Behan, H. Zhang, I.V. Shvets, Surf. Sci., 606 (2012) 1815-1820.

[12] Jingxia Li , Wei-Lin Dai and Kangnian Fan J. Phys. Chem. C, 112 (2008) 17657-17663.

[13] Gizelle I. Almerindoa, Luiz F.D. Probsta, Carlos E.M. Camposb, Rusiene M. de Almeidac, Simoni M.P. Meneghettic, Mario R. Meneghettic, Jean-Marc Clacensd, Humberto V. Fajardoe, J. Power Sources, 196 (2011) 8057-8063.

[14] R.A. Lukaszew, V. Stoica, C. Uher, R. Clarke, Mater. Res. Soc. Symp. Proc., 648 (2001) p. P3.29.21.

[15] M. Ohtake, F. Kirino, M. Futamoto, Jpn. J. Appl. Phys., 46 (2007) L895.

[16] Y. Nukaga, M. Ohtake, F. Kirino, M. Futamoto, J. Phys.: Conf. Ser., 200, (2010) 072071.

[17] J. Du, S. Gnanarajan, A. Bendavid, Supercond. Sci. Technol., 18 (2005) 1035.

[18] K. Iida, J. Hänisch, S. Trommler, V. Matias, S. Haindl, F. Kurth, I.L.d. Pozo, R. Hühne, M. Kidszun, J. Engelmann, L. Schultz, B. Holzapfel, Appl. Phys. Express, 4 (2011) 013103.

[19] S. Lee, A. Fursina, J.T. Mayo, C.T. Yavuz, V.L. Colvin, R.G. Sofin, I.V. Shvets, D. Natelson, Nat Mater, 7 (2008) 130-133.

[20] A.A. Fursina, R.G.S. Sofin, I.V. Shvets, D. Natelson, Phys. Rev. B, 79 (2009) 245131.

[21] Jia Zhang, Yan Wang, X.-G. Zhang, and X. F. Han, Phys. Rev. B, 82 (2010) 134449.

[22] D.W. Guo, F.A. Cardoso, R. Ferreira, E. Paz, S. Cardoso, P.P. Freitas, J. Appl. Phys., 115 (2014) -.

[23] B. H. Moeckly, S. E. Russek, D. K. Lathrop, R. A. Buhrman, Jian Li, and J. W. Mayer, Appl. Phys. Lett., 57, 1687 (1990).

[24] K.H. Wu, S.P. Chen, J.Y. Juang, T.M. Uen, Y.S. Gou, Physica C: Superconductivity, 289 (1997) 230-242.

[25] R. Ramesh, K. Luther, B. Wikerns, D.L. Hart, E. Wang, J.M. Tarascon, A. Inam, X.D. Wu, T. Venkantesen, Appl. Phys. Lett. 57 (1990) 1505.

[26] R.V. Gudavarthy, A.S. Miller, E.W. Bohannan, E.A. Kulp, Z. He, J.A. Switzer, Electrochimica Acta, 56 (2011) 10550-10556.

[27] N. E.J.W. Verwey, 144 (1939) 327.

[28] G.K. Rozenberg, M.P. Pasternak, W.M. Xu, Y. Amiel, M. Hanfland, M. Amboage, R.D. Taylor, R. Jeanloz, Phys. Rev. Lett., 96 (2006) 045705.

[29] A.A. Fursina, R.G.S. Sofin, I.V. Shvets, D. Natelson, Phys. Rev. B, 82 (2010) 245112.

[30] D.T. Margulies, F.T. Parker, F.E. Spada, R.S. Goldman, J. Li, R. Sinclair, A.E. Berkowitz, Phys. Rev. B, 53 (1996) 9175-9187.

[31] F.C. Voogt, T. Fujii, P.J.M. Smulders, L. Niesen, M.A. James, T. Hibma, Phys. Rev. B, 60 (1999) 11193-11206.

[32] M.F. Craciun, S. Russo, M. Yamamoto, J.B. Oostinga, A.F. Morpurgo, S. Tarucha, Nat Nano, 4 (2009) 383-388.

[33] W. Bao, L. Jing, J. Velasco, Y. Lee, G. Liu, D. Tran, B. Standley, M. Aykol, S.B. Cronin, D. Smirnov, M. Koshino, E. McCann, M. Bockrath, C.N. Lau, Nat Phys, 7 (2011) 948-952.

[34] C.H. Lui, Z. Li, Z. Chen, P.V. Klimov, L.E. Brus, T.F. Heinz, Nano Lett., 11 (2010) 164-169.

[35] C.H. Lui, Z. Li, K.F. Mak, E. Cappelluti, T.F. Heinz, Nat Phys, 7 (2011) 944-947.

[36] T. Taychatanapat, K. Watanabe, T. Taniguchi, P. Jarillo-Herrero, Nat Phys, 7 (2011) 621-625.

[37] F. Zhang, J. Jung, G.A. Fiete, Q. Niu, A.H. MacDonald, Phys. Rev. Lett., 106 (2011) 156801.

[38] L. Zhang, Y. Zhang, J. Camacho, M. Khodas, I. Zaliznyak, Nature Physis, 7 (2011) 953-957.

[39] E.V. Castro, Phys. Rev. Lett., 99 (2007) 216802.

[40] T. Ohta, A. Bostwick, T. Seyller, K. Horn, E. Rotenberg, Science, 313 (2006) 951-954.

[41] Y. Zhang, T.-T. Tang, C. Girit, Z. Hao, M.C. Martin, A. Zettl, M.F. Crommie, Y.R. Shen, F. Wang, Nature, 459 (2009) 820-823.

[42] K.F. Mak, C.H. Lui, J. Shan, T.F. Heinz, Phys. Rev. Lett., 102 (2009) 256405.

[43] J.B. Oostinga, H.B. Heersche, X. Liu, A.F. Morpurgo, L.M.K. Vandersypen, Nat Mater, 7 (2008) 151-157.

[44] F. Xia, D.B. Farmer, Y.-m. Lin, P. Avouris, Nano Lett., 10 (2010) 715-718.

[45] M. Aoki, H. Amawashi, Solid State Commun., 142 (2007) 123-127.

[46] A.A. Avetisyan, B. Partoens, F.M. Peeters, Phys. Rev. B, 80 (2009) 195401.

[47] A.A. Avetisyan, B. Partoens, F.M. Peeters, Phys. Rev. B, 79 (2009) 035421.

[48] K. Zou, F. Zhang, C. Clapp, A.H. MacDonald, J. Zhu, Nano Lett., 13 (2013) 369-373.

[49] P.Y. Huang, C.S. Ruiz-Vargas, A.M. van der Zande, W.S. Whitney, M.P. Levendorf, J.W. Kevek, S. Garg, J.S. Alden, C.J. Hustedt, Y. Zhu, J. Park, P.L. McEuen, D.A. Muller, Nature, 469 (2011) 389-392.

[50] K. Kim, Z. Lee, W. Regan, C. Kisielowski, M.F. Crommie, A. Zettl, ACS nano, 5 (2011) 2142-2146.

[51] V.Y. Aristov, G. Urbanik, K. Kummer, D.V. Vyalikh, O.V. Molodtsova, A.B. Preobrajenski, A.A. Zakharov, C. Hess, T. Hänke, B. Büchner, I. Vobornik, J. Fujii, G. Panaccione, Y.A. Ossipyan, M. Knupfer, Nano Lett., 10 (2010) 992-995.

[52] A. Chaika, O. Molodtsova, A. Zakharov, D. Marchenko, J. Sánchez-Barriga, A. Varykhalov, I. Shvets, V. Aristov, Nano Res., 6 (2013) 562-570.

[53] A.N. Chaika, O.V. Molodtsova, A.A. Zakharov, D. Marchenko, J. Sánchez-Barriga, A. Varykhalov, S.V. Babenkov, M. Portail, M. Zielinski, B.E. Murphy, S.A. Krasnikov, O. Lübben, I.V. Shvets, V.Y. Aristov, Nanotechnol., 25 (2014) 135605.

[54] A.W. Tsen, L. Brown, M.P. Levendorf, F. Ghahari, P.Y. Huang, R.W. Havener, C.S. Ruiz-Vargas, D.A. Muller, P. Kim, J. Park, Science, 336 (2012) 1143-1146.

[55] O.V. Yazyev, S.G. Louie, Nat Mater, 9 (2010) 806-809.

[56] R. Verre, K. Fleischer, O. Ualibek, I.V. Shvets, Appl. Phys. Lett., 100 (2012) 031102.

[57] R. Verre, K. Fleischer, J.F. McGilp, D. Fox, G. Behan, H. Zhang, I.V. Shvets, Nanotechnol., 23 (2012) 035606.

[58] S. Benedetti, L. Gragnaniello, M. Franchini, P. Torelli, S. Valeri, Superlattices Microstruct., 46 (2009) 153-158.

[59] A. Ueda, R.R. Mu, V.C. Saunders, T.C. Livingston, M.H. Wu, D.O. Henderson, in: Surf. Eng., John Wiley & Sons, Inc., 2002, pp. 35-42.

[60] D. Fox, R. Verre, B.J. O'Dowd, S.K. Arora, C.C. Faulkner, I.V. Shvets, H.Z. Zhang, Prog Nat Sci, 22 (2012) 186-192.

[61] S.K. Arora, O'Dowd, B. J. Polishchuk, D. M. Tovstolytkin, A. I. Thakur, P. Brookes, N. B. Ballesteros, B. Gambardella, P. Shvets, I. V., J. Appl. Phys., 114 (2013) 133903.

Chapter 2

Physical property of vicinal surfaces, Fe_3O_4 and trilayer graphene

2.1 Vicinal surfaces

Vicinal surfaces consist of atomically flat terraces separated by atomic steps (see Figure 2.1 (A)). The vicinal surfaces are prepared when a substrate is cut with a small angle **θ** from a low Miller-index plane such as the (100), (110), (111) etc. The vicinal surface consists of periodic terraces **L** that are separated by steps of atomic height **h**. The terrace width distribution is usually narrower for larger miscut angles. In the case of a cubic (100) substrate, the miscut direction can be either the <100> or <110> direction.

Prior to annealing, the vicinal surfaces have a denser distribution of monoatomic steps, in proportion with the miscut angle. During high temperature annealing, the steps gather together, and as a consequence, the higher the miscut angle, the higher the final step height is (Figure 2.1 (B)) [1]

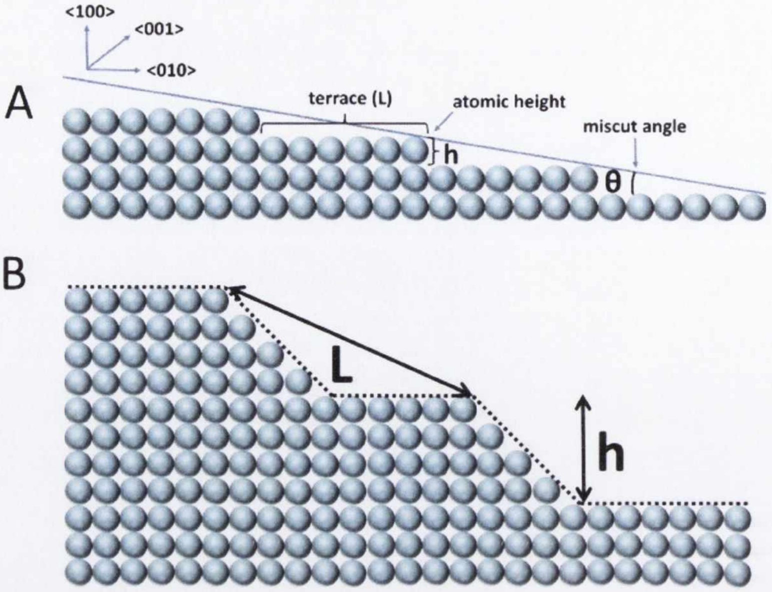

Figure 2.1 (A) Geometric parameters for a vicinal surface: the terrace width **L**, the step height **h** and the miscut angle **θ**, (B) After high temperature annealing of vicinal substrate.

2.2 Crystal structure of MgO

As shown in Figure 2.2 Magnesium oxide (MgO) crystallizes in the rock salt structure with lattice constant equal to 4.21 Å, and belongs to the space group Fm3m. This is close to half the lattice parameter of magnetite (a= 8.398 Å). Therefore, the lattice mismatch with magnetite is only -0.30 % which makes MgO a suitable substrate for the growth of Fe_3O_4 films. Due to the common face-centred cube (fcc) oxygen sub-lattice, magnetite can be grown expitaxially on MgO substrates. In this work, stepped MgO (100) substrates miscut along the <010> direction have been used for the growth of Fe_3O_4 (100) epitaxial thin films.

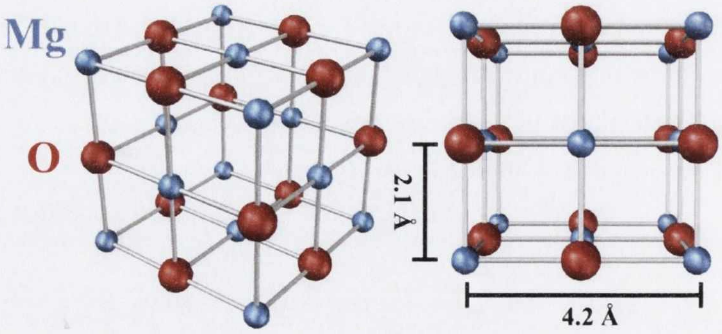

Figure 2.2 3D view of the unit cell of MgO containing oxygen and magnesium atoms.

2.3 Properties of epitaxial Fe_3O_4 films

2.3.1 Applications

Epitaxial magnetite films are a good candidate material for planar magnetic and memristor device applications [2-4]. It has physical properties that deviate from those of the bulk, such as magnetoresistance (MR) and magnetization which does not saturate in high magnetic fields [5-7]. Moreover, anisotropic magnetoresistance has been observed in Fe_3O_4 thin films grown on vicinal MgO (100) substrates [8-10]. This is because the density of the APBs aligned along the atomic step edges. Furthermore, resistive switching effects have been observed in epitaxial Fe_3O_4 thin films grown on flat MgO substrates [11-15].

2.3.2 Crystal structure of Fe_3O_4

Magnetite crystallizes in the inverse spinel structure AB_2O_4 with a lattice constant of a=0.8397 nm and it belongs to the space group Fd3m. The unit cell of Fe_3O_4 includes 4 formula units consisting of 32 O^{2-} anions and 24 $Fe^{2+, 3+}$ cations. The 32 oxygen anions form a face-centred cubic(fcc) lattice that contains 64 tetrahedral A sites which are occupied by Fe^{3+} cations and 32 octahedral B sites which are occupied in equal amounts by Fe^{2+} and Fe^{3+} cations (see Figure 2.3).

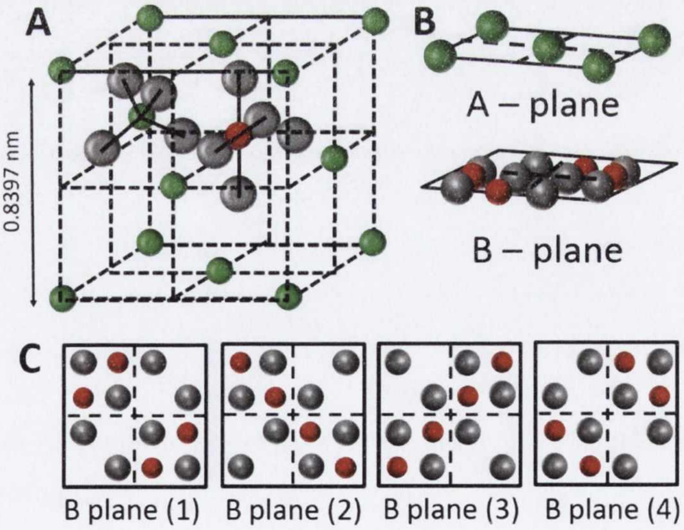

Figure 2.3: (A) 3D view of the unit cell of Fe_3O_4 containing 32 oxygen anions (black) 16 octahedral iron ions (red) and 8 tetrahedral iron ions (green). (B) Tetrahedral iron (Fe_A) in the A-

plane, a octahedral iron (Fe_B) in the B-plane. Four possible types of surface termination in B-plane Reproduced from [16].

Normal spinels are formed when 1/8 of the A sites are occupied by 8 divalent ions and 1/2 of the B sites are occupied by 16 trivalent ions. Instead, in magnetite, 8 of the 16 Fe^{3+} ions in the unit cell are placed in A sites, whereas the other 8, together with the 8 Fe^{2+} ions occupy the B sites in the inverse spinel structure. One uint cell consist of four layers, each layer having the oxygen anions plus the octahedral iron ions. The tetrahedral sites are located halfway between these layers.

2.3.3 Verwey transition.

One of interesting phenomena of magnetite is the transition from metal to insulator at around 125 K, known as Verwey transition. At the Verwey transition temperature (T_V) the structure of magnetite distorts from its cubic symmetry [17] and a charge ordering occurs at the B site [18] therefore decreasing the conductivity. The electrical resistivity of stoichiometric magnetite crystals suddenly increases by an order of magnitude at the Verwey transition temperature. Other properties of the crystal such as magnetization, thermal expansion and heat capacitance also exhibit a sudden variation at T_v [19]. Even though it has been investigated for a long time, this transition is still a matter of discussion and controversy [20-22]. To explain the electronic transfer mechanism below and after Verwey transition, and the sudden change in conductivity at the transition point, different theoretical models have been proposed [17, 20, 23]. Four different mechanisms are proposed in the literature. The first one proposes the charge ordering of Fe^{+2} and Fe^{+3} on the same octahedral planes and it is supported by nuclear magnetic resonance (NMR) data [24, 25]. The second hypothesis suggests ordering of electrons in the Fe_B sites in terms of condensation of phonons, and is supported by X-ray resonant scattering data [26, 27]. However, both hypotheses did not provide enough evidence to give a full explanation of the mechanisms of the Verwey transition. The third proposed hypothesis is the charge density transfer; a transition from inverse to normal spinel, characterized by a specific temperature, $T_{CC,}$ and the last one is the first order structure phase transition, from cubic to a distorted-cubic phase characterized by a specific transition temperature designated T_{dist} [28]. All hypotheses did not show enough evidence to give a conclusive description of the mechanism of the Verwey transition; lots of experiments and work are needed to explain the exact mechanism.

2.3.4 Electronic structure

A pictorial representation of the orbital splitting of the octahedral B site of magnetite is shown in Figure 2.4 (A) [29]. The five degenerate d-electron levels of the Fe ions are split by the crystal field, Δ_{cf}, into three degenerate t_{2g} and two degenerate e_g levels. The t_{2g} and e_g levels are occupied by Fe^{2+} and Fe^{3+} ions' five electrons. The extra electrons of the Fe^{2+} ion occupy the minority t_{2g} band, which is the only band located at the Fermi energy (E_f), giving rise to the half metallic behaviour of magnetite. At room temperature, the conductivity of Fe_3O_4 is ascribed to the hopping of electrons between B sites and A sites. However, at low temperatures, below the Verwey temperature, charge ordering occurs, opening a gap at the Fermi energy, thus a metal-insulator transition occurs. The majority spin-down band and minority spin-up band are split by an exchange energy Δ_{ex}.

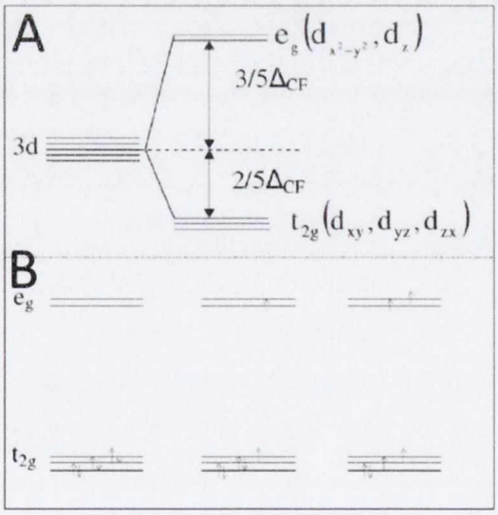

Figure 2.4 Schematic view of the splitting of the 5d electronic orbitals of an isolated iron ion in an octahedral crystal field [29].

2.3.5 Formation of anti-phase boundaries (APBs)

The properties of epitaxial Fe_3O_4 films differ from those of the bulk with thin films having a large electrical resistivity [30], magneto resistance [6, 31] and magnetization which does not saturate in high magnetic fields [32]. These differences are due to the presence of antiphase boundaries (APBs) which are natural defects occurring during growth of Fe_3O_4/MgO thin films [33]. In the first stage of the growth, islands of Fe_3O_4 are deposited on MgO. However, because of the difference in the unit cell parameter and crystal symmetry, the different islands can be related by a shift vector, which is not a lattice translation vector [32, 34]. Fe_3O_4 grows expitaxially on MgO in a layer-by-layer growth mode, where one layer consists of 1/4 of the Fe_3O_4 unit cell [35]. APBs are formed when islands of Fe_3O_4 on the MgO surface coalesce and the neighbouring islands are shifted with respect to each other [36]. The structure at the boundary is determined by the type of shift with respect to the plane of the boundary; whether the shift is parallel or perpendicular to the boundary plane. The oxygen sub-lattice is more or less undisturbed across the APBs and only the cation lattice is shifted. The APB shifts in these films are a consequence of two distinct forms of symmetry breaking between MgO and Fe_3O_4. The first is due to the lattice parameter of MgO (0.4213nm) being half that of Fe_3O_4 (0.8397nm) and because of this, adjacent Fe_3O_4 monolayers may be shifted by 1/4<110>, 1/4<1-10> or 1/2 <100> which are called in-plane shifts (see Figure 2.5 and 2.6). Growth from regions on the MgO substrate separated by a step height of half a unit cell of MgO (0.2106 nm) can also give rise to these shifts [33]. The other APB shifts are a result of the lower symmetry of Fe_3O_4 monolayers compared to the MgO substrate surface. Therefore, adjacent Fe_3O_4 islands on the same MgO surface may be rotated by 90°, as shown in Figure 2.7. APB domain size in Fe_3O_4 has been studied in detail by transmission electron microscopy (TEM) [37]. It has been shown that domain size increases significantly with film thickness, showing a parabolic relation domain size $\mathbf{D} \sim \sqrt{t}$ where t is the deposition time which is proportional to the thickness of the film.

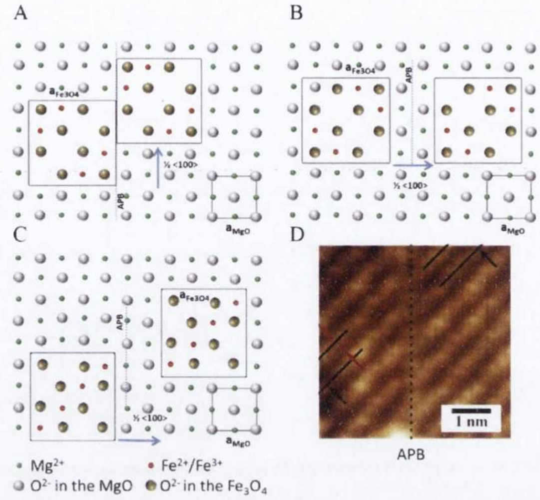

Figure 2.5 Schematic of antiphase boundaries (APBs) formed due to 1/2 <100> type of in-plane shift (A) shift parallel to boundary plane (B) shift perpendicular to the boundary plane. Reproduced from [38]. (C) Possible surface atomic configuration around an APBs with a 1/2 <100> shift where shown in the STM image (D). The boundary at which the two nucleation domains meet and form the APB is indicated by the dashed line [16].

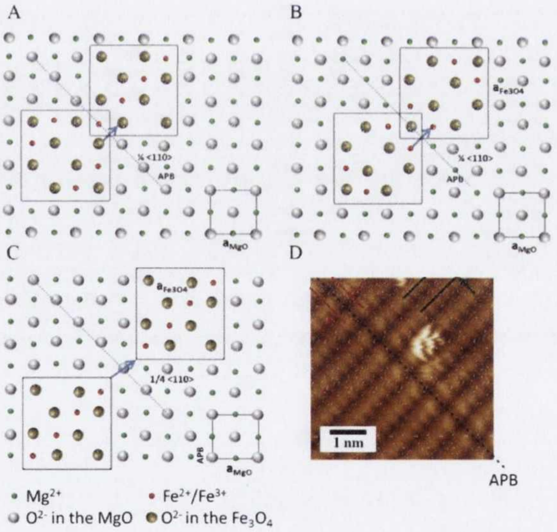

Figure 2.6 Schematic of antiphase boundaries (APBs) formed due to 1/4 <110> type of in-plane shift (A) shift parallel to boundary plane (B) shift perpendicular to the boundary plane. Reproduced from [38]. (C) Possible surface atomic configuration around an APBs with a 1/4 <110> shift where shown in the STM image (D). The boundary at which the two nucleation domains meet and form the APB is indicated by the dashed line [16].

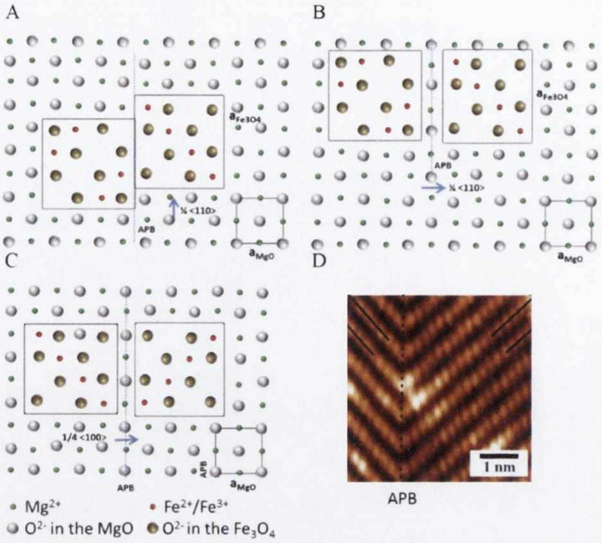

Figure 2.7 Schematic of antiphase boundaries (APBs) formed due to 1/4 <101> type of out-plane shifts (A) 1/4 <100> shift parallel to boundary plane (B) 1/4 <100> shift perpendicular to the boundary plane. Reproduced from [38]. (C) Possible surface atomic configuration around an APBs with a 1/4 <100> shift where shown in the STM image (D). The boundary at which the two nucleation domains meet and form the APB is indicated by the dashed line [16].

2.4 Magnetic hysteresis

2.4.1 Introduction

The term hysteresis came from Greek "hysteresis" – lag, delay e.i. the value describing some physical process is dependent on an external parameter. We can find the word hysteresis in electricity, magnetism and thermodynamics where it has a sign of a first-order phase transition.

2.4.2 Ferromagnetic materials

Fe, Fe_3O_4, Co, Ni and so on show a unique magnetic behavior which is called ferromagnetism. When an external magnetic field is applied to a ferromagnet, the atomic magnetic moments line up parallel with each other in a region called a domain and when the field is removed, it will not go back to zero magnetization. Ferromagnetic materials have a critical temperature, called the Curie temperature where the ferromagnetic properties of the system can no longer maintain a spontaneous magnetization, so its ability to be magnetized to a magnet disappears because of thermal agitation.

2.4.3 Hysteresis loop

Figure 2.8 shows hysteresis in ferromagnetic material. The x-axis show magnetic field strength **H** while the y-axis show degree of magnetization M. When the magnetic field is not applied, there is no magnetization and once a magnetic field is applied, the ferromagnetic material will become magnetic. Let us consider that a sample is unmagnetized, i.e. M and H are zero, as H increases from zero, M increases as shown by the red dashed curves in Figure 2.8. This calls magnetization M process where almost all of the magnetic domains are aligned along the applied field and it reaches saturation value called saturation magnetization M_S at saturation field H_{SAT}. When the field is decreased to zero the sample still keeps certain value of magnetization which is called remanence Mr. The magnetization goes back to zero at applied field $-H_C$ (coercivity of material) when magnetic field applied in opposite direction. Further increasing the magnetic field will saturate magnetic domains along the applied field. The ratio Mr/Ms is also called squareness ratio (SQR) and it measures how square the hysteresis loop is and it is used to differ the anisotropy shape as well.

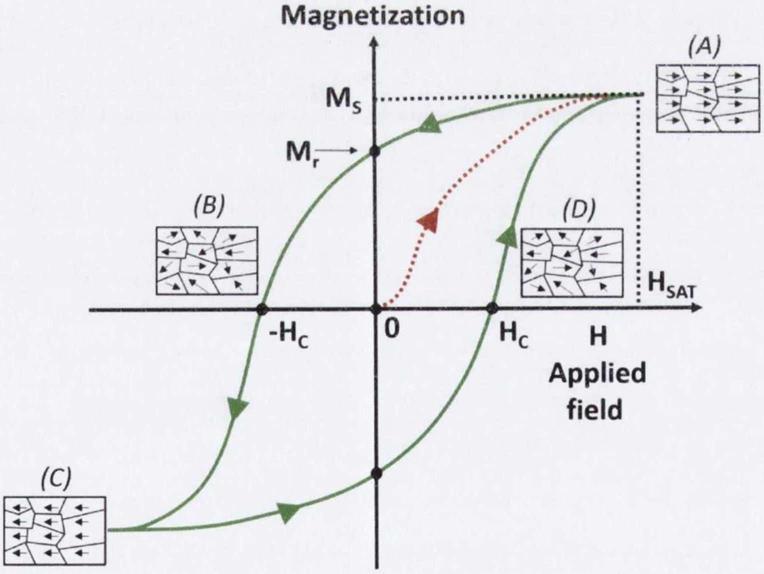

Figure 2.8 Hysteresis curves for a ferromagnetic material: Magnetization M vs applied field H

2.4 Resistive switching

2.4.1 Introduction

The resistance switching behaviour of several materials has recently attracted considerable attention for its application in non-volatile memory (NVM) devices. This phenomena have been observed in many metal oxides: binary transition metal oxides NiO [39-41], TiO_2 [42, 43] and ZnO [44, 45] in addition to perovskite-type oxides such as $SrTiO_3$ [46, 47] and $SrZrO_3$ [48, 49]. A resistive random access memory (RRAM) is a type of non-volatile memory (NVM). Interest in materials showing this technologically interesting behaviour for information storage is huge because of the potential high information density and low-cost of NVM made from these materials.

2.4.2 Classification

Resistive switching (RS) is a phenomenon where the resistance of a material changes dramatically due to application of a current or voltage. Therefore, resistance states of these materials can be divided into two bistable states: a high resistance state (HRS) and a low resistance state (LRS). Resistive switching behaviour can be classified into two types: (1) unipolar resistive switching (URS) and (2) bipolar resistive switching (BRS) (see Figure 2.9). The URS operation is not dependent on the applied voltage polarity, so that the set and reset switching is only due to the magnitude of the applied voltage. The set voltage is always higher than the reset voltage, and reset current is always higher than the compliance current (CC) during the set operation. In contrast to URS, BRS depends on the applied voltage polarity. If the reset switching occurs under one voltage polarity, the set switching will occur under the other polarity.

Resistive switching is used in two configurations: (A) sandwich and (B) planar as shown in Figure 2.10. Sandwich type of structure where metal oxide or insulator placed between top and bottom electrode. This method is used in most cases to observe resistive switching because of easy preparation of the device. Planar resistive switching is also observed in metal oxide materials where two electrodes are placed on top of an insulator. Planar resistive switching is trickier, because of the small gap between the two electrodes.

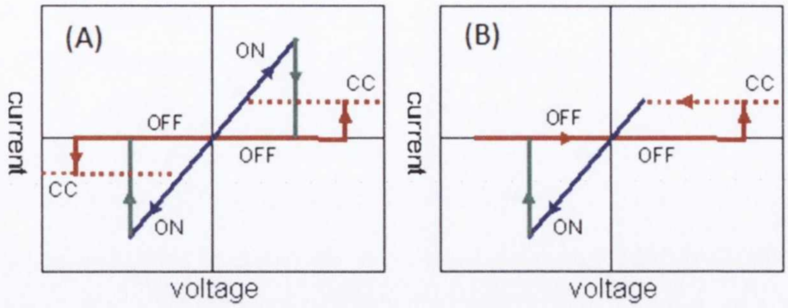

Figure 2.9: Two types of resistance switching behaviours: (A) Unipolar RS, (B) Bipolar RS.

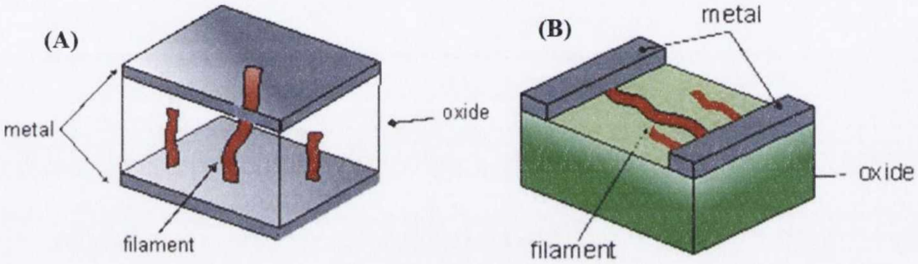

Figure 2.10: Geometric location of metal oxide resistive switching in metal-insulator-metal (MIM) structure: (A) Sandwich configuration; (B) Planar configuration.

2.4.3 Resistive switching in Fe_3O_4

A resistive switching mechanism also has been seen in magnetite: there is a switching from a high-resistance state before the switching voltage (V_{sw}) to a low-resistance above switching voltage (see Figure 2.11). The resistive switching phenomenon in magnetite is different to the unipolar and bipolar classifications because of the shape of the hysteresis in I-V curve. As mentioned above, bipolar resistive switching persists at the low resistance state once it forms conducting filaments in the metal oxide. However, in the magnetite there is no forming filament which could keep the low resistance state after switching the resistance of the sample into low resistance state. Therefore, the low resistance state in magnetite will remain in a certain voltage range. It means at zero applied voltage the resistance of the sample goes back to high resistance state.

In Figure 2.11 (B) an I-V measurement is shown in a magnetite sample where sweeping happens when voltage is swept from 0 V to a certain voltage and back to 0 V again. Point A indicates that switching takes place at a certain voltage denoted as V_{on}. At that point the resistance of the sample dramatically changes from the high resistance state to the low resistance state. Note that we limited the current with a compliance current in order to protect the device from damage caused by the large, sudden increase in the amount of current flowing through it when it switches to the low resistance state. When switching happens, Joule heating due to large current flow leads to heating of the sample. This heating of the sample destroys the device. Therefore, it needs to be protected by limiting the current with a compliance current. At point B switching goes back to the high resistance state (V_{off}). In conclusion, one can say that in the magnetite system there is essentially no memory effect. The low resistance state does not persist without application of a high voltage.

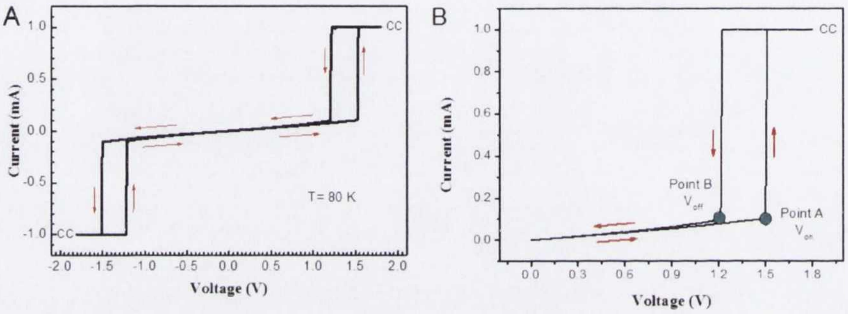

Figure 2.11 Resistive switching in Fe_3O_4 at 80 K (A) I-V measurement demonstrated at both polarities (B) demonstrated switching point A and B respectively.

2.5 Trilayer graphene on SiC(001) substrate

2.5.1 Introduction

With the dramatic progress in research on graphene, recent studies have been devoted to mono-, bi-, and few-layer graphene [50-52]. In few-layer graphene (FLG), the crystallographic stacking of the individual graphene sheets provides an additional degree of freedom [53, 54]. The different stacking orders in FLG have been predicted to strongly influence the electronic properties [55, 56], the band structure [57], magnetic state [58] and spin-orbit coupling [59]. There are two stable crystallographic configurations for graphene trilayer: ABA and ABC stacking order [55, 56].

Graphene-based materials have attracted great interest because of their unique electronic properties and potential for novel applications. They are promising candidates for non-silicon-based nanoelectronic devices [60, 61]. However, in order to be considered as a potential candidate to replace silicon in electronics, graphene should be grown on large area insulating substrates compatible with existing lithographic technology.

SiC(001) thin films grown on standard Si(001) wafers are appealing substrates for growth of low-cost graphene layers for electronic technologies. The large size SiC(001)/Si(001) wafers are cheap and commercially available, e.g., in USA and Japan. It has been shown recently that graphene can be synthesized on cubic SiC(001) wafers using the vacuum sublimation of silicon atoms similar to synthesis on very expensive single crystalline wafers of hexagonal SiC [77]. Therefore, synthesis on low-cost SiC(001) thin films can represent a new method for mass producing graphene layers suitable for electronic applications [62, 63]. However, the graphene layers on the SiC(001) surface have to be continuous and uniform on a wafer scale for potential applications.

2.5.2 Surface structure of trilayer graphene on cubic SiC(001)/Si(001) substrate

Figure 2.12 (A) shows a typical LEEM micrograph of the graphene synthesized on cubic-SiC(001) surface demonstrating intrinsic SiC(001) grain boundaries and uniform contrast throughout the probed 20×20 μm^2 surface area [63]. The uniform contrast on Figure 2.12 (A) proves that despite all the defects of the starting cubic-SiC substrate, the thickness of the synthesized graphene is uniform across the probed surface area [64]. Figure 2.12 (D) shows the number of graphe layers from the reflectivity curves where three distinct minima pick in reflectivity which coresponds three layer of graphene and it does not exced more than three layers. Morevoere, it shows that grpahene covers whole surface uniformaly where the thicknesses measured in different regions. Micro-LEED patterns taken from the Figure 2.12 (C) shows in the Figure 2.12 (E) and (F) that the 12 double-split spots originate from different micrometerscale surface areas producing 90°-rotated micro-LEED patterns with 12 non-equidistant spots. Therefore, Figure 2.12 (B) reveals 12 double - split diffraction spots from graphene layer and SiC layer taken from the large area of Figure 2.12 (A).

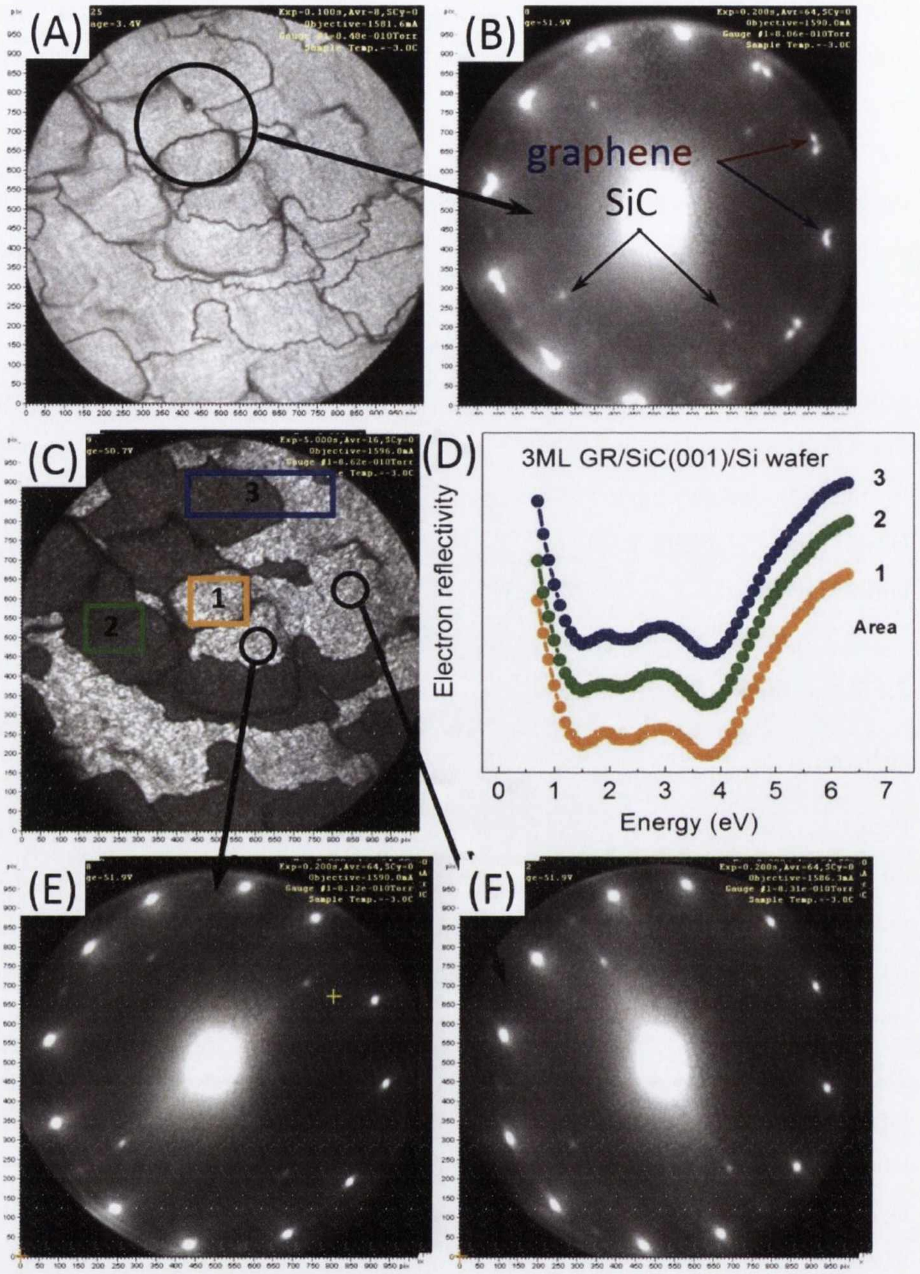

Figure 2.12 (A) 20 µm LEEM micrograph, showing the uniform thickness of the graphene synthesized on SiC(001)/Si(001) wafers. (B), (E) and (F) Micro-LEED patterns from the surface areas shown in panels (A) and (C). Electron reflectivity spectra recorded for the different surface regions 1, 2 and 3 as labelled in panel (C), where the number of dips in the spectra identifies regions 1–3 as trilayer graphene [65, 66]

As STM experiments demonstrate (Figure 2.13), the dark lines (pointed by red arrows in the image in Figure 2.13 (A)) are the anti-phase domain (APD) boundaries separating the systems of nanodomains with elongation in the [110] and $[1\bar{1}0]$ directions. Figure 2.13 (A) reveals horizontal and vertical nanoribbonson the left and right side of the APD boundary, as zooms of the areas shown in Figure 2.13 (C and D) illustrate.

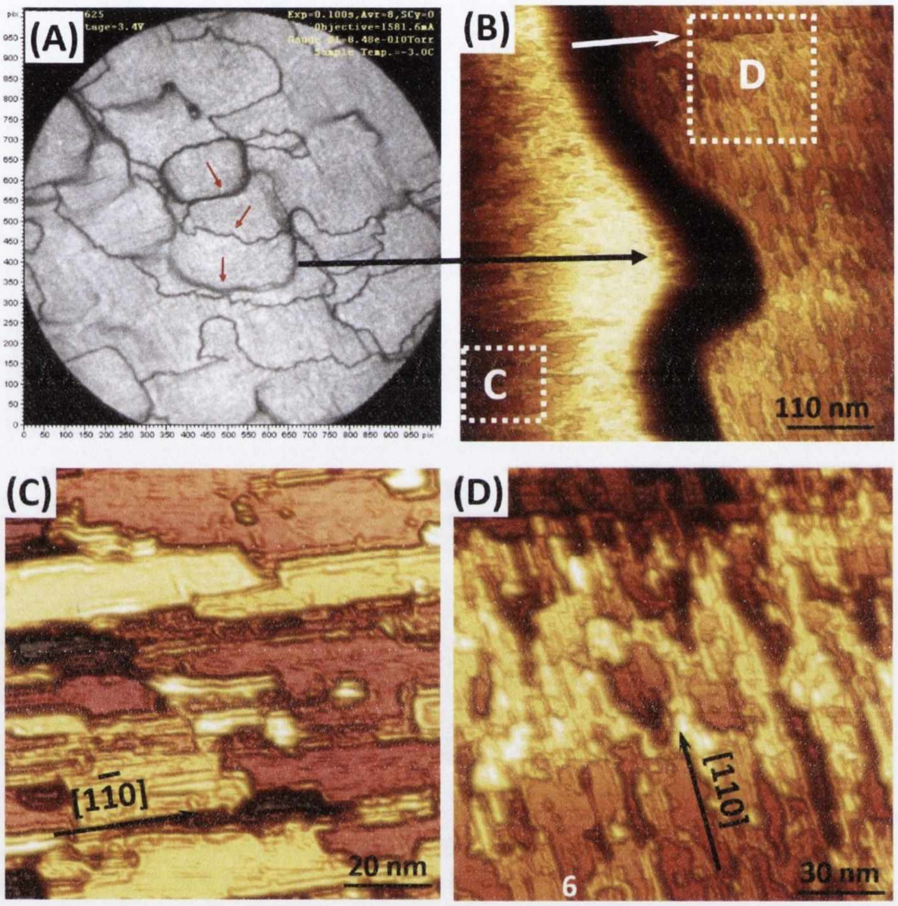

Figure 2.13 (A) 20×20 μm LEEM micrograph of the graphene synthesized on SiC(001)/Si(001) wafers (B) Large area STM images of graphene/SiC (001). STM images of horizontal (B) and vertical (C) nanoribbons on the left and right side of the APD boundary indicated by squares B and C in panel (A), respectively [63, 67]

Large area STM images measured in different areas of several graphene/SiC(001) samples show that the top graphene layer on SiC(001) consists of nanodomains which are typically elongated in either the [110] or $[1\bar{1}0]$ direction, have widths in the range of 5–30 nm and lengths varying from 20 to 200 nm (see Figures 2.13 (B and C)). The average width of these nanodomains is approximately 10 nm, although wider nanoribbons were frequently observed (Figures 2.13 (C and D)). According to STM studies [78,80], individual domains possess a rippled morphology, which leads to a root mean square roughness of 1.7 Å and 2.5 Å, respectively. Detailed STM analysis [63] proved that fabricated trilayer graphene/SiC(001) possesses all the properties of the quasi-freestanding graphene weakly interacting with the substrate (rippling, picometer distortions of the honeycomb lattice, etc.).

The micro-LEED pattern taken from a 5 μm area shown in Figure 2.13 (A) revealed four types of domains, which are responsible for the 24 diffraction spots from the graphene layer and well resolved spots from the SiC (001) substrate (Figure 2.14 (C)). The 6 diffraction spots from graphene in **A'** side and and another 6 diffraction spots from graphene **A** side in Figure 2.14 (A) make total 12 difraction spots. These two domains rotated by ±13.5° from the [110] axis produce two hexagons of spots indicated as red and blue in Figure 2.14 (A) rotated by 27° with respect to each other. Another two domains rotated by ±13.5°from the [1$\bar{1}$0] axis produce another 12 spots marked by green and brown hexagons in Figure 2.14 (B) [63]. The micro-LEED patterns from these two domain systems are rotated by 90 degrees, as can be seen from Figure 2.13 (C) and (D). The sum of these patterns produce the micro-LEED pattern with 12 double split spots as schematically shown in Figure 2.14 (C).

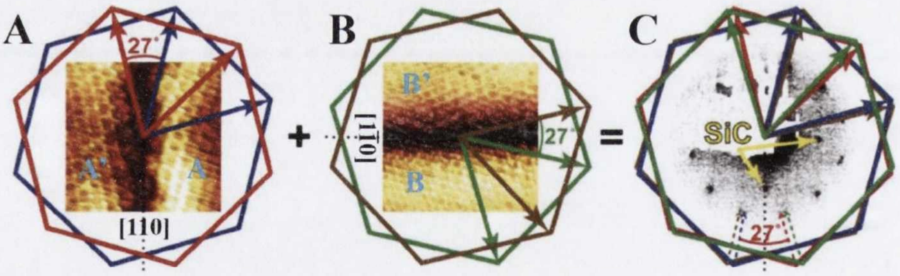

Figure 2.14. **(A-C)** STM images of the domains with the 27°-rotated graphene lattices and the model explaining 12 double spot in LEED patterns taken from graphene/SiC(001) shown in Figure 2.13. The four different colored hexagons, red, blue, green and brown represent the four domain orientations (C) LEED pattern taken from a ,millimetre-sized surface area [63, 67]

2.5.3 Transport properties across grain boundaries in graphene.

The formation of rotated domains and grain boundaries can modify the electronic properties of graphene and lead to the opening of a transport gap [68], which is crucial for technological applications. Grain boundaries, intrinsic topological defects of polycrystalline materials [69], are expected to markedly alter the electronic transport in graphene. Moreover, grain boundaries (GB) in graphene [62, 63, 67, 70-72], can amend the electronic transport in graphene [67, 72]. Recent theoretical study show that transport gaps can be introduced and changed by GBs which present in the graphene layers [68]. Yazyev and Louie [68] have shown that grain-boundary periodicity and its orientation with respect to the crystalline lattices of the two domains of graphene was enough to draw a conclusion about the possible presence of a transport gap. Therefore, perfectly reflecting grain-boundary defects are related to the lattice mismatch at the boundary line. The system reveals an extraordinarily large transport gap of 1.04 eV (Figure 2.15 B), in good agreement with Eg = 1.1 eV obtained. Such periodic grain-boundary structures (class II) which is shown in Figure 2.15 (B) are characterized by a transport gap from equation 1. Which depends exclusively on the periodicity d along the boundary

$$E_g = \hbar v_F \frac{2\pi}{3d} \approx \frac{1.38}{d\,nm}(eV) \tag{1}$$

In conclusion they said that the possibility of introducing class II grain boundaries characterized by large transport gaps into graphene may find important practical applications.

In the graphene synthesized on SiC(001) (Figure 2.13) there are two preferential orientations of the nanodomain boundaries (which are close to the [110] and [$1\bar{1}0$] directions). Using vicinal SiC(001) substrate for graphene synthesis appears to be a promising way to select one of them. In this case, the presence of one preferential direction of the domain boundaries can lead to more uniform domain boundary structure and the opening of the transport gap in graphene synthesized on low-cost, technologically relevant substrate.

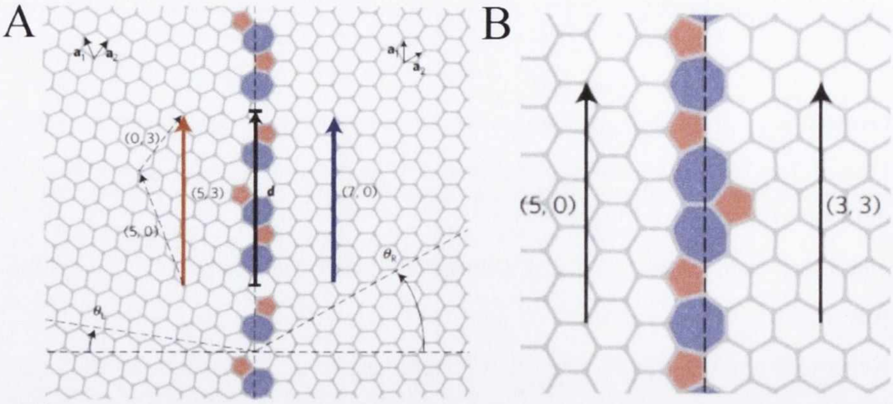

Figure 2.15 Structure of grain boundaries in graphene. (A) An example of a tilt grain boundary in graphene separating two crystalline domains rotated by $\boldsymbol{\theta} = \boldsymbol{\theta}_L + \boldsymbol{\theta}_R = 8.2° + 30° = 38.2°$ with respect to each other, (B) Atomic structure of the (5;0) | (3;3) class II grain boundary [68].

References

[1] R. Verre, R.G.S. Sofin, V. Usov, K. Fleischer, D. Fox, G. Behan, H. Zhang, I.V. Shvets, Surf. Sci., 606 (2012) 1815-1820.

[2] J. S. Moodera, J. Nassar, and G. Mathon, Annu. Rev. Mater. Sci., 29:381 (1999).

[3] C. A. Kleint, H. C. Semmelhack, M. Lorentz, and M. K. Krause, I. Magn. Magn. Mater., 140:725, (1995).

[4] F. C. Voogt, T. T. M. Palstra, L. Nielsen, O. C. Rogojanu, M. A. James, and T. Hibma, Phys. Rev. B, 57:R8107, (1998).

[5] D. T. Margulies, F. T. Parker, M. L. Rudee, F. E. Spada, J. N. Chapman, P. R. Aitchison, and A. E. Berkovitz, Phys. Rev. Lett., 79, 5162 (1997).

[6] J. M. D. Coey, A. E. Berkowitz, Ll. Balcells, F. F. putris, and F. T. Parker, Appl. Phys. Lett., 72:734, (1998).

[7] W. Eerenstein, T. T. M. Palstra, S. S. Saxena, and T. Hibma, Phys. Rev. Lett., 88:247204, (2002).

[8] S.K. Arora, R.G.S. Sofin, I.V. Shvets, Phys. Rev. B, 72 (2005) 134404.

[9] V.O. Golub, V.V. Dzyublyuk, A.I. Tovstolytkin, S.K. Arora, R. Ramos, R.G.S. Sofin, I.V. Shvets, J. Appl. Phys., 107, 09B108 (2010).

[10] R.G.S. Sofin, S.K. Arora, I.V. Shvets, J. Magn. Magn. Mater., 316 (2007) e969-e972.

[11] A.A. Fursina, R.G.S. Sofin, I.V. Shvets, D. Natelson, New J. Phys., 14 (2012) 013019.

[12] A.A. Fursina, R.G.S. Sofin, I.V. Shvets, D. Natelson, Phys. Rev. B, 82 (2010) 245112.

[13] S. Lee, A. Fursina, J.T. Mayo, C.T. Yavuz, V.L. Colvin, R.G. Sofin, I.V. Shvets, D. Natelson, Nat Mater, 7 (2008) 130-133.

[14] A. Fursina, S. Lee, R.G.S. Sofin, I.V. Shvets, D. Natelson, Appl. Phys. Lett., 92 (2008).

[15] A.A. Fursina, R.G.S. Sofin, I.V. Shvets, D. Natelson, Phys. Rev. B, 79 (2009) 245131.

[16] A. Ikeuchi, S. Hiura, T. Mizuno, E. Kaji, A. Subagyo, K. Sueoka, Jpn. J. Appl. Phys., 51 (2012) 08KB02.

[17] E.J. Verwey, P.W. Haayman, F.C. Romeijn, The Journal of Chemical Physics, 15 (1947) 181-187.

[18] J.P. Wright, J.P. Attfield, P.G. Radaelli, Phys. Rev. Lett., 87 (2001) 266401.

[19] C. A Domenicali, Phys. Rev., 78 (4):458 (1950).

[20] F. Walz, Journal of Physics: Condensed Matter, 14 (2002) R285.

[21] J. García, G. Subías, J. Phys.: Condens. Matter, 16 (2004) R145.

[22] G.K. Rozenberg, M.P. Pasternak, W.M. Xu, Y. Amiel, M. Hanfland, M. Amboage, R.D. Taylor, R. Jeanloz, Phys. Rev. Lett., 96 (2006) 045705.

[23] H. Eschrig, Crystal Research and Technology, 26 (1991) 788-788.

[24] S. Iida, K. Mizushima, M. Mizoguchi, K. Kose, K. Kato, K. Yanai, N. Goto, S. Yumoto, J. Appl. Phys. 53 (1982) 2164-2166.

[25] M. Mizoguchi, J. Phys. Soc. Jpn, 44:1501 (1978).

[26] J. García, G. Subías, M.G. Proietti, J. Blasco, H. Renevier, J.L. Hodeau, Y. Joly, Phys. Rev. B, 63 (2001) 054110.

[27] G. Subías, J. García, J. Blasco, M. Grazia Proietti, H. Renevier, M. Concepción Sánchez, Phys. Rev. Lett. 93 (2004) 156408.

[28] M.J. Rozenberg, Phys. Rev. B, 55 (1997) R4855-R4858.

[29] D. Khomskii, in: M. Ziese, M. Thornton (Eds.) Spin Electronics, Springer Berlin Heidelberg, 2001, pp. 89-116.

[30] W. Eerenstein, T.T.M. Palstra, T. Hibma, S. Celotto, Phys. Rev. B, 66 (2002) 201101.

[31] W. Eerenstein, T. T. M. Palstra, S. S. Saxena and T. Hibma, Phys. Rev. Lett., 88, 247204 (2002).

[32] D.T. Margulies, F.T. Parker, M.L. Rudee, F.E. Spada, J.N. Chapman, P.R. Aitchison, A.E. Berkowitz, Phys. Rev. Lett., 79 (1997) 5162-5165.

[33] S. Celotto, W. Eerenstein, T. Hibma, Eur. Phys. J. B, 36 (2003) 271-279.

[34] F.C. Voogt, T.T.M. Palstra, L. Niesen, O.C. Rogojanu, M.A. James, T. Hibma, Phys. Rev. B, 57 (1998) R8107-R8110.

[35] F.C. Voogt, T. Fujii, P.J.M. Smulders, L. Niesen, M.A. James, T. Hibma, Phys. Rev. B, 60 (1999) 11193-11206.

[36] T. Hibma, F.C. Voogt, L. Niesen, P.A.A.v.d. Heijden, W.J.M.d. Jonge, J.J.T.M. Donkers, P.J.v.d. Zaag, J. Appl. Phys., 85 (1999) 5291-5293.

[37] W. Eerenstein, T. T. M. Palstra, T. Hibma and S. Celotto Phys. Rev. B, 68 (2003) 014428.

[38] R.G. Sumesh Sofin, Thesis, Trinity Colloge Dublin, Ireland, (2006).

[39] S. Spiga, A. Lamperti, C. Wiemer, M. Perego, E. Cianci, G. Tallarida, H.L. Lu, M. Alia, F.G. Volpe, M. Fanciulli, Microelectron. Eng., 85 (2008) 2414-2419.

[40] C. Park, S.H. Jeon, S.C. Chae, S. Han, B.H. Park, S. Seo, D. W. Kim, Appl. Phys. Lett., 93 (2008) 042102.

[41] S. Seo, M.J. Lee, D.H. Seo, E.J. Jeoung, D.-S. Suh, Y.S. Joung, I.K. Yoo, I.R. Hwang, S.H. Kim, I.S. Byun, J.-S. Kim, J.S. Choi, B.H. Park, Appl. Phys. Lett., 85 (2004) 5655-5657.

[42] M. Lee, K. Kim, S. Song, S. Rha, J. Seok, J. Jung, G. Kim, J. Yoon, C. Hwang, Appl. Phys. A, 102 (2011) 827-834.

[43] B. Magyari-Köpe, M. Tendulkar,, S.G. Park,, H.D. Lee and Y. Nishi, Nanotechnol., 22, 254029 (2011).

[44] Q. Mao, Z. Ji, J. Xi, J.Phys. D: Appl. Phys., 43 (2010) 395104.

[45] C.N. Peng, C.W. Wang, T.C. Chan, W.Y. Chang, Y.C. Wang, H.W. Tsai, W.W. Wu, L.J. Chen, Y.L. Chueh, Nanoscale Res Lett, 7 (2012).

[46] W.S. K. Szot, G. Bihlmayer, R. Waser, Nat. Mater., 5 (2006).

[47] K. Szot, R. Dittmann, W. Speier, R. Waser, Phys. Stat. Sol. (RRL), 1 (2007) R86-R88.

[48] M.H. Lin, M.C. Wu, C.H. Lin, T.Y. Tseng, J. Appl. Phys., 107 (2010) 124117.

[49] M.C.Wu. M.H. Lin, C.Y. Huang, C.H. Lin and T.Y. Tseng, J. Phys. D: Appl. Phys., 43, 29, (2010).

[50] T. Ohta, A. Bostwick, J. L. McChesney, T. Seyller, K. Horn, and E. Rotenberg, Phys. Rev. Lett., 98, 206802., (2007).

[51] M. F. Craciun, Russo, S. Yamamoto, M. Oostinga, J. B. Morpurgo, A. F. Thrucha, S. , Nat. Nanotechnol., 4 (2009) 383-388.

[52] M. Bruna, S. Borini, Phys. Rev. B 2010, 81, 125421.

[53] S. Latil, L. Henrard, Phys. Rev. Lett. 2006, 97, No. 036803.

[54] W. Norimatsu, M. Kusunoki, Phys. Rev. B 2010, 81, 161410.

[55] H. K. Min, A. H. MacDonald, Prog. Theor. Phys. Suppl. 2008, 176, 227.

[56] M. Aoki, H. Amawashi, Solid State Commun. 2007, 142, 123.

[57] F. Guinea, A. H. Castro, N. M. R. Peres, Solid State Commun. 2007, 143, 116.

[58] M. Otani, Takagi, Y. Koshino, M. Okada, S. Appl. Phys. Lett. 2010, 96, 242504.

[59] E. McCann, Koshino, M. Phys. Rev. B 2010, 81, 241409.

[60] K.S. Novoselov, Geim, A. K. Morozov, S. V. Jiang, D. Zhang, Y. Dubonos, S. V. Grigorieva, I. V. Firsov, A. A., Science. 2004, 306, 666–669.

[61] K.S. Novoselov, A.K. Geim, S.V. Morozov, D. Jiang, M.I. Katsnelson, I.V. Grigorieva, S.V. Dubonos, A.A. Firsov, Nature, 438 (2005) 197-200.

[62] V.Y. Aristov, G. Urbanik, K. Kummer, D.V. Vyalikh, O.V. Molodtsova, A.B. Preobrajenski, A.A. Zakharov, C. Hess, T. Hänke, B. Büchner, I. Vobornik, J. Fujii, G. Panaccione, Y.A. Ossipyan, M. Knupfer, Nano Lett., 10 (2010) 992-995.

[63] A. Chaika, O. Molodtsova, A. Zakharov, D. Marchenko, J. Sánchez-Barriga, A. Varykhalov, I. Shvets, V. Aristov, Nano Res., 6 (2013) 562-570.

[64] K.V. Emtsev, Bostwick, A. Horn, K. Jobst, J. Kellogg, G. L. Ley, L. McChesney, J. Ohta, T. Reshanov, S. A. Rohr, J. et al. Nat. Mater. 2009, 8, 203–207.

[65] H. Hibino, H. Kageshima, F. Maeda, M. Nagase, Y. Kobayashi, H. Yamaguchi, Phys. Rev. B, 77 (2008) 075413.

[66] C. Riedl, C. Coletti, T. Iwasaki, A.A. Zakharov, U. Starke, Phys. Rev. Lett., 103 (2009) 246804.

[67] A.N. Chaika, O.V. Molodtsova, A.A. Zakharov, D. Marchenko, J. Sánchez-Barriga, A. Varykhalov, S.V. Babenkov, M. Portail, M. Zielinski, B.E. Murphy, S.A. Krasnikov, O. Lübben, I.V. Shvets, V.Y. Aristov, Nanotechnol., 25 (2014) 135605.

[68] O.V. Yazyev, S.G. Louie, Nat Mater, 9 (2010) 806-809.

[69] A. P. Sutton, R. W. Balluffi, Clarendon Press, (1995).

[70] P.Y. Huang, C.S. Ruiz-Vargas, A.M. van der Zande, W.S. Whitney, M.P. Levendorf, J.W. Kevek, S. Garg, J.S. Alden, C.J. Hustedt, Y. Zhu, J. Park, P.L. McEuen, D.A. Muller, Nature, 469 (2011) 389-392.

[71] K. Kim, Z. Lee, W. Regan, C. Kisielowski, M.F. Crommie, A. Zettl, ACS nano, 5 (2011) 2142-2146.

[72] A.W. Tsen, L. Brown, M.P. Levendorf, F. Ghahari, P.Y. Huang, R.W. Havener, C.S. Ruiz-Vargas, D.A. Muller, P. Kim, J. Park, Science, 336 (2012) 1143-1146.

Chapter 3

Experimental techniques

3.1 Introduction

In this chapter we will describe most of the experimental tools which have been used for the preparation of substrates, thin film growth, characterization and the micro-fabrication techniques. The chapter is divided into three parts. In the first part, the high temperature furnace which was used for annealing different vicinal substrates and the molecular beam epitaxy (MBE) system will be described. In the second part, the characterization techniques used to analyse the surface and bulk structure of annealed vicinal substrates and thin films will be explained. In the third part, micro and nanofabrication methods will be described. Finally, electrical and transport measurement tools will also be described.

3.2 High temperature furnace

Samples were annealed at high temperature in order to create different periodicity of the vicinal substrates. The annealing procedure was carried out using a high temperature furnace (GSL-1600X, Corporation MTI, USA). The furnace consists of four cylindrical SiC heating elements which generate the heat. A desirable temperature is controlled by the PID automatic controller and it is programmable up to 51 steps. A high purity alumina tube, surrounded by four heating elements, is placed inside the furnace for loading the samples. During the annealing it is important to close the alumina tube from both sides with two ceramic tube blocks in order to block heat radiation from the inside of the tube and prevent contamination. A S-type thermocouple is attached close to the alumina tube to measure the furnace temperature and a B-type thermocouple is used for the calibration of the furnace. The temperature ranges are varied between 1100°C and 1600°C and the constant temperature area is along a length of 6 cm in the middle of the alumina tube.

3.3 Molecular beam epitaxy (MBE)

The films for this study have been grown by molecular beam epitaxy (MBE). Using this deposition technique, thin films can be grown with very precise control over the film thickness and stoichiometry, thus increasing the reproducibility of quality thin films [1]. Moreover, the MBE system can be grown with a slow rate, low deposition temperatures and highly precise doping. The term epitaxy describes the continuation of crystal structure from the substrate to the film. The film to be grown has to be single crystal and it can be grown one monolayer at a time. Thin film lattice structure and orientation is identical to the substrate on which it is deposited. Typically material is evaporated from pellets by heating or with an electron beam. The flux of material can be controlled by the evaporation rate and once it reaches the desired thickness it can be switched off immediately using the mechanical shutters. During growth atoms can move freely on the surface until they find a proper position in the crystal lattice to bond. The surface will have many nucleation sites and so growth can proceed by the spreading of islands. The substrate temperature is also important because it affects the mobility and sticking of atoms on the surface. Expitaxially grown thin films by this technique are used in a large area of studies and applications [2-7].

A molecular beam of a metal species is created by evaporation of the surface material using a beam of high energy electrons. The molecular beam subsequently condenses on a substrate and the thin film grows expitaxially. The flux of molecular beam and energy of the evaporating e-beam can be controlled thus controlling the growth rate of the thin film. In the MBE system, an appropriate gas can be simply added into the deposition chamber. The gas may be added in molecular form or in atomic form using a plasma generator.

All of the thin films in this study have been deposited using a DCA MBE M600 molecular beam epitaxy system. The system consists of two separate chambers connected through a gate valve. The deposition chamber and load-lock chamber were designed separately. Substrates can be transferred from the load-lock chamber into the deposition chamber using a magnetically coupled transfer arms with an attached transfer cup. The pressure of the load-lock chamber can reach 5×10^{-7} Torr while the base pressure of the deposition chamber is maintained around 2×10^{-9} Torr. The picture of the MBE system is shown in Figure 3.1.

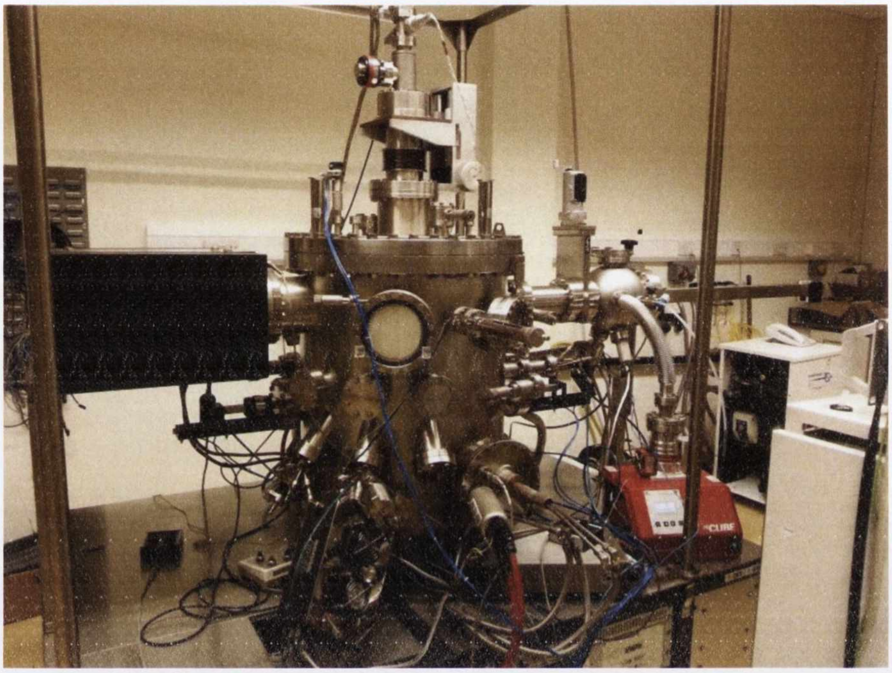

Figure 3.1 Molecular beam epitaxy system DCA MBE M600.

3.3.1 Deposition chamber

Figure 3.2 of the deposition chamber is shown below. The top of the system is fitted with a substrate manipulator which consists of a Z-stage controller. The substrate manipulator is located vertically in the centre of the chamber where the substrate is faced downwards during all processes and manipulations. The substrate manipulator is designed for the heater's electrical contacts as well. The substrate holder is surrounded by a radiation shield and a C-type thermocouple is placed between the filament and the substrate where the temperature is controlled by a EUROTHERM 2408 controller. Before depositing the thin film, the substrates have been thermally cleaned in vacuum and oxygen in order to remove all contaminations which may come from the transfer procedure.

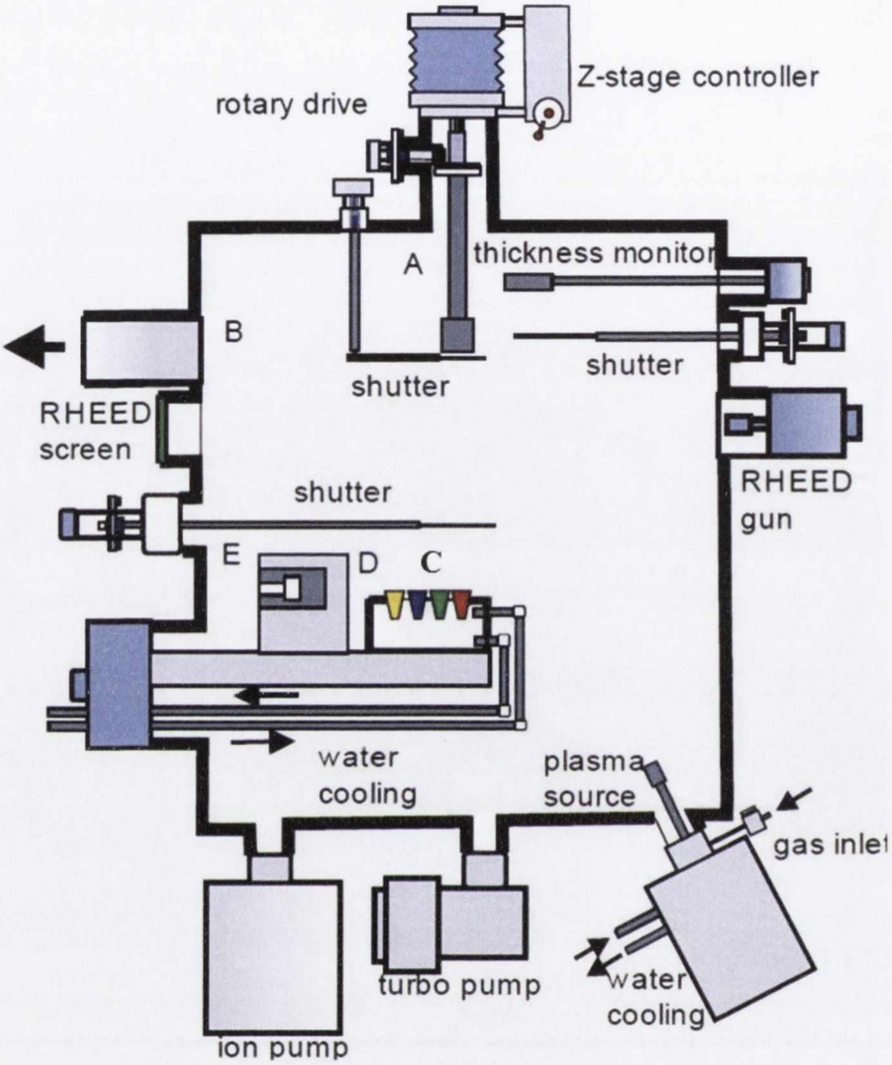

(A) Sample manipulator
(B) Load-lock chamber
(C) Crucible
(D) Water jacket
(E) e-beam evaporator

Figure 3.2 Schematic drawing of the molecular beam epitaxy system used in this study. Reproduced from [8].

The chamber is equipped with two e-guns. Four separate small crucibles are located in the first e-gun which are used for different source materials and the second e-gun used for a single large crucible. The first e-gun in the deposition chamber can be easily moved between the different crucibles with a support belt thus allowing re-filling and servicing as well.

The e-gun power and deposition rates are controlled and monitored using an INFICON IC/5 deposition rate controller. When high power is applied to the e-gun the intensity will be more thus resulting in a higher deposition rate. The deposition rate can be controlled by a sweeper module. Before and during the growth, the growth rate has been monitored using a quartz crystal monitor. The crystal monitor head is positioned face down and shielded by a shutter. This shutter is used to check the growth rate and closed once deposition starts. Each e-gun had its own shutter as well and it is used to cover e-beam until it reaches the desired growth rate. The main shutter is below the substrate manipulator. This shutter is used to interrupt all beams at any time and was only opened during loading of the sample and during the deposition. Typically it is kept closed to prevent unwanted deposition and contamination.

3.3.2 Load-lock chamber

The load-lock chamber is used to load and transfer the sample into the deposition chamber transfer arm, without disturbing the ultra-high vacuum conditions maintained in the deposition chamber. The load-lock chamber is connected to a turbo pump. The load-lock chamber is vented manually through a nitrogen valve. Once the sample is loaded into the load-lock chamber, it is pumped until the pressure reaches 2×10^{-7} Torr and then it is transferred into the deposition chamber by opening the gate valve.

3.4 Characterisation of surface morphology

3.4.1 High resolution x-ray diffraction (HRXRD)

The high resolution x-ray diffraction (HRXRD) is a powerful tool for non-destructive ex-situ investigation of epitaxial layers of heterostructures and superlattice systems. A wide range of information can be obtained from the diffraction patterns such as uniformity of epitaxial layers, thicknesses of films as well as the strain and relaxation. A detailed description of this instrument and technique are provided below.

Crystals at certain specific wavelength and incident angle produce intense peaks of diffracted radiation known as Bragg peaks (see Figure 3.3). A crystal has various planes separated by a constant parameter *d*. If reflection of the various planes interferes constructively then diffracted waves are in phase and reinforce which show maximum peaks. When diffracted waves are out of phase and cancel out then Bragg's Law is not satisfied.

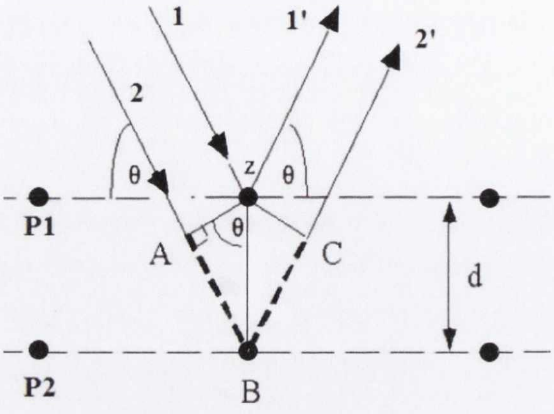

Figure 3.3 Schematic view of Bragg's diffraction.

Let us consider an x-ray beam incident on a pair of parallel planes *P1* and *P2*, separated by an interplanar spacing *d*. The two parallel incident rays *1* and *2* make an angle (*θ*) with these planes. A reflected beam of maximum intensity will result if the waves represented by *1'* and *2'* are in phase. The difference in path length between *1* to *1'* and *2* to *2'* must then be an integral number of wavelengths, (*λ*). We can express this relationship mathematically using Bragg's law:

$$2d\sin\theta = n\,\lambda \qquad (3.1)$$

Constructive interference occurs only when $n\lambda = AB+BC$, AB equal to BC which means $n\lambda$ is equal to 2AB. The extra travelled wavelength is $AB+BC$ $\sin\theta = AB/d$, from this formula we get $n\lambda = 2d\sin\theta$.

3.4.2 Instrumentation details of HRXRD

In this work we used a Bruker D8 advance diffractometer. A photograph of the system is given in Figure 3.4. The whole system is placed inside a safety case with access to the equipment through the opening window. The system itself consists of three main components: x-ray source, sample holder and detector. X-rays are produced when electrons collide with a metal target. The x-rays are produced from a Cu Kα1 transition and had a wavelength of 1.54 Å. The intensity of the x-ray beam can be controlled through the thin removable metal slits. In the case of a small sample which is less than 10 mm, the beam can be cut into a narrow range to avoid the signal coming from the sample holder. The x-ray source is attached to the moveable disc and it can be rotated with an angle of ω.

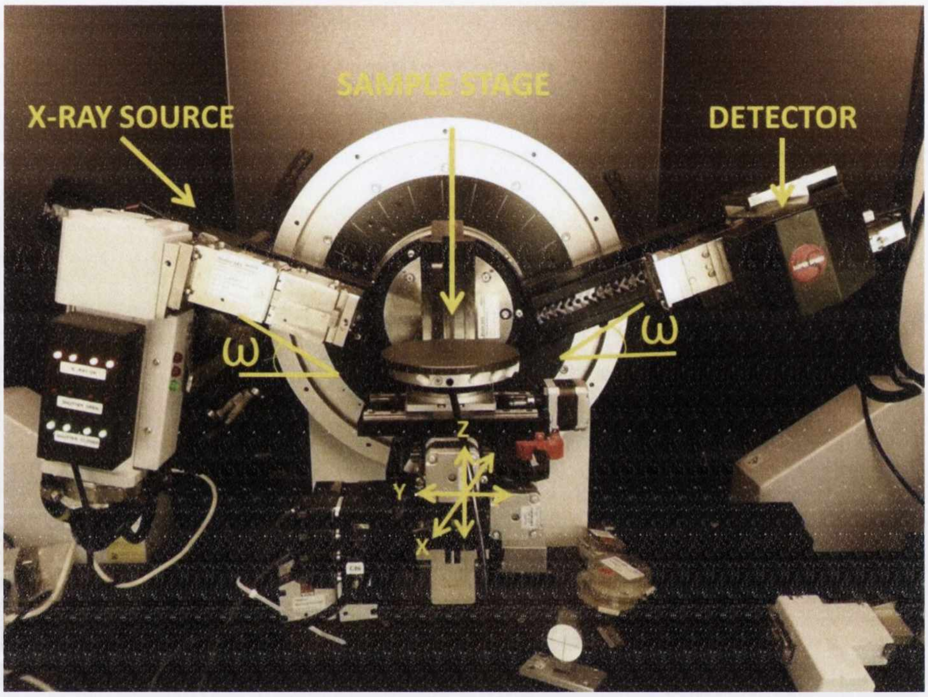

Figure 3.4 Picture of the components of the high resolution x-ray diffractometer.

The sample stage is the main moveable part which allows movement in three separate directions (x, y, z). A sample is attached into the sample holder via vacuum which is connected through the sample stage by a small pump. The detector stage is also attached to the moveable disc and is also capable of rotation through a range of angle 2θ. The beam intensity can be controlled using the copper or alumina slits. The system is fully controlled by software which was provided with the system. All the analysis software was also provided with the system.

3.4.3 X-ray reflectivity measurement (XRR)

In this study we used X-ray reflectivity (XRR) for the estimation of thickness, density and roughness of the measured thin films (single or multilayers). The x-ray reflectivity essentially consist of measuring the reflected intensity of x-rays from a sample surface at near glancing incidence [9]. The basic idea of this method is to point the x-ray beam to the film at low angles ($0 < \theta < 9°$) and measure the intensity of the reflected beam from the film surface. These reflected beams interfere with each other either destructively or constructively giving graph in oscillation in the reflectivity intensity versus incident angle (the example shown in the Figure 3.5). The oscillating intensity is related to the film thickness where their relation is given by modified Bragg's law which is written bellow:

$$m\lambda = 2t\sqrt{sin^2\theta - 2\delta}$$

where $m=1,2,3...$ is peak order, λ is the wavelength of x-ray, t is film thickness, θ is the incident angle of the beam where in our case used between $0.4° < 2\theta < 6°$ and finally δ is the dispersive refractive index of the sample used.

The interference between the rays reflected from the top and the bottom of the film results in interference fringes as shown in Figure 3.5 for the 70 nm of Fe_3O_4 film where it gives the density of material, period of oscillation and interface roughness.

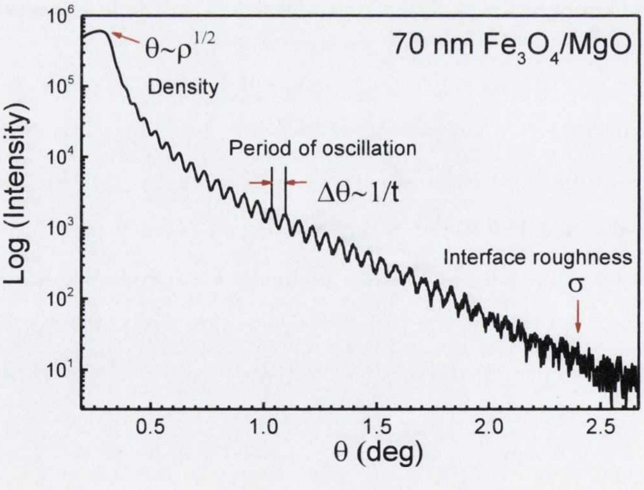

Figure 3.5 XRR scan 70 nm of epitaxial Fe_3O_4 thin film grown on single crystal MgO substrate.

3.4.4 Tilt analysis of miscut angle measurement

The miscut angle of the sample can be measured by XRD. For vicinal substrates with miscut angle α ω can range between $\theta_s \pm \alpha$. The two extreme cases are as follows: $\omega = \theta_s + \alpha$ is the case when the miscut minimum angle is facing the incident step up direction shown in Figure 3.6 (A) and $\omega = \theta_s - \alpha$ is the case when miscut maximum is facing the incident beam Figure 3.6 (B).

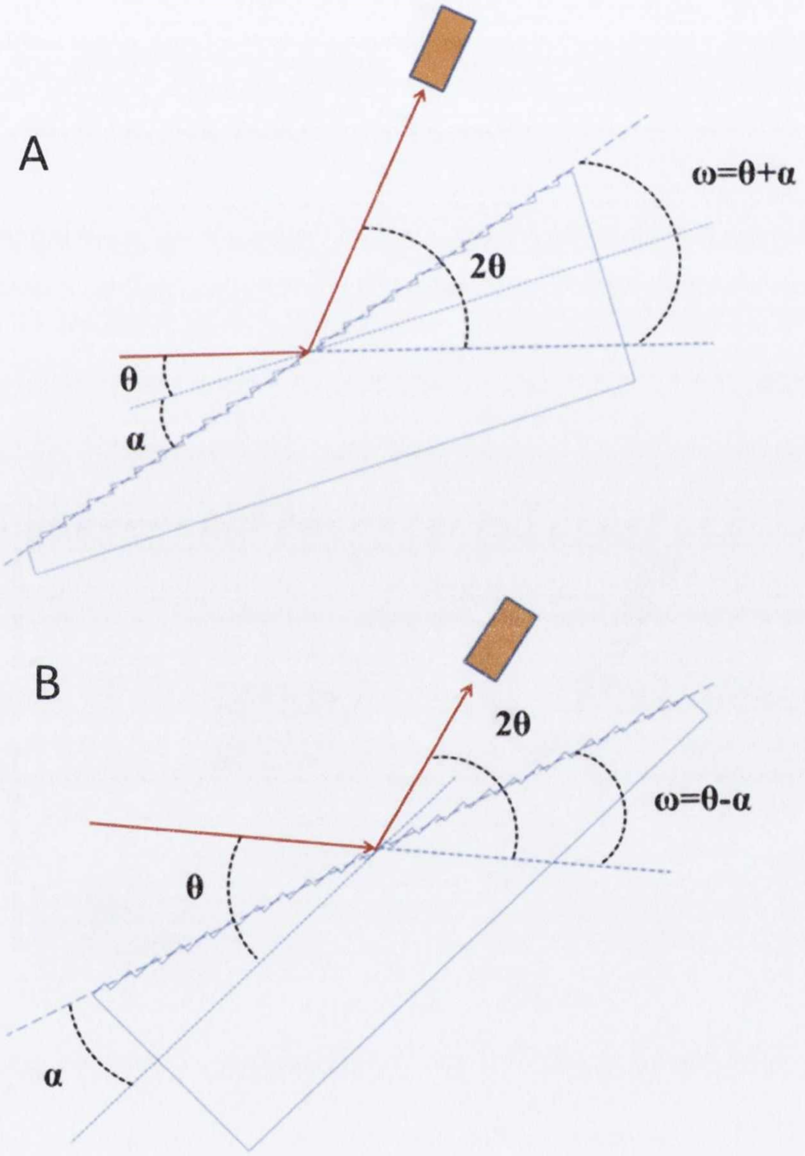

Figure 3.6 Schematic of the diffraction geometry for a vicinal surface (A) miscut minimum facing the incident beam (B) miscut maximum facing the incident beam.

3.5 Atomic force microscope (AFM)

An Atomic Force Microscope (AFM) is a device used to analyse the surface morphology. The atomic force microscope has a sharp tip at the end of a cantilever which scans over the surface and records data as an image. There are different scanning modes. In this report we will concentrate only on the in air AC scanning mode and further details of the instrument is described.

In AC mode a cantilever is attached to a piezoelectric manipulator. After applying the voltage, the piezo vibrates and the cantilever starts oscillating. The AFM measures the force acting between the tip and sample. When the cantilever is far from the sample, the interatomic force is not affected and it oscillates in its free equilibrium position. However, once it is closer to the surface, an attractive force acts upon the tip to bring the cantilever towards the surface. When the tip is in contact with the surface, repulsive force dominates pushing the cantilever backward. The laser spot is pointed of the back side of cantilever so that it detects the movement of cantilever. Figure 3.7 shows the basic concept of AFM.

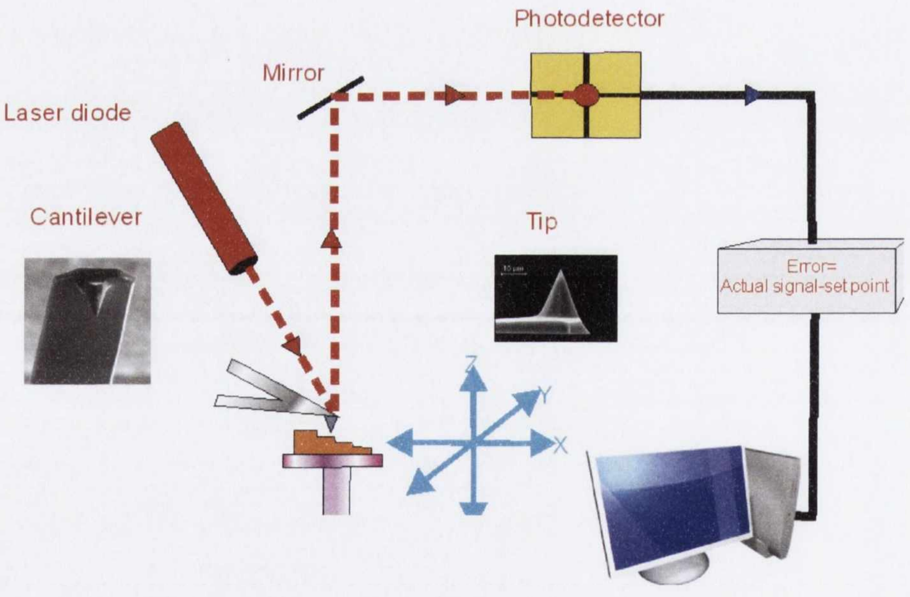

Figure 3.7 Block diagram of Atomic Force Microscope.

The cantilever is made from silicon or silicon nitride with tip radius of curvature on the order of less than 10 nm. “Tap 300-G” cantilevers are attached on the AFM. The Si cantilever has a nominal resonant frequency of 300±50 kHz. In our case we have used the Asylum Research MFP-3D AFM to characterize the surface morphology of the samples.

3.6 Scanning electron microscope (SEM)

The SEM instrument consists of two main components: an electronic console and an electronic column. The electronic console allows us to control instrument adjustments such as accelerating voltage, focus, magnification, brightness and contrast. All of the controls are accessed through the computer system using a mouse and keyboard. The electron column is where the electron beam is generated under vacuum, focused to a small diameter, and scanned across the surface of a specimen by electromagnetic deflection coils. A description of each of the components of the electron column is written below:

Electron gun: Located at the top of the column where electrons are generated by field emission from a tungsten filament at 2400°C. Electrons are primarily accelerated toward an anode, typically from 0.5 to 30kV. *Condenser lenses*: After the beam passes the anode it is influenced by two condenser lenses that cause the beam to meet and pass through a central point. What happens is that the electron beam is essentially focused down to 1000 times its original size. *Apertures*: Depending on the microscope in the electron column there may be one or more apertures. The purpose of these apertures is to reduce and exclude external electrons in the lenses. The final lens aperture situated below the scanning coils determines the spot size of the beam at the specimen. The spot size on the specimen defines the resolution and depth of field. Decreasing the spot size allows for an increase in resolution and depth of field with loss of brightness. *Scanning system*: Images are shaped by rastering the electron beam across the specimen using deflection coils inside the objective lens. Magnetic field reduces deflection of the electron beam. During the scan the electron beam should be a circular cross section when it strikes the specimen. If it is elliptical, the stigmator will act to control this problem. *Specimen chamber*: At the lower part of the column the specimen stage and controls are located. The secondary electron from the specimen is attracted to the detector by positive charge. In this study a Zeiss ULTRA Plus field emission SEM was used for imaging.

3.7 Transmission electron microscope (TEM)

The TEM tool is a powerful tool used in the area of nanoscience research. The working principal of TEM is similar to SEM but the analysed electrons are transmitted through the sample. The electrons are accelerated by high voltage (≈300 kV) to maximise electron transmission. The TEM consist of a high vacuum chamber, electron source, a column with lenses and focusing apparatus and a sample holder. Two types of imaging modes are possible: one is bright filed imagining and the other is dark field imaging. In our case we have used bright field imaging mode. In this mode the contrast of the image can be deferred from the electron which passed through the sample. The area where electrons are absorbed will be dark while the area where an electron passed freely will be bright.

The sample preparation for the TEM is very important because it requires extremely thin samples due to the small mean free path of the electrons. Before loading into the TEM, a 10 nm of Au is deposited using e-beam deposition in order to protect the surface. Afterwards, the sample is prepared in a focused ion beam system equipped with SEM (FIB-SEM). The in situ lift-out technique was used to remove a section of the sample and affix it to a TEM grid. The sample was then polished to ~ 50 nm thickness with 30 keV gallium ions. In order to reduce surface damage and amorphisation, the sample was finally polished with 5 keV gallium ions. The substrate was aligned to the [001] zone axis for TEM imaging.

3.8 Lithography processes

3.8.1 Introduction

Before doing any lithography processes, samples need to follow some treatment which is described below [10].

Sample preparation: To remove any contaminations from the surface of the sample chemical solvents were used. Afterward, the samples are heated to a higher temperature to remove any moisture that may be on top of the sample.

Spin coating: For spin coating it is important to choose a desirable process which suit the type of photoresist. Different photo-resists can be used for spin coating for a sample. Other important things in spin coating include choosing rotational speeds and required thicknesses.

Exposure: In this part the resist is exposed to UV light or an electron beam to get the desired pattern. For positive resist patterning, the exposed resist is soluble in the developer. However, for the case of negative resist, unexposed resist is soluble in the developer.

Developing: After exposing the photo-resist, the exposed area can be developed by using developer in order to remove the unwanted resist.

Lift-Off: A metal or oxide material is deposited on the entire surface of the substrate where it has direct contact with the substrate and on top of the resist which has not been removed from the substrate or thin film. When the substrate is put into acetone the resist will be washed away therefore removing the metals which has been deposited on top of the resist. After the lift-off process deposited material will stay only in the area where it had direct contact with the substrate or thin film.

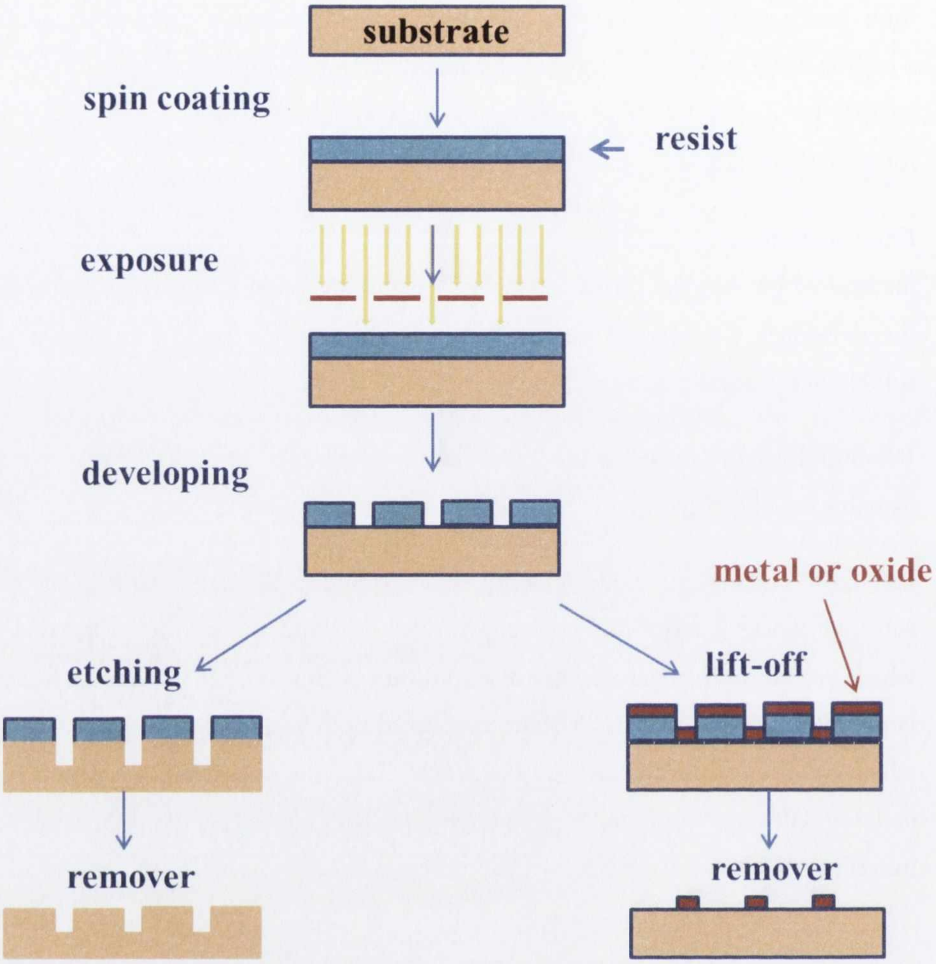

Figure 3.8 Schematic view of two types of steps followed in a lithography process.

3.8.2 UV mask aligner

To fabricate millimetre/micrometre size electrode contacts uv-lithography has been used. A Karl Suss MJB-3 UV400 has been used for exposing substrates up to 4 inch in diameter (see Figure 3.9). This type of mask aligner is most used in academia rather than in industry. The working principle of the UV mask aligner is following; the mask is held chrome side down by mask holder and it is placed right bellow optical microscope. The resist coated sample is placed on a moveable sample holder and it can be moved in three micro-positional directions (x, y and rotation angle θ). The optical microscope can also move by x and y direction to choose desirable pattern. When sample is aligned properly to the mask, it can be lifted up to make contact to the mask. Once everything is ready for the expose UV light, the UV light moves forward to start exposure. The intensity of UV light is fixed and only time of exposure can be controlled. The minimum gap that can be achieved is up to 1 μm.

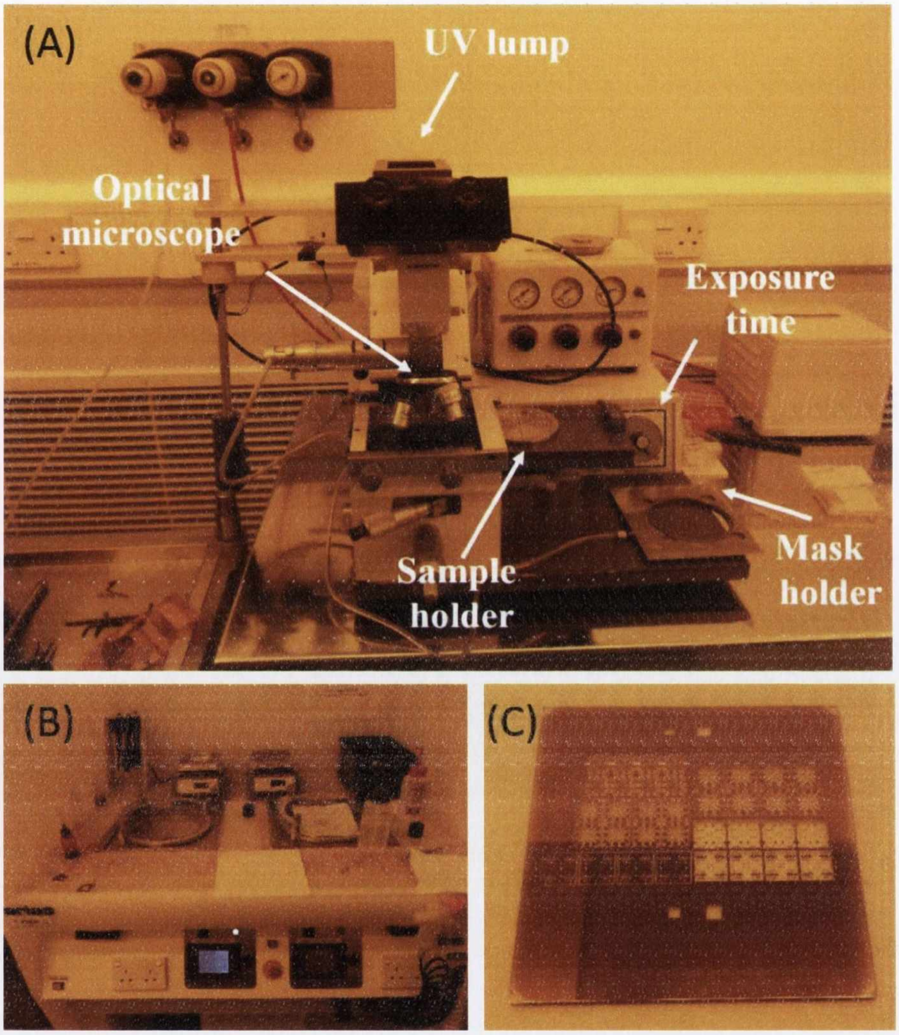

Figure 3.9 Images of the UV mask aligner, spinner, hot plate for soft baking and UV photomask

3.8.3 Electron beam lithography (EBL)

Electron beam lithography is a powerful technique which can be used to write patterns of very high resolution. A scanning electron microscope (SEM) (SUPRA40, Carl Zeiss) is equipped with a Raith50 electron lithography tool. The SEM has an imaging resolution of 1.3 nm at 15 kV, with magnification factor ranging from 12 to 9×10^5. The acceleration voltage can be set from 5 to 25 kV with a probe current ranging from 10 pA to 1nA. Dose factor can be varied accordingly between 30-300 μC/cm depending on the material. The feature size of the exposed beam can be less than 10 nm. The working principle of the EBL is the electron draws a given pattern into polymethyl methacrylate (PMMA) resist breaking the polymer chains. The exposed patterns are then removed by rinsing the sample in a solvent Methyl Isobutyl Ketone mixed with Isopropyl alcohol (MIBK: IPA). After deposition of metal, the resist can be removed by acetone (lift-off).

3.9 Electric and magnetic measurements

3.9.1 Closed cycle refrigeration (CCR) system

The closed cycle refrigerator has the following major components (see Figure 3.11): expander, compressor, vacuum shroud, and radiation shield. The expander is the main body referred to as the cold-head, where the refrigeration cycle takes pace. A compressor with two gas lines and an electrical power cable are connected to the expander. One of the gas pipe lines supplies high pressure helium gas to the expander, the other gas pipe line returns low pressure helium gas from the expander. The role of compressor is to provide the necessary helium gas flow rate at the high and low pressure for the expander. The vacuum shell encloses the cold end of the expander in vacuum, limiting the heat load on the expander caused by conduction and convection. The radiation heat shield cools the expander by helium and the vacuum shroud insulates from the room temperature.

The electric measurement of the samples was measured with a Keithley 2400 multimeter, in a standard four probe measurement. Electrical wires are connected to the sample with quick drying silver paint (Agar scientific, Batch number OW2078440). The silver paint was diluted with Iso-Butyl-Methyl-Ketone (Agar scientific, Batch number R 1272). A closed cycle refrigeration (CCR) system (Sumitmo Cryogenics HC-4E Compressor) was used to measure at low temperature. A diagram of the CCR system is shown in Figure 3.10. The samples were mounted on a copper sample holder using GE varnish which is a good thermal conductor but also an electric insulator. The samples are attached to the cold finger by a ceramic attachment directly screwed into cold finger. Helium is used as a cooler for the CCR system and the temperature is controlled by a Lake Shore 331 Temperature controller, where heating wires are near to the sample to control the cooling effect of the compressed helium from the compressor. A GaAlAs thermometer with an accuracy of ± 0.05 K is used to control the temperature of the sample holder. A compressor is used to provide the high pressure helium gas needed for the cycle. Flexible metal gas lines deliver the compressed helium gas to the refrigerator, and return the low pressure gas to the compressor for recirculation. The refrigerator includes two cold stages, one for cooling the sample and one for cooling a radiation shield that surrounds the sample.

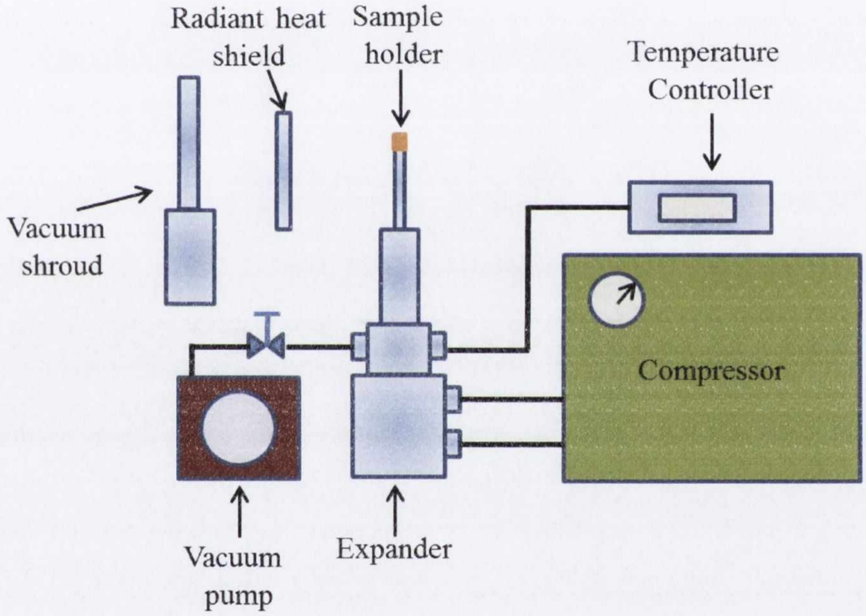

Figure 3.11 Schematic of the closed cycle refrigerator.

3.9.2 Physical property measurement system (PPMS)

The electric and transport measurement were characterized using a physical property measurement system (PPMS Quantum Design). The PPMS consists of a liquid helium cooled cryostat which is pumped by a rotary pump in which the sample can be placed and the temperature can be varied between 2 K and 400 K. The PPMS is equipped with a superconducting magnet with maximum magnetic field of 14 T and the field uniformity of ± 0.1% over 5.5 cm. The platinum resistance thermometer monitors the sample temperature with an accuracy of ±1% from zero to full field. The sample rotator's angle ranges from -10 to 370, with the step size of 0.05° (see Figure 3.12 (C)). The angular rotator is fully automated and is capable of performing angular-dependant magnetic moment measurements at a wide range of fields and temperatures. It has been designed specifically for anisotropic samples.

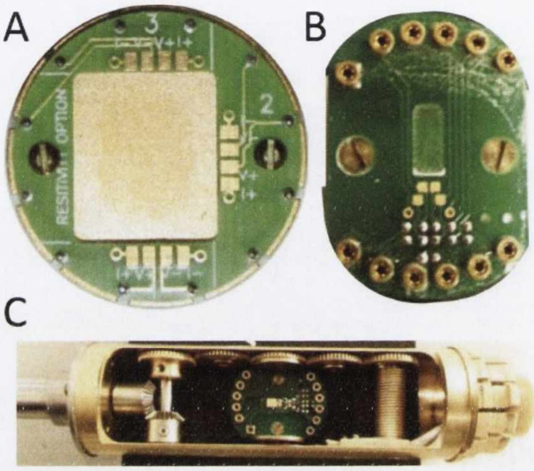

Figure 3.12 (A and B) the sample holders and (C) rotator for the electric and magnetic measurement of the PPMS system.

The resistivity puck has three groups of four marked contact pads relating to channels one, two and three on the user bridge board. Every group of contacts has one positive contact and one negative contact for both current and voltage channels to which a sample may be conventionally wired (see Figure 3.12 (A)). Therefore, up to three samples can be placed on a conventional resistivity puck or it can measure up to three contacts at one time in one sample.

3.9.3 Vibrating sample magnetometer (VSM)

In a VSM generally an electromagnet is employed to provide the DC magnetising field *H* (super conducting magnets have been used for generating higher fields) [11]. A sample is situated in between the sensing coils and it is mechanically vibrated. A changing flux coming from the vibrating magnetised sample induces a signal voltage in the sensing coils. The resulted measurement displays the magnetic moment *M* as a function of the field *H*. In this work a MicroMag$^{\text{TM}}$

Model 3900 VSM system produced by Princeton Measurements Corporation USA was used for the magnetisation measurements. VSM has high sensitivity (1 μemu at 1 sec per point) and with accuracy x, y, and z transfer stages allow quick and accurate sample placement. Sample size that can be used on the VSM is between 6 to 10 mm square and can be measured from room temperature to low temperature.

References

[1] R.F.C. Farrow, editor. Molecular Beam Epitaxy. Application to key materials. Noyer Publications, (1995).

[2] M. P. Warusawithana, C. Cen, C. R. Sleasman, J. C. Woicik, Y. Li, L. F. Kourkoutis, J. A. Klug, H. Li, P. Ryan, L.-P. Wang, M. Bedzyk, D. A. Muller, L.Q. Chen, J. Levy and D. G. Schlom, Science, 324, 367 (2009).

[3] X. J. Wang, I. A. Buyanova, F. Zhao, D. Lagarde, A. Balocchi, X. Marie, C. W. Tu, J. C. Harmand and W. M. Chen, Nat. Mat. , 8, 198 (2009).

[4] S. Nikishin, B. Borisov, M. Pandikunta, R. Dahal, J. Y. Lin, H. X. Jiang, H. Harris and M. Holtz, Appl. Phys. Lett., 95, 054101 (2009).

[5] K.-M. Ko, J.-H. Seo, D.-E. Kim, S.-T. Lee, Y.-K. Noh, M.-D. Kim and J.-E. Oh Nanotechnol., 20, 225201 (2009).

[6] I. Stolichnov, S. W. E. Riester, H. J. Trodahl, N. Setter, A. W. Rushforth, K. W. Edmonds, R. P. Campion, C. T. Foxon, B. L. Gallagher and T. Jungwirth, Nat. Mat., 7, 464 (2008).

[7] S. I. Tsintzos, N. T. Pelekanos, G. Konstantinidis, Z. Hatzopoulos and P. G. Savvidis, Nature, 453, 372 (2008).

[8] R. Ramos, Thesis, Trinity College Dublin, Ireland (2009).

[9] O. Auciello, A. R. Krauss, In situ real-time characterization of thin films, John Wiley and Sons, Inc, (2001).

[10] R. C. Jaeger, Introduction to Microelectronic Fabrication, volume V of Modular series on Solid State Devices. Prentice Hall, New Jersey, (2002).

[11] R.G. Sumesh Sofin, Thesis, Trinity Colloge Dublin, Ireland, (2006).

Chapter 4

Induced morphological changes on vicinal MgO (100) subjected to high temperature annealing: step formation and surface stability.

4.1 Introduction

Magnesium oxide (MgO) is a technologically important material. Known for its high melting temperature (above 2800°C), bulk MgO crystallizes in a rocksalt structure (fcc-structure, a = 4.212 Å) and is a large band gap (7.8 eV) insulating oxide. It is an archetypal highly ionic oxide, due to the large difference in the electronegativity of magnesium as compared to oxygen. Due to the basic character of its surface, it has found applications in heterogeneous catalysis [1, 2]. It is also very often used as substrate for the growth of epitaxial metal films [3-5], metal oxides [6, 7], high temperature oxide superconductors (HTS) [8, 9], ferroelectric pervoskites [10], resistive switching materials [11, 12] and magnetic tunnel junctions (MTJs) [13, 14].

Additionally stepped surfaces are often used as substrates, in particular as templates for producing ordered nanoparticle arrangements [15, 16], nanostructures [17], and nanowires [18]. The presence of steps arrays can influence the magnetic, electronic and transport properties of films grown on top [19-21]. Magnetic properties of epitaxial thin films grown on vicinal MgO surfaces attract a lot of attention both from the fundamental and applied points of view [21-23]. For example, the magnetic anisotropy of a Fe_3O_4 film is affected by the presence of regular *atomic* step-edge arrays. However, *atomic* step-edge arrays are inherently limited as growth templates, as the step height cannot exceed just a few angstroms. This limits the size of the structures that can be grown. Vicinal surfaces annealed at high temperature, instead, can form much larger terraces, in the sub-100nm range [24]. Therefore, the controlled preparation of these kinds of templates is valuable as they can be used as templates for the growth of larger structures.

Previous studies have dealt with the surface evolution of MgO (100) single crystals upon thermal treatment, showing the formation of steps and terraces [25-31]. However these studies were limited either to non-vicinal samples [25-27] or to a temperature regime up to 1000°C for miscut samples [28]. Other studies were carried out for (110) and (111) surfaces [29-31]. However, there are no systematic studies on vicinal MgO (100) surfaces subjected to annealing in high temperatures regimes (above 1000°C).

A crucial factor for the growth of epitaxial films is the control of defects on the substrate surface, in particular crystallographic defects, chemical contaminants and substrate smoothness. This is of particular importance in the case of MgO, due to its instability in ambient conditions arising from its reaction with moisture and CO_2. These can lead to the formation of carbonates and magnesium hydroxides on the surface, thus introducing chemical contaminants and adversely affecting the surface morphology [32]. This problem is typically overcome by thermal treatment of the MgO substrate at high temperature prior to deposition of thin films [8, 9, 33, 34]. Whereas the chemical stability of MgO surfaces exposed to ambient moisture was investigated for flat single crystals [35], no similar study has been performed on stepped MgO surfaces, leaving the question unanswered as to whether the formation of the hydroxyl-carbonates could lead to the complete destruction of ordered stepped surfaces or whether this layer of contaminants merely covers the stepped structure.

Here we make notable advances in understanding the surface properties of MgO (100) though detailed characterization of its morphology. The morphological evolution of the MgO (100) surface in the high temperature regime and the stability of the formed structures over time are investigated. In particular, it is found that steps' height and width can be fully and finely tuned by the appropriate combination of miscut angle and annealing temperature. In this way a stepped surface with desired morphological characteristics and with a low defect density can be produced. We also show that the apparent degradation of the morphology upon exposure to the ambient atmosphere, even for a prolonged time, can be reversed by short thermal treatment, thus recovering the original morphological features.

4.2 Experimental

Single crystalline one-side polished MgO (100) substrates miscut along the <010> axis with miscut angles of 2°, 3° and 4° (±0.3°) were used. Samples were received in sealed packs and, prior to annealing, were cut into 5×2.5 mm pieces and cleaned in methanol, acetone and high purity propan-2-ol. Thermal treatments were performed in a dedicated high-temperature tube furnace. The annealing temperatures ranged between 1100 – 1580°C, which was sustained for 3 hours in air. A heating and cooling rate of 5°C/min was used for both ramping up and down, to reach the desired temperatures. The miscut angles of the substrates and the minimal impact on quality due to defects like mosaicity were determined and verified by x-ray diffraction (XRD) using a Bruker D8 advanced diffractometer. The miscut of each sample was found to be within the tolerance of ±0.3° with respect to the nominal value.

After annealing, the surface morphologies were measured with an Asylum Research MFP-3D Atomic Force Microscope (AFM) in tapping mode. Al backside coated Si tips were used with nominal resonance frequency of 300 ± 50 kHz and a tip radius of ≤10 nm. For each annealed sample, at least 5 different areas were scanned and the results were averaged on more than 200 terraces and steps. A FEI Titan transmission electron microscope (TEM) operating at 300 kV was used to investigate a cross section of the surface with the normal of the section close to the 001 axis of the substrate. The thin TEM lamella was prepared in a Carl Zeiss Auriga CrossBeam focused ion beam workstation (FIB). All images were acquired in bright-field mode. The full-field strains at the MgO interface were mapped by using the geometric phase analysis (GPA). By selecting a geometric phase image, a desired numerical Moiré image corresponding to a group of special crystal planes can be obtained, thus allowing a detailed analysis of this group of crystal planes [36].

In order to determine the presence of contaminants, both as-received and annealed samples were analyzed by X-ray photoelectron spectroscopy (XPS) using an Omicron Multiprobe XP system equipped with a monochromatic Al k-alpha source in conjunction with an Omicron EA 125 and hemispherical analyzer. Pass energy of 20 eV was used. Due to the insulating nature of the samples, an Omicron C-10 charge neutralizer was used. Beam energy, emission current and deflection were optimized to achieve a FWHM of the O 1s peak comparable with respect to the line-width typical of a sample not affected by charging effects (FWHM = 1.5 eV). The obtained spectra were analyzed by means of the CasaXPS software. To minimize surface contamination, samples were loaded into the XPS chamber, immediately after annealing at 1300°C for 3 hours.

4.3 Results and discussion

Here we demonstrate that vicinal MgO surfaces can be facetted by the appropriate annealing treatment in air and we illustrate the role of substrate miscut angle in step faceting. A clear step and terrace morphology is observed with well-defined steps and atomically flat terraces as shown in Figure 4.1(a). Steps are distributed with a high degree of uniformity over the entire surface, running parallel along the [001] direction. The temperature dependence of the surface morphology was studied in the range of 1100°C-1580°C and analyzed by AFM. The results are summarized in Table 1.

For a fixed temperature, the miscut angle plays an important role in the final morphology of the system. Comparing the substrates miscut by 2° and 4° from the <010> direction, annealed at a temperature of 1200°C, it can be seen that, within error, larger miscuts result in smaller step periodicity and a higher average step height. This observation can be qualitatively explained using a simple geometrical argument. Prior to annealing, the vicinal surfaces had a denser distribution of monoatomic steps, in proportion with the miscut angle. During annealing, steps gather together, and as a consequence, the higher the miscut angle, the higher the final step height is. However, in order to preserve this greater miscut angle, the step periodicity also needs to decrease.

The temperature dependence was examined for the 3° miscut samples annealed at 1100°C - 1580°C. From Table 1 it can be seen that the average periodicity width increases with higher annealing temperature.

Table 1

Average periodicity <L> and step height <h> with relative standard deviation for different miscut angles at various annealing temperatures. The miscut listed was measured with high resolution XRD.

Miscut	2°		3°			4°	
T (°C)	1200	1100	1200	1300	1400	1580	1200
<L> (nm)	98 ± 38	55 ± 18	74 ± 23	136 ± 46	212 ± 75	285 ± 95	54 ± 16
<h> (nm)	3 ± 0.9	2.7 ± 0.8*	3.1 ± 0.9	6.9 ± 3	11.3 ± 5	14.5 ± 5	3.4 ± 1

*Due to the small dimensions of the structure involved, measurements of the exact step height was not possible. In this case a step height was calculated using formula $h=tan\theta\times L$.

In order to explain this, it is worth noting that if the surface rearrangement can be considered as a thermally activated diffusion process, a direct relationship between surface periodicity and average displacement of adatoms can be assumed. In this case the square of the period L^2 is proportional to the diffusion constant D through the Einstein diffusion equation. Considering an effective diffusion constant $D=D_o\exp(-E_{ac}/k_BT)$, the activation energy of the thermal process, E_{ac}, can be calculated [37]. We implicitly assumed here a value $D_0 = 2.5\times10^{-6}-1.8\times10^{-6}$ cm^2/sec [38, 39]. The reported value for the nominally flat MgO which were varied between 2.7 and 3.24 eV [39-41], the activation energy which reported here is E_{ac}=1.61±0.2 eV. However, the large errors involved in the data makes it difficult to conclusively attribute this as a definitive explanation for the step rearrangement.

From the sample of Figure 4.2(a) it is clear that very few defects such as kinks and step merging are visible on the annealed surface, suggesting a very low free energy configuration for the considered system. A scattering of small diagonal steps of variable height from 0.73 nm up to 3.17 nm run on the flat terraces as shown in Figure 4.2(a). They are all aligned to [011] and $[1\bar{1}0]$, i.e. (45° ± 3) respect to the <001> step direction. Similar steps have already been observed in c-plane Al_2O_3 and they are related to different surface energy of such monoatomic steps originated by different atomic arrangements [42].

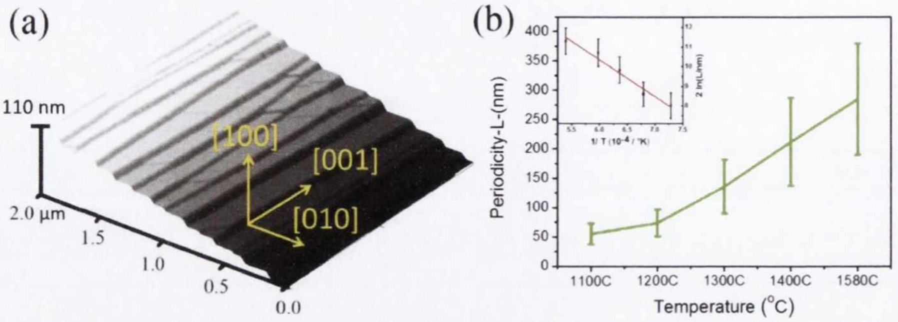

Figure 4.1 Facet formation after annealing of MgO (100) at a high temperature. (a) 2x2 μm^2 AFM image, after first order leveling, of a 3° miscut of MgO (100) substrate annealed at 1300°C for 3 hours. (b) Temperature dependence of the periodicity as a function of the annealing temperature and the Arrhenius plot of the period is shown in the inset.

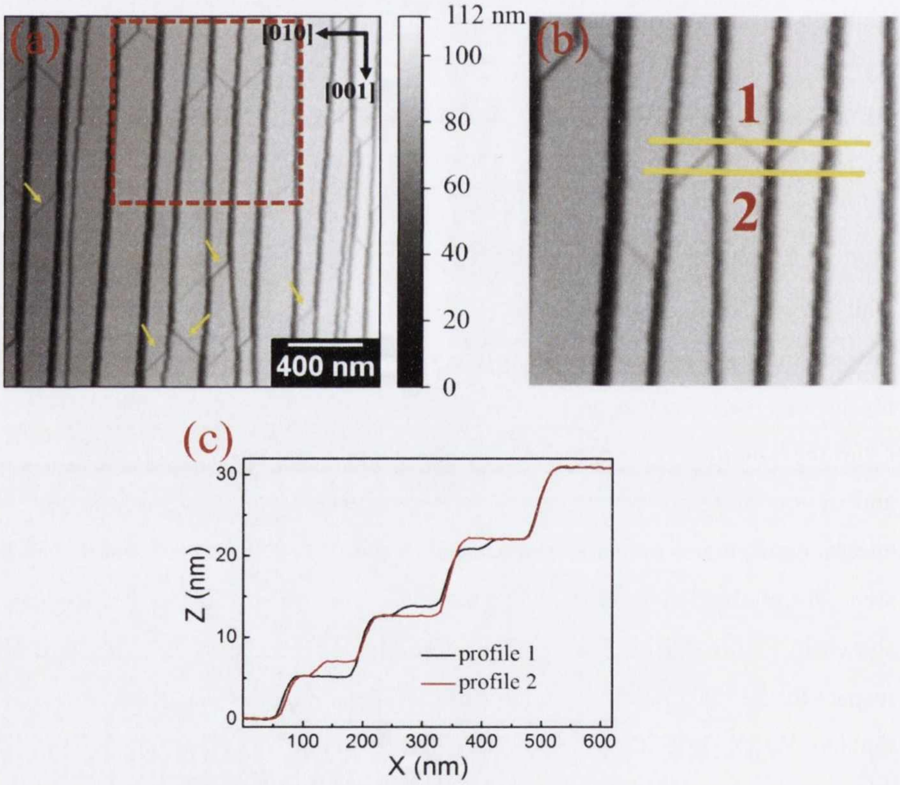

Figure 4.2 2x2 μm^2 AFM image of 3° miscut of MgO (100) annealed at 1300°C for 3 hours. (a) Defects are pointed by yellow arrows (b) A magnification of the solid red square. (c) Height profile taken from the section along lines 1 and 2 of (b).

Surfaces with comparable periodicities were analyzed, and the step height appeared smaller for the smaller off-cuts, preserving the overall surface orientation. Thus the periodicity can be varied, for a given off-cut angle, by changing the annealing temperature and the step height can be tuned by varying the initial sample off-cut. Full control of the morphology of the stepped surface, periodicity and step height, can hence be obtained.

In order to fully characterize the surface morphology, a cross section of the faceted surface was examined using TEM. The analysis was performed for a 3° miscut sample annealed at 1200°C. As shown in Figure 4.3, all the steps appear inclined at an angle of 10±2° with respect to the [010] direction and their orientation is independent on the step height.

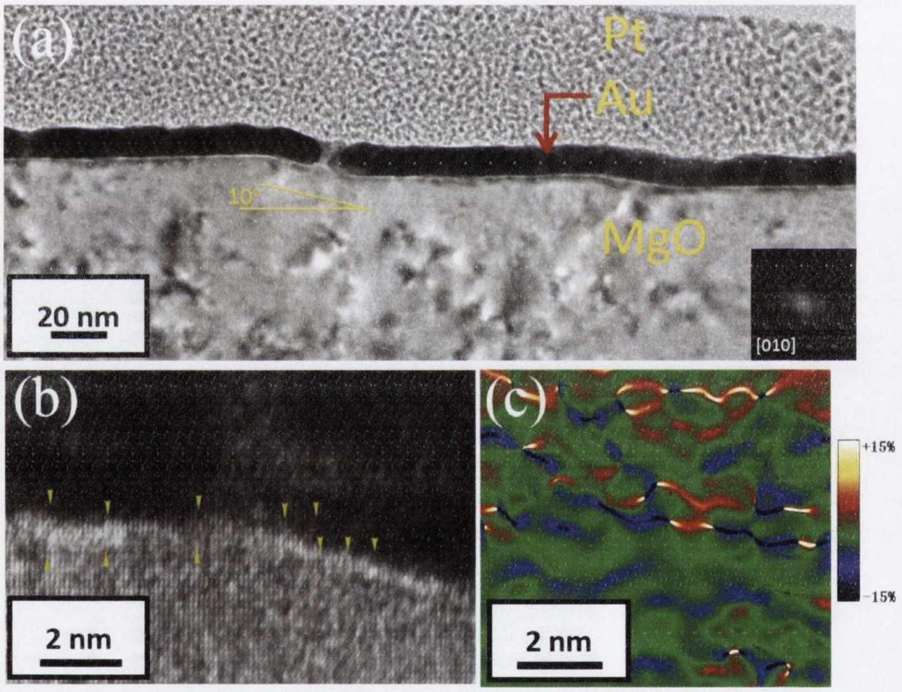

Figure 4.3 TEM section of a sample 3° miscut and annealed at 1200°C for 3 hours. An Au protective layer was deposited on the surface before preparation of the section to protect the surface. (a) Low magnification showing the cross section of MgO, the slope of step is 10±2° with respect to the [010] (insert). (b) High magnification image of interface boundary of MgO and Au showing strain field. (c) Geometric phase analysis image of 10° slope. The blue color indicates strain field in the lattice.

The lattice-resolved image (Figure 4.3(b)) shows a bright strip at the interface between the MgO substrate and the Au layer which is due to the strain field at the interface. Figure 4.3(c) shows the strain components ε_{xx} at the MgO interface to analyze the effect of the lattice mismatch on the GPA result. It can be noticed that there are several regions of strain around the misfit dislocation cores between MgO and Au. Along the interface compressive rather than positive tensile strains dominate. Although the delocalization of the TEM phase imaging inhibits the definite resolution of the surface lattice configuration, it can be seen from the GPA a stepped strain field that the 10° steps most likely exhibit a 6(100)x(010) or 5(100)x(010) surface, i.e. the Miller indices are (160) or (150) which corresponds to angles of 9.5° and 11.3° respectively.

The results observed can be explained by the kinetic evolution taking place on the surface. As the annealing temperature is increased the attractive nature of the step edges, mediated by elastic forces, allows them to bunch into facets, giving rise to wider terraces and higher steps [43-46]. Because surface kinetics are far more strongly dependent on temperature than time, the bunching occurs in a time of the order of few minutes. Samples were annealed for 24 hours, and it was verified that the periodicity of the stepped surface did not appreciably change when compared with a similar sample annealed for 3 hours.

The mechanism responsible for the rearrangement of the surface appears to be common to all samples. This is supported by Figure 4.4 where the probability *P(L)* of observing two steps separated by a distance *L* is plotted versus step separation normalized over the mean step normalized period *L/<L>*. From Figure 4.4 it is evident that the step distribution does not significantly depend on either the annealing temperature or the off-cut angle.

Elastic theory predicts the equilibrium morphology consisting of a periodic array of facets, as observed in this study [44-46]. The attractive interaction between steps, mediated by the elastic strain field created by individual steps [29-32], could then explain the faceted morphology. Nevertheless, a complete explanation of the mechanisms involved is still lacking. If one assumes only nearest neighbor step interactions, the Gaussian distribution of Figure 4.4 should be invariant whenever <L>P(L) (and not simply P(L)) is plotted vs the normalized period L/<L> [46-48]. The complicated behavior could be caused by the presence of competing effects in the surface evolution, such as entropic contributions and inter-step long range interactions or the possible influence of contaminants [49, 50].

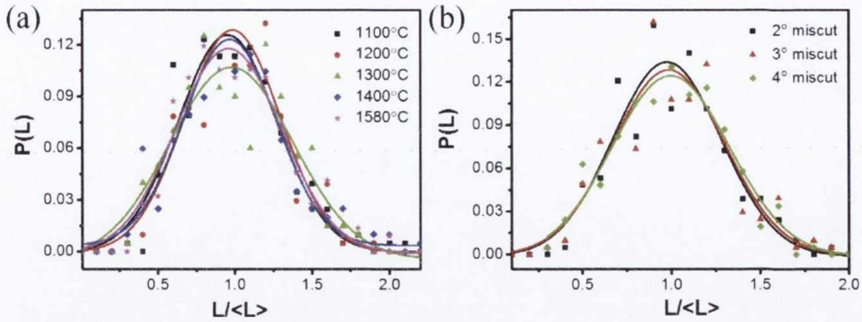

Figure 4.4 Normalized distribution of the period as a function of L/<L> for different annealing temperatures (a) with a substrate miscut angle 3° and (b) for an annealing temperature of 1200 °C

Contaminants can play a major role in the faceting process. Therefore it was necessary to determine the presence of impurities and assess their concentration [49, 50]. To this end, both the as received and the post annealed samples were subjected to investigation by x-ray photoelectron spectroscopy (XPS) (see Figure 4.5). Before the annealing process, carbon represents the main contaminant (21%). A small amount of Ca (1.5%) was found as well, together with an unknown contaminant, having a binding energy of 242.5 eV. Such a signal has been seen in previous XPS studies of MgO substrates [51] and was attributed to a small stray signal coming from the Ta sample holder. This conclusion is questionable, as the same signal was observed in the course of our experiments while using a stainless steel holder.

After annealing, the relative presence of carbon on the surface was strongly reduced (16%) while that of calcium was increased (4%). This is because of single crystal MgO substrate will have some Ca impurities on the bulk and this impurities segregates into the MgO surface after annealing them at temperature more than 950°C which was confirmed by XPS analysis [52, 53]. Aluminum contaminants, not present on the pristine surface, appear after the annealing treatment (3.5%). The fact that such contaminants are present only in the post-annealed substrates brings us to the conclusion that this is an external contamination coming from the alumina tube furnace used for the annealing process. Traces of Al on the surface suggest that contamination is one of the driving mechanisms for the formation of such stepped surfaces, as was demonstrated for other oxides, *e.g.* Al_2O_3 [54] and $SrTiO_3$ [55]. To confirm this, we cut into halves a vicinal substrates having a 3° miscut. One half of the sample was annealed at 1100°C in an alumina tube and the other half in a quartz tube. The half annealed in the quartz tube did not produce a step and terrace structure. However, the piece annealed in the alumina tube produced the typical step and terrace structure.

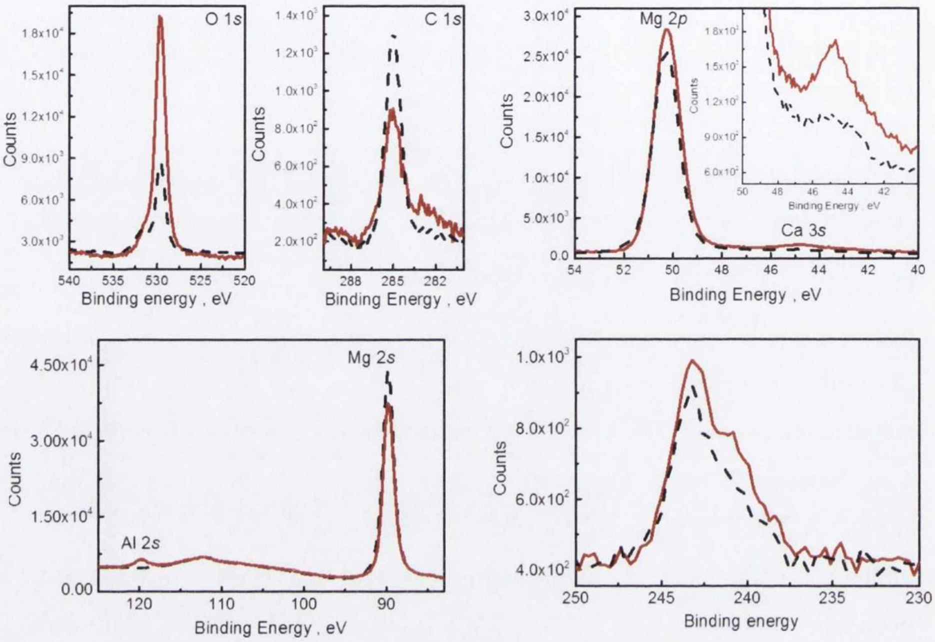

Figure 4.5 XPS investigations of the as received (dashed black line) and post annealed (solid red line) samples.

The MgO surface is quite reactive with the atmospheric moisture and carbon dioxde [25]. Once the step and terrace morphology was formed on the surface by annealing, samples were exposed to ambient conditions and re-examined using AFM over an extended time period. The evolution of the surface morphology over time is shown in Figure 4.6. Right after the high temperature treatment the surface had clear stepped morphology as shown in Figure 4.6(a). However, after few weeks of exposure, contamination starts covering the stepped surface (see Figure 4.6(b)). After 5 months, the contaminants fully cover the stepped surface leaving no sign of the steps and terraces, (Figure 4.6(c)). Figure 4.6(d) shows the profile along the line in image Figure 6(c), which was found to have a roughness of ~41 nm.

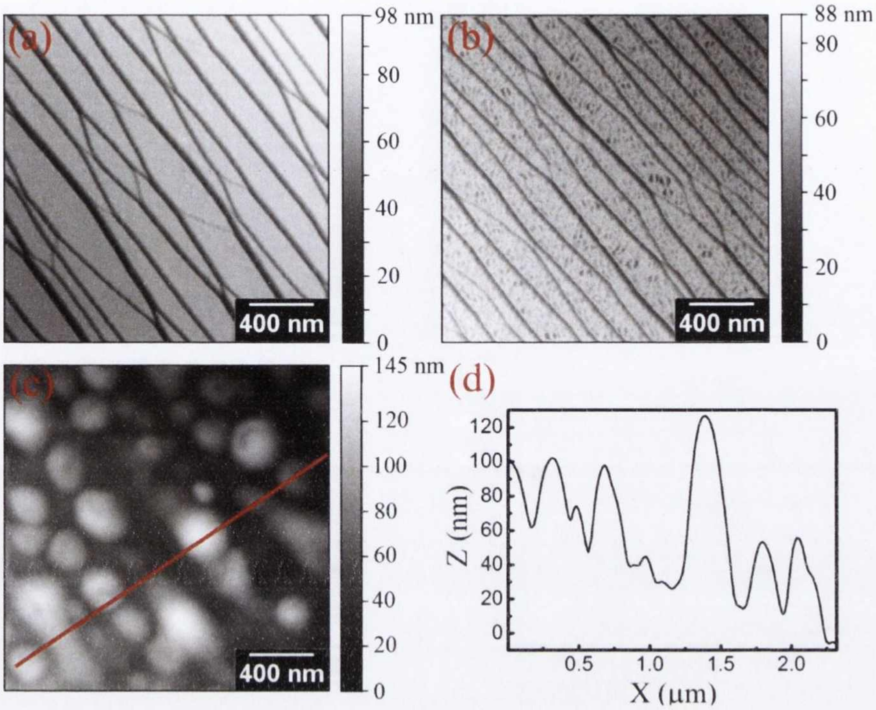

Figure 4.6 2x2 μm^2 AFM image of stepped MgO substrate after exposure to ambient conditions for: one day (a), few weeks (b), few months (c) and height profile across the red line shown in c (d)

However, this apparent destruction of surface morphology can be reversed and the original stepped morphology can be restored after a short thermal treatment at a moderate temperature (200°C for 1 hour), as shown in Figure 4.7.

A sample with steps and terraces was analysed over eight months to assess the effect of surface contamination. In Figure 7(a), the sample was scanned by AFM immediately after annealing at 1100°C, then it was kept for eight months in air. After this time the sample was completely covered with contamination, Figure 4.7(b). Similar behaviour has been reported in literature whenever MgO samples were kept for few days in air [25]. In order to verify that such contaminations do not destroy the step and terrace features, the sample was cleaned in acetone, methanol and IPA then put on a hot plate at 200°C for 1 hour. As seen in Figure 4.7(c), the step and terrace features reappear and most of contamination has been removed even at this rather low temperature [56-61].

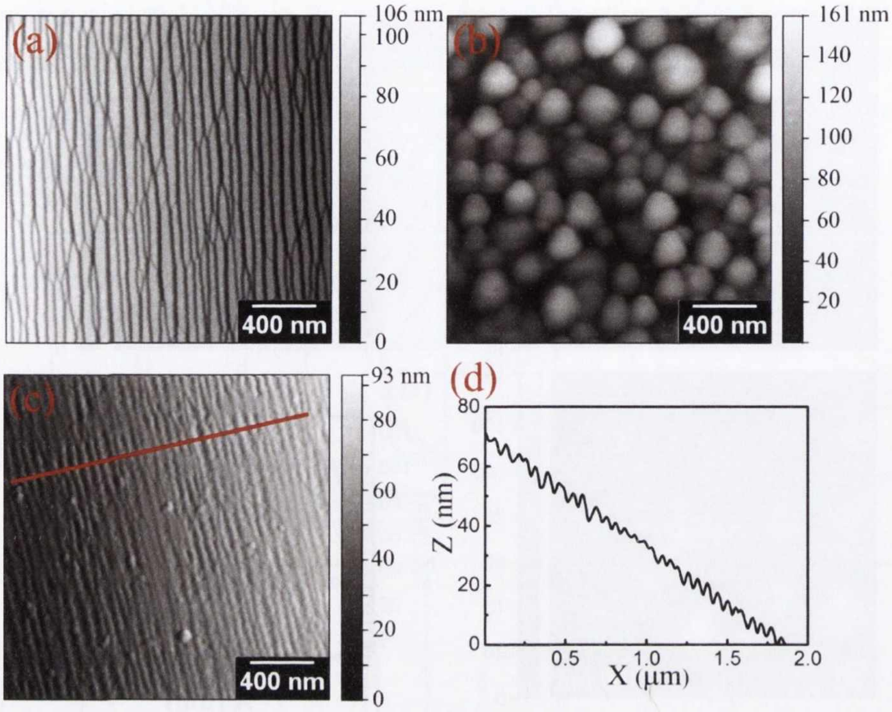

Figure 4.7 2x2 μm^2 AFM images of stepped MgO (100) surface, (a) annealed at 1100°C, (b) kept for eight months in air, (c) and after baking on a hot plate for 200°C for 1 hour and (d) height profile across the red line shown in (c). The experiment demonstrates that the surface morphology can be retrieved due to the decomposition of contaminants formed on the surface.

XPS measurements were performed on the sample, which had been kept in ambient conditions for eight months, before and after the thermal treatment at 200°C for one hour. For simplicity, the sample kept for eight months in ambient condition after the formation of vicinal surface as described earlier, will henceforth be referred to as "pre-treatment" whereas the sample after the cleaning procedure at 200°C will be defined as "post-treatment". In order to verify the reproducibility of the cleaning procedure, more than one sample was measured. Figure 4.8 shows the core levels O 1*s*, C1*s* and Mg 2*p* XPS spectra recorded for the sample before and after cleaning. It can be noted, the O 1*s* peak for pre-treatment sample is centred at 532 eV, and has a FWHM of 2.15 eV, which is much larger than expected for a peak consisting of a single component (1.5 eV) (Figure 4.8A). Indeed, the O1*s* core level can be deconvoluted into 3 components, having respective binding energies of 530.6 eV, 531.9 eV and 533 eV. Comparison with literature brings us to the conclusion that these components have to be assigned respectively to Mg bond to oxygen (such as in MgO), Mg bond to an hydroxyl group (as in $Mg(OH)_2$), and Mg bond to a carbonate group (as in $MgCO_3$) [62, 63] and that hydroxyls and carbonates together can roughly account for 90% of the oxygen present on the surface. Further confirmation of hydroxyl and carbonate formation comes from analysis of the C1*s* and Mg 2*p* core levels. Regarding the C1*s* core level, it is clearly visible that this consists of two distinct components, the first at 285 eV, characteristic of aliphatic carbon, the second at 289 eV, typical of Mg bonded to carbonate [64] (Figure 4.8(b)). Also the Mg 2*p* peak is centred at the value of the binding energy expected for Mg-OH bonds (51.7 eV) and shows a FWHM (1.6 eV) higher than expected for a single component peak (1.3eV). However, resolving the different components in this case is much more difficult than for the O1*s* core level, due to the relative close vicinity of the expected binding energies for oxide, hydroxyl and carbonate type of bonds [65, 66]. Nevertheless, based on the peak position (Figure 4.8(c)) and on the FWHM we can conclude that magnesium hydroxyl and carbonate are present on the surface and can account for, again, at least 90% of Mg present.

After the cleaning treatment, the morphology of the surface recovers, as is demonstrated in Figure 4.7(c), due to the decomposition of the hydroxyl and carbonates present on the surface. This latter observation is supported by analysis of the XPS spectra of the post-treatment sample. The relative C1*s* core level shows only one component, at 285 eV, while the components previously observed at 289 eV almost completely disappear. Moreover the Mg 2*p* core is now centred at 50.3 eV, in line with the value expected for a Mg-O bond, and has a lower FWHM (1.3 eV). Analysis of the O1*s* however suggested that small amounts of impurities might still be present: two distinct components are in fact visible, the main one is centred at 529.5 eV related to the Mg-O bond, the second at 531.5 related to the Mg-OH bond. According to the quantitative analysis, 20% of the O atoms are still present in the form of hydroxyls. According to literature, $MgCO_3$ and $Mg(OH)_2$ only starts to decomposed below 200°C [56], a temperature higher than that used for the cleaning procedure. However, other hydroxy-carbonates of magnesium such as hydromagnesite do show decomposition temperature below or comparable to those used for the cleaning procedure. Therefore, taking into consideration the information coming from the XPS and AFM analysis, as well as the temperature at which the thermal treatment was performed we can conclude that the contaminants present on the surface are not pure $Mg(OH)_2$ or $MgCO_3$ but a mixed magnesium hydroxyl-carbonate, which can decompose even at this low temperatures.

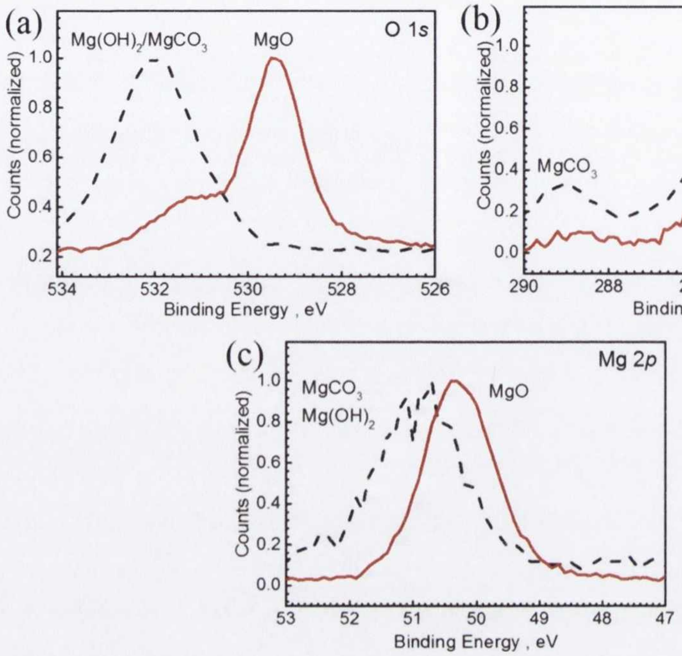

Figure 4.8 XPS spectra for a stepped sample after eight months of ambient exposure (dashed black line) and after thermal treatment on hot plate (solid red line).

In addition to this study, we first time demonstrated depositing of gold nanoparticles (NPs) and iron nanowires (NWs) which were taken by SEM images.

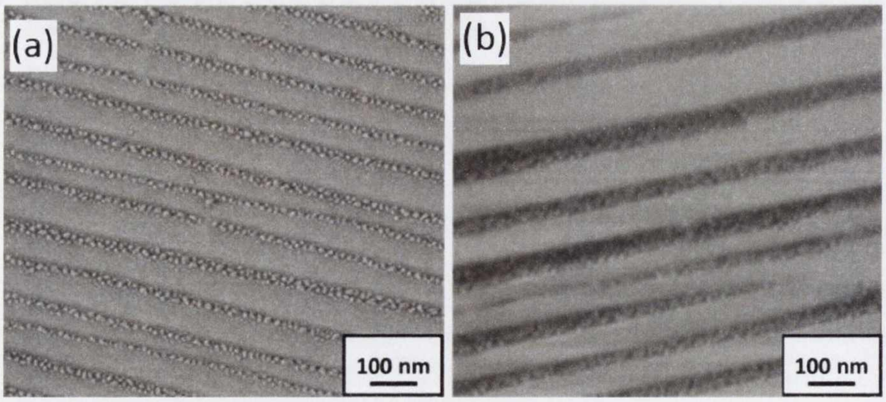

Figure 4.9 SEM images of gold nanoparticles (NPs) (a) iron nanowires (NWs) (b)

4.4 Conclusion

The effects of annealing MgO (100), miscut along the [010] direction, at the temperatures of 1100-1580°C, were investigated. Detailed AFM analysis was performed, revealing a mesoscopic faceted step-and-terrace surface. The possibility of tuning both periodicity and step height was demonstrated by modifying the annealing temperature and the miscut angle respectively. The average terrace periodicity increases with the temperature while the step height increases with miscut angle. This self-assembly phenomenon was found to be completely reproducible for all the samples investigated. Careful TEM analysis found the step inclination to be 10±2° with respect to the terraces. Possible causes for the phenomena have been discussed together with the long term stability of the surface. The presence of impurities was assessed before and after annealing. Aluminium contaminations coming from the alumina tube used for the annealing were found in post annealed sample. Comparison with samples annealed at the same temperature in a quartz tube did not facet, leading us to the conclusions their presence is the driving mechanisms responsible for the formation of step and terrace structures. The formation of a thick layer of contaminants, covering steps and terraces, was observed after long term exposure of the sample to atmosphere. A procedure was outlined to decompose such contaminants by short thermal annealing at moderate temperatures, thus recovering the original morphology.

References

[1] Jingxia Li , Wei-Lin Dai and Kangnian Fan J. Phys. Chem. C, 112 (2008) 17657-17663.

[2] Gizelle I. Almerindoa, Luiz F.D. Probsta, Carlos E.M. Camposb, Rusiene M. de Almeidac, Simoni M.P. Meneghettic, Mario R. Meneghettic, Jean-Marc Clacensd, Humberto V. Fajardoe, J. Power Sources, 196 (2011) 8057-8063.

[3] R.A. Lukaszew, V. Stoica, C. Uher, R. Clarke, Mater. Res. Soc. Symp. Proc., 648 (2001) p. P3.29.21.

[4] M. Ohtake, F. Kirino, M. Futamoto, Jpn. J. Appl. Phys., 46 (2007) L895.

[5] Y. Nukaga, M. Ohtake, F. Kirino, M. Futamoto, J. Phys.: Conf. Ser., 200, (2010) 072071.

[6] J. Du, S. Gnanarajan, A. Bendavid, Supercond. Sci. Technol., 18 (2005) 1035.

[7] K. Iida, J. Hänisch, S. Trommler, V. Matias, S. Haindl, F. Kurth, I.L.d. Pozo, R. Hühne, M. Kidszun, J. Engelmann, L. Schultz, B. Holzapfel, Appl. Phys. Express, 4 (2011) 013103.

[8] B. H. Moeckly, S. E. Russek, D. K. Lathrop, R. A. Buhrman, Jian Li, and J. W. Mayer, Appl. Phys. Lett., 57, 1687 (1990).

[9] K.H. Wu, S.P. Chen, J.Y. Juang, T.M. Uen, Y.S. Gou, Physica C: Superconductivity, 289 (1997) 230-242.

[10] R. Ramesh, K. Luther, B. Wikerns, D.L. Hart, E. Wang, J.M. Tarascon, A. Inam, X.D. Wu, T. Venkantesen, Appl. Phys. Lett. 57 (1990) 1505.

[11] S. Lee, A. Fursina, J.T. Mayo, C.T. Yavuz, V.L. Colvin, R.G. Sofin, I.V. Shvets, D. Natelson, Nat Mater, 7 (2008) 130-133.

[12] A.A. Fursina, R.G.S. Sofin, I.V. Shvets, D. Natelson, Phys. Rev. B, 79 (2009) 245131.

[13] Jia Zhang, Yan Wang, X.-G. Zhang, and X. F. Han, Phys. Rev. B, 82 (2010) 134449.

[14] D.W. Guo, F.A. Cardoso, R. Ferreira, E. Paz, S. Cardoso, P.P. Freitas, J. Appl. Phys., 115 (2014) 17E513.

[15] R. Verre, K. Fleischer, O. Ualibek, I.V. Shvets, Appl. Phys. Lett., 100 (2012) 031102.

[16] R. Verre, K. Fleischer, J.F. McGilp, D. Fox, G. Behan, H. Zhang, I.V. Shvets, Nanotechnol., 23 (2012) 035606.

[17] S. Benedetti, L. Gragnaniello, M. Franchini, P. Torelli, S. Valeri, Superlattices Microstruct., 46 (2009) 153-158.

[18] A. Ueda, R.R. Mu, V.C. Saunders, T.C. Livingston, M.H. Wu, D.O. Henderson, in: Surf. Eng., John Wiley & Sons, Inc., 2002, pp. 35-42.

[19] H. Zheng, L. Salamanca-Riba, R. Ramesh, H. Li, Appl. Phys. Lett., 85 (2004) 2905-2907.

[20] R. Ramos, S.K. Arora, I.V. Shvets, J. Appl. Phys., 105 (2009) 07B108.

[21] V.O. Golub, V.V. Dzyublyuk, A.I. Tovstolytkin, S.K. Arora, R. Ramos, R.G.S. Sofin, I.V. Shvets, J. Appl. Phys., 107, 09B108 (2010).

[22] B.B. Maranville, A.L. Shapiro, F. Hellman, D.M. Schaadt, E.T. Yu, Appl. Phys. Lett., 81 (2002) 517-519.

[23] L. McGuigan, R.C. Barklie, R.G.S. Sofin, S.K. Arora, I.V. Shvets, Phys. Rev. B, 77 (2008) 174424.

[24] R. Verre, R.G.S. Sofin, V. Usov, K. Fleischer, D. Fox, G. Behan, H. Zhang, I.V. Shvets, Surf. Sci., 606 (2012) 1815-1820.

[25] D.K. Aswal, K.P. Muthe, S. Tawde, S. Chodhury, N. Bagkar, A. Singh, S.K. Gupta, J.V. Yakhmi, J. Cryst. Growth, 236 (2002) 661-666.

[26] Hideaki Zama, Yukie Ishii, Hiroshi Yamamoto and Tadataka Morishita, Jpn. J. Appl. Phys., 40 (2001) L465-L467.

[27] A.B. Joshi, M. Grant Norton, Appl. Surf. Sci., 115 (1997) 307-310.

[28] S. Benedetti, P. Torelli, P. Luches, E. Gualtieri, A. Rota, S. Valeri, Surf. Sci., 601 (2007) 2636-2640.

[29] D.R. Giese, F.J. Lamelas, H.A. Owen, R. Plass, M. Gajdardziska-Josifovska, Surf. Sci., 457 (2000) 326-336.

[30] R. Plass, J. Feller, M. Gajdardziska-Josifovska, Surf. Sci., 414 (1998) 26-37.

[31] V.E. Henrich, Surf. Sci., 57 (1976) 385-392.

[32] S. Hwan Moon, T. Wook Heo, S. Young Park, J. Hyuk Kim, H. Joon Kim, J. Electrochem. Soc., 154 (2007) J408-J412.

[33] C.H. Lei, G. Van Tendeloo, M. Siegert, J. Schubert, J. Mater. Res, 17 (2002) 1923-1931.

[34] Toshiharu Minamikawa, Tenmin Suzuki, Yasuto Yonezawa, Kazuhito Segawa, Akiharu Morimoto and Tatsuo Shimizu, , Jpn. J. Appl. Phys., 34 (1995) 4038-4042.

[35] F. Ahmed, K. Sakai, H. Ota, R. Aoki, N. Ikemiya, S. Hara, J. Low Temp. Phys., 105 (1996) 1343-1348.

[36] C.W. Zhao, Y.M. Xing, P.C. Bai and L.F. Wang, Chin. Opt. Lett., 6 (2008) 179–182.

[37] L. Pham Van, O. Kurnosikov, J. Cousty, Surf. Sci., 411 (1998) 263-271.

[38] J.C.P. Y. Oishi and W. D. Kingery, 33, 905–906, Sept. 1960, Vacuum, 10 (1960) 402.

[39] Han-Ill Yoo, Bernhardt J. Wuenschb, William T. Petuskeyc, Solid State Ionics, 150 (2002) 207-221.

[40] Y. Oishi, K. Ando, H. Kurokawa, Y. Hiro, J. Am. Ceram. Soc. 66 (1983) C60.

[41] H. Matzke, in: L.-C. Dufour, C. Monty, G. Petot-Ervas (Eds.) Surfaces and Interfaces of Ceramic Materials, Springer Netherlands, 1989, pp. 241-272.

[42] O. Kurnosikov, L. Pham Van, J. Cousty, Surf. Sci., 459 (2000) 256-264.

[43] V. Marchenko, J. Exp. Theor. Phys., 81 (1981) 1141.

[44] S. Song, M. Yoon, S. Mochrie, G. Stephenson, S. Milner, Surf. Sci., 372 (1997) 37.

[45] J.J. Metois, A. Saul, P. Muller, Nat Mater, 4 (2005) 238-242.

[46] Hyeong-Chai Jeong, Ellen D. Williams, Surf. Sci. Rep., 34 (1999) 171-294.

[47] K. Sudoh, H. Iwasaki, E.D. Williams, Surf. Sci., 452 (2000) L287-L292.

[48] X.S. Wang, J.L. Goldberg, N.C. Bartelt, T.L. Einstein, E.D. Williams, Phys. Rev. Lett., 66 (1991) 677-677.

[49] A. Rokosz, P. Strycharski, Z. Anal. Chem., 313 (1982) 316-318.

[50] M.H. Leipold, J. Am. Ceram. Soc., 49 (1966) 498-502.

[51] S. Riyadi, Thesis, (2012) 122.

[52] M. Gajdardziska-Josifovska, P.A. Crozier, M.R. McCartney, J.M. Cowley, Surf. Sci., 284 (1993) 186-199.

[53] R. Souda, Y. Hwang, T. Aizawa, W. Hayami, K. Oyoshi, S. Hishita, Surf. Sci., 387 (1997) 136-141.

[54] N. Ravishankar, C.B. Carter, J. Mater. Res., 17 (2002) 98-106.

[55] A.D. Polli, T. Wagner, M. Rühle, Surf. Sci., 429 (1999) 237-245.

[56] V. Vágvölgyi, R.L. Frost, M. Hales, A. Locke, J. Kristóf, E. Horváth, J. Therm. Anal. Calorim., 92 (2008) 893-897.

[57] Y. Sawada, K. Uematsu, N. Mizutani, M. Kato, Thermochim. Acta, 27 (1978) 45-59.

[58] Y. Sawada, K. Uematsu, N. Mizutani, M. Kato, J. Inorg. Nucl. Chem., 40, 979–982 (1978).

[59] Y. Sawada, J. Yamaguchi, O. Sakurai, K. Uematsu, N. Mizutani, M. Kato, Thermochim. Acta, 32 (1979) 277-291.

[60] L. Haurie, A.I. Fernández, J.I. Velasco, J.M. Chimenos, J.-M. Lopez Cuesta, F. Espiell, Polym. Degrad. Stab., 91 (2006) 989-994.

[61] L.A. Hollingbery, T.R. Hull, Thermochim. Acta, 509 (2010) 1-11.

[62] H.B. Yao, Y. Li, A.T.S. Wee, Appl. Surf. Sci., 158 (2000) 112-119.

[63] D. Aswal, K. Muthe, A. Singh, S. Sen, K. Shah, L. Gupta, S. Gupta, V. Sahni, Physica C: Superconductivity, 363 (2001) 208-214.

[64] Hong-Liang Lu, Shi-Jin Ding, David Wei Zhang, Electrochem. Solid-State Lett., 13 (2010) G25-G28.

[65] C.D. Wagner, W.M. Riggs, L.E. Davis, J.F. Moulder, J.E. Mullenburg Handbook of the X-ray Photoelectron Spectroscopy, Perkin-Elmer, Eden Draivie, MN, (1979).

[66] D. Briggs, M.P. Seath, Wiley, New York, (1983).

Chapter 5

Magnetic and transport properties of epitaxial stepped Fe_3O_4 (100) thin films

5.1 Introduction

Ferromagnetic thin films grown expitaxially on vicinal substrate surfaces have attracted much attention recently due to their interesting magnetic and transport properties [1-12] and potential for applications in spintronics [13]. Most studies focus on anisotropy induced by step arrays, particularly metallic films on stepped surfaces, such as Fe on stepped Ag [2-4], Au [4], W [5-7], and Si [12], $Fe_{1-x}Co_x$ on stepped GaAs [8], Co on stepped Cu [9, 10], and $CoPt_3$ on stepped MgO [11]. However, the alignment of the magnetization easy axis, associated with this step induced anisotropy, is debatable. It is sometimes parallel to the step edges and other times perpendicular to them. Magnetite, Fe_3O_4, is an important transition metal oxide with a nearly fully spin polarized electron band at the Fermi level (half-metallic character) and a high Curie temperature of 858 K, which make it a promising candidate for room temperature spintronic devices and applications [14-16]. Recently, interesting magnetic and transport properties in Fe_3O_4 have been reported, i.e., magnetism in nanometer-thick magnetite [17], large orbital moment in nanoscale magnetite [18], giant magnetization in nanometer-thick magnetite [19], a spin Seebeck effect [20], a spin filter effect [21], electrical field-induced phase transition [22-24], large transversal magnetoresistance [25, 26], and spin valve effect [27-29]. However, initial efforts in exploiting its half metallic nature in magnetic tunnel junctions (MTJ) have been far from promising [28, 29]. The presence of anti-phase boundaries (APBs) defects in Fe_3O_4 contributes to its unusual magnetic and transport properties, such as the magnetization non-saturation even at very high field [30, 31], the super-paramagnetic behaviour in Fe_3O_4 films [32, 33], and a greater MR response across the AF-APBs [34-36]. On the other hand, in polycrystalline Fe_3O_4 thin films, interesting properties such as magnetic-transport [37], spin-injection [38] and charge ordering [39, 40] have also been investigated and discussed. Therefore, it is worth investigating the magnetic properties of stepped epitaxial Fe_3O_4 films produced on large miscut angle vicinal MgO substrates, as a high density APBs is expected along the step edges. Moreover, this arrangement could be useful to help understand the effects of APBs on the conduction mechanisms within Fe_3O_4 and its metal to insulator transition (Verwey transition).

This chapter describes how we fabricated epitaxial stepped Fe_3O_4 thin films of different thicknesses and provides details of their magnetic and transport properties. The morphology of Fe_3O_4 thin films was characterized by atomic force microscopy (AFM) and high resolution scanning transmission electron microscopy (STEM). The M (H) measurements suggest that the steps induce additional anisotropy which has its easy axis perpendicular to steps and the hard axis along the steps. Local transport measurements suggest that the step induced anisotropy is mainly due to APBs formed at the step edges.

5.2 Experimental part and contact fabrication

To grow stepped Fe_3O_4 films, the first step is to prepare a stepped MgO (100) substrate. In this work, we used single-side polished MgO (100) single crystalline substrates with a miscut angle of 2.8° along the <010> direction. The steps were produced by annealing the substrates in air in a furnace at high temperature. The terrace width and height of the steps were tuned by selection of the substrate annealing temperature and time. To produce uniform, regular and straight steps on MgO surface for this study, the MgO substrates were annealed at 1300°C for 3 hours. Figure 5.2(a) shows a typical AFM image of a stepped MgO substrate annealed at 1300°C for 3 hours. Uniform, regular, and straight steps can be clearly observed and steps are parallel to <010> direction. The terrace width for this substrate is around 160 nm. The Fe_3O_4 films with different thicknesses were grown on stepped MgO substrates using oxygen plasma assisted molecular beam epitaxy (MBE) with a base pressure of 3×10^{-10} Torr. Films with thicknesses of 5, 10, 15 and 20 nm were grown for magnetization measurements. To insure the growth conditions were the same for films with different thickness, the Fe_3O_4 layers were grown on the same MgO substrate using a shadow mask inside the MBE system. Several films with a thickness of 60 nm were also prepared for electrical measurements. After annealing in air to produce steps, the substrates were chemically cleaned prior to insertion into the growth chamber and were further annealed at 600°C in UHV for 30 minutes and subsequently annealed in oxygen at a partial pressure of 1.3×10^{-5} Torr for 2 hours. The Fe_3O_4 films were grown by electron beam evaporation of metallic iron (99.999%) in the presence of free oxygen radicals generated by an electron cyclotron resonance plasma source with a growth rate of 0.3 Å/s. The substrate temperature during growth was kept at 250°C. Reflection high energy electron diffraction (RHEED) was employed to confirm the epitaxial growth and establish the growth mode. Details of the film growth is given elsewhere [19, 26, 27].

5.2.1 Electron beam lithography (EBL)

Further we fabricated electrode patters for the transport measurement. Description of contact fabrications are followed by few steps and we described it in details. First of all, triangle nano-gap shaped electrodes were designed by Raith software and so that electrodes would be aligned along the steps and perpendicular to the steps (see Figure 5.2(a)). Secondly, Electron beam lithography (EBL) has been used to fabricate the small metal electrode pattern. The EBL was performed using a Carl Zeiss SUPRA40 equipped with a Raith50 electron lithography tool. After cleaning the sample in acetone and IPA, PMMA A-3 (poly methyl methacrylate) was spin coated onto the thin film at 3000 rpm for 45 seconds (thickness around 150 nm) followed by baking at 180°C for 1 minute on a hotplate. A 15 keV accelerating voltage was used to expose the resist with 20 pA of current and an area dose of 130 $\mu C/cm^2$. The two probe electrode patterns are then defined by opening a window in the PMMA resist via EBL writing. Once the sample was exposed to the electron beam, electrode designs was developed by a mixture of MIBK and IPA (1:3) for 45 sec, kept in IPA for 15 sec, and then blown dry with nitrogen.

Metals were deposited by electron beam deposition in a Temescal FC-2000 e-beam system, which has 6 different metal pockets. The bottom evaporated electrode was made of 5 nm of Ti (as an adhesion layer) followed by 35 nm of evaporated Au to protect the Ti electrodes from oxidation. The metallization is performed at pressures less than 6×10^{-7} Torr with a deposition rate of 1 Å/s for both electrodes. After the metallization, the sample was kept in acetone for one hour and then washed with IPA and blown dry with nitrogen. As shown in Figure 5.1(b) the fabricated electrode patterns were checked gap and right placement of electrodes on step region with scanning electron microscopy (SEM)

5.2.2 UV lithography

Small electrodes fabricated by electron beam lithography (EBL) were connected to 7×7 mm sized pads made by UV lithography (see Figure 5.1(e) and (f)). After cleaning the sample gently with Acetone and IPA, it was spin coated using positive photoresist (Shipley S1813) at 3000 rpm for 45 seconds followed by baking on a hotplate at 115°C for one minute. Before exposing to UV light we aligned alignment marks (crosses) on the sample which was made by EBL. The sample was then exposed to UV radiation through a Karl Suss MJB-3 UV400 mask aligner for 16 seconds. Finally the samples were developed in the developer MF319 for 45 seconds and rinsed with deionized water (DI) water followed by blow drying with nitrogen. The UV patterns were checked with optical microscopy. After developing, metals were deposited on the sample by electron beam deposition. 20 nm of Ti was used as an adhesion layer then 20 nm of Au was used to protect the Ti electrodes from oxidation. The electron beam deposition was performed at pressures of less than 6×10^{-7} Torr and the deposition rate was 1 Å/s. After metallization, the sample was kept in acetone for 2 hours for lift-off, and then gently blown with a plastic pipe keeping the sample in the acetone. Sometimes it was difficult to lift-off and metal still remained in unwanted places on the sample. For these samples it was necessary to keep them in acetone for a longer duration. Finally, it was rinsed with IPA and blown with nitrogen gas. Finally, nano-gap contacts were scanned by atomic force microscopy (AFM) by showing a pair of contacts placed (c) along the steps and (d) perpendicular to the steps.

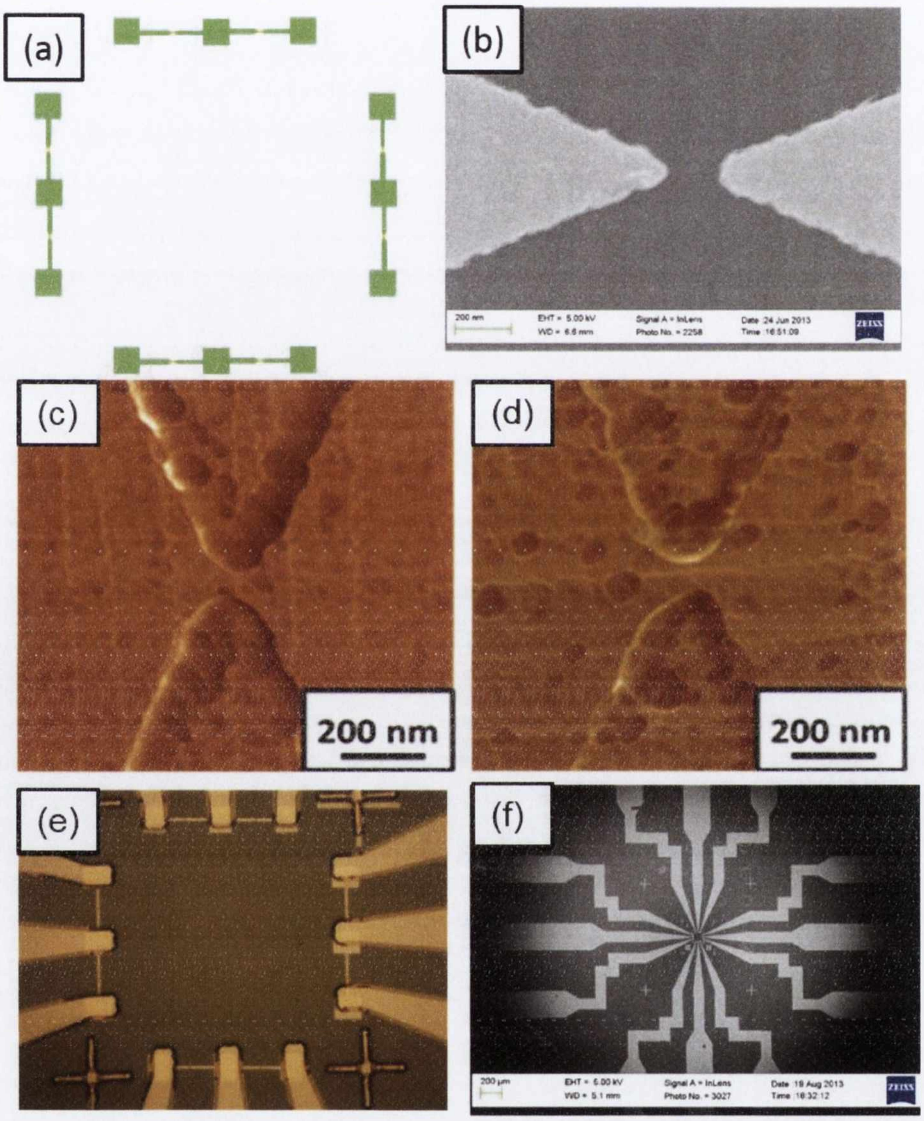

Figure 5.1(a) Design of triangle shape electrodes drawn by Raith software (b) SEM image of electrode pattern fabricated by electron beam lithography (EBL) (e) Optical microscopy image of the large electrodes pattern connected to the small electrode patters for the contacting with silver wires (f) SEM image of zoom are of image (e). 1×1 μm^2 AFM images with a pair of nano-gap contacts placed (c) along the steps and (d) perpendicular to the steps.

5.3 Results and discussion

Figure 5.2(b) shows a 4×4 μm^2 AFM image of 60 nm thick Fe_3O_4 deposited on a stepped MgO substrate. It is clear the film keeps the morphology of the substrate. The steps remain parallel to the <010> direction, and the terrace width and height of the steps are around 160 nm and 8 nm, respectively. To further demonstrate the stepped structure of the Fe_3O_4 films, we show in Figure 5.2(d) a low-magnification high angle angular dark field (HAADF) STEM image of the whole depth of the Fe_3O_4 thin film (bright) on the MgO substrate (dark). One can clearly see that the Fe_3O_4 films were epitaxially grown on the MgO substrates and the Fe_3O_4 thin films do have a stepped character. One can also see from Figure 5.2(d) that the interface between Fe_3O_4 and MgO is coherent and defect free. We also show a high resolution STEM image in Figure 5.2(c), which further demonstrates the epitaxial nature of the films even at the step edges.

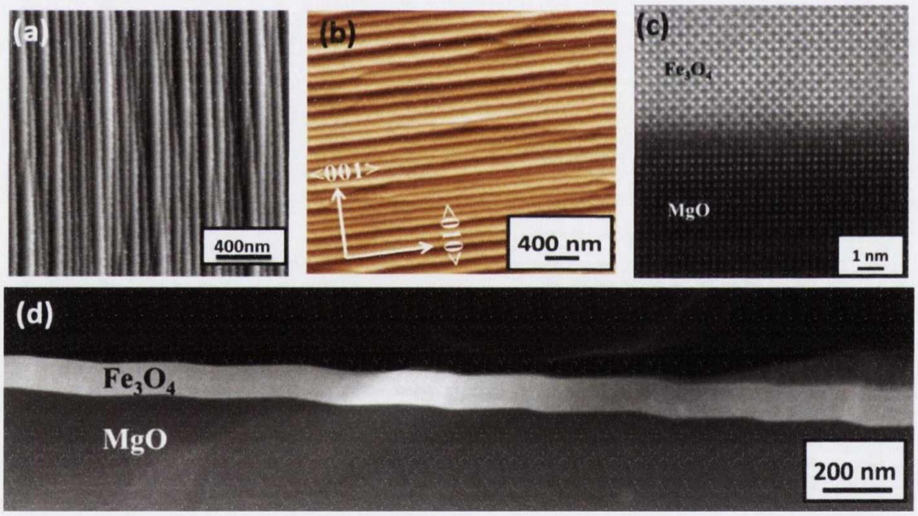

Figure 5.2(a) An AFM image of a MgO substrate with a miscut angle of 2.8° annealed at 1300°C for 3 hours. The steps are parallel to <010> direction. (b) A 4×4 μm^2 AFM image of a 60 nm thick Fe_3O_4 deposited on a stepped MgO substrate. The steps are parallel to <010> direction. (c) High resolution STEM image indicating the epitaxial growth of Fe_3O_4 on stepped MgO substrate. (d) Low magnification STEM image demonstrating the epitaxial growth of stepped Fe_3O_4.

Figure 5.3 shows M (H) loops of stepped Fe_3O_4 thin films measured at room temperature using a Physical Property Measurement System (PPMS) (Quantum Design) equipped with a 14 T superconducting magnet. The magnetic field was applied in-plane along the steps (AL), i.e., along <010> and perpendicular to the steps (PS). The room temperature saturation magnetizations for the 5, 10, 15, and 20 nm thick stepped Fe_3O_4 film are 450, 465, 475, and 480 emu/cm [1], respectively, which are less than the bulk value. The reduced saturation magnetization is due to the presence of antiferromagnetic the anti-phase boundaries formed at the step edges [33]. A significant difference between M (H) loops for the orthogonal field directions can be clearly observed in Figure 5.3. For the 5 nm Fe_3O_4 film with the field perpendicular to the steps, the coercivity field is 65 Oe. While for the field along the steps, the coercivity field is only 33 Oe. Moreover, the M (H) loop for the field perpendicular to the steps is much squarer than for field applied along steps. Similar behavior was observed for all the films. It is clear that the easy axis, for all the films grown, is perpendicular to the steps and hard axis is along the steps.

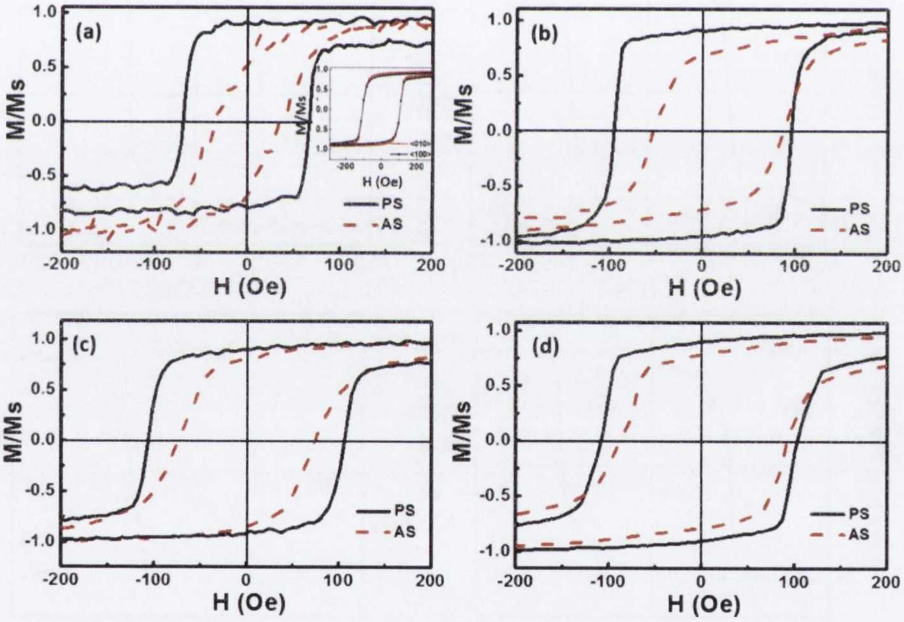

Figure 5.3 M (H) loops measured at room temperature with the in-plane magnetic field applied along the steps (red dashed lines) and perpendicular to the steps (black-solid lines). The thicknesses of the magnetite films are 5 nm (a), 10 nm (b), 15 nm (c), and 20 nm (d), respectively. Inset: M (H) loops for 5 nm thick Fe3O4 film without steps with the field is applied along the <100> and <010> directions.

We can also see from Figure 5.3 that, with increasing film thickness, the difference in the M (H) loops for two field directions decreases. In contrast to stepped samples, the inset of Figure 5.3 (a) shows M (H) loops of a 5 nm Fe_3O_4

film without steps, fabricated with the same conditions. There is no discernible difference between the M (H) loops for the two field directions. The M (H) measurements on stepped Fe_3O_4 thin films were also performed at a variety of temperatures.

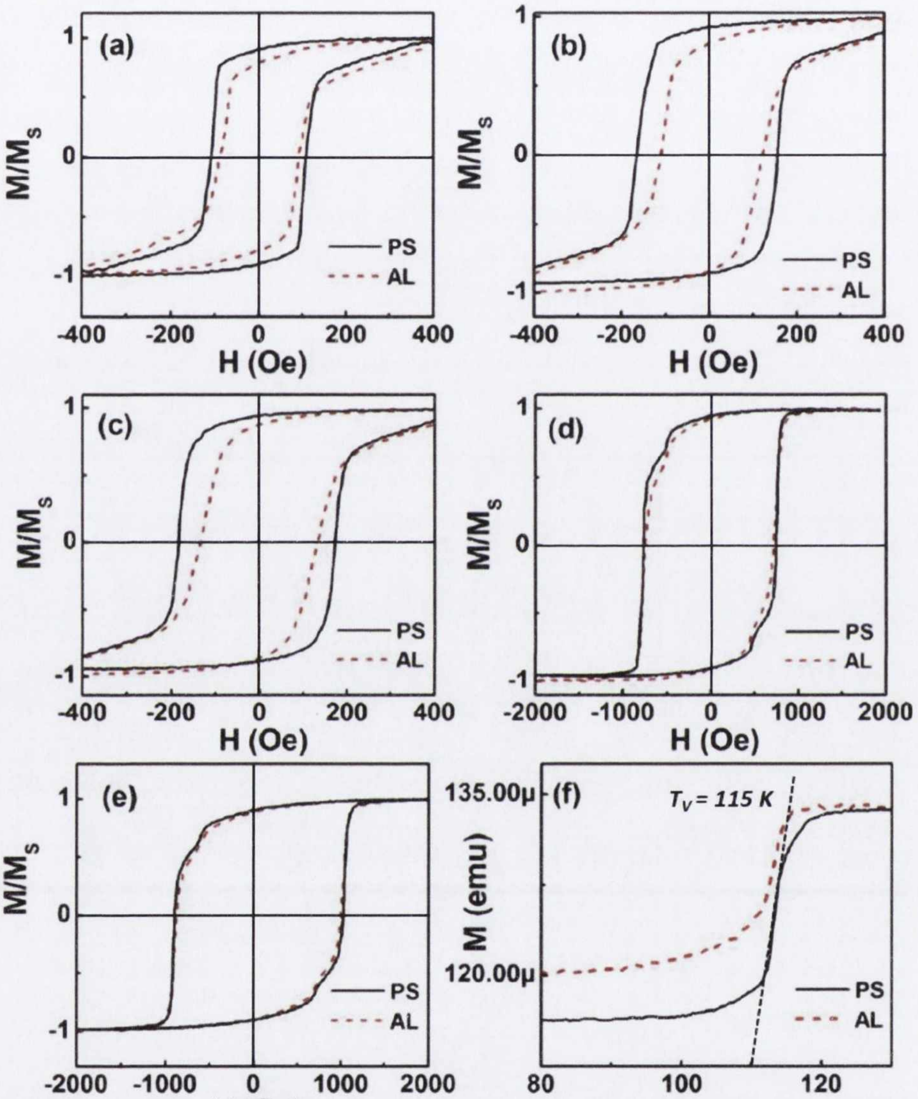

Figure 5.4 M (H) loops with an in-plane magnetic field applied along the steps (red-dashed lines) and perpendicular to the steps (black-solid lines) measured at 300K (a), 200K (b), 150K (c), 100K (d), and 50K (e), respectively. The thickness of the measured magnetite film is 20 nm. (f) M-T curves measured at an in-plane field of 200 Oe applied along the steps (red-dashed lines) and perpendicular to the steps (black-solid lines).

Figures 5.4(a)–5.4(e) show M (H) loops of 20 nm thick stepped Fe_3O_4 thin films acquired at different temperatures. Figure 5.4(f) shows the magnetization vs temperature (M-T) curves measured during the heating cycle at a field of 200 Oe applied for both orthogonal field directions. At around 115 K, the Verwey transition is clearly present, which further indicates the epitaxial nature of the stepped Fe_3O_4 film. There is a small difference in the M-T curves measured for both field directions which can attributed to different initial states as the coercivity field below the Verwey transition temperature is larger than 200 Oe. Nerveless the coercivity field of the film increases significantly across the Verwey transition and step-like features in the M (H) loops appear below the Verwey transition temperature, similar behavior was observed at all temperatures. The easy axis of the film is perpendicular to the steps and hard axis is along the steps even below the Verwey temperature. The step-like features in the M (H) loops observed in Figures 5.4(e) and 5.4(f) are mainly due to the proximity effect of anti-phase boundaries [41].

The difference in the M (H) loops can be understood by considering the preferential formation of APBs in Fe_3O_4 films during growth on stepped surfaces. Fe_3O_4 has a cubic inverse spinel structure, where Fe^{3+} ions occupy tetrahedral sites (A-sites) and octahedral sites (B-sites) are occupied by both Fe^{3+} and Fe^{2+} ions. The symmetry (Fd3m) of Fe_3O_4 is lower than that of MgO (Fm3m) and the lattice parameter of Fe_3O_4 (8.397 Å) is almost twice of that of the MgO substrate (4.213 Å). Thus, APBs will form when growing Fe_3O_4 on MgO and there is a very high chance of APB formation along step edges when growing Fe_3O_4 on stepped MgO. Let us consider the alternately positioned A- and B-sites in the (100) atomic planes of Fe_3O_4. First, examining the case of nucleation at the B-sites, there are 32 possible combinations and 16 of them have the nucleation rows of the first B-site layer on the upper terrace parallel to the ones on the lower terrace which will result in the formation of APBs. The remaining 16 combinations have the rows of the first B site layer on the upper plane but perpendicular to the rows of the first B site layer on the lower plane. Of these 16 combinations, 8 of them will result in the formation of the APBs. Similarly, considering the second case when the nucleation starts at the A-sites, there are 64 possible combinations, but only 8 combinations do not result in the formation of APBs. Therefore, there is a high chance of forming APBs along the step edges. In other words, the high density of APBs formed along the step edges is seen to be responsible for orienting the easy axis perpendicular to the steps and hard axis along the steps edges.

It is well-known that APBs are responsible for the increased resistivity in magnetite films [36, 42]. If APB density along the step edges is higher than perpendicular to steps, the resistivity measured along the step edges should be higher than that measured perpendicular to steps. To confirm this, we studied the local transport properties of 60nm thick stepped Fe_3O_4 films using sub-100 nm nano-gap contacts. Two kinds of devices were fabricated: nano-gap contacts aligned along the steps (Figure 5.1(c)) and nano-gap contacts placed perpendicular to the steps (Figure 5.1(d)). All the nanogap contacts were aligned either along the steps or perpendicular to steps. Figure 5.5(a) shows the resistivity as a function of temperature (R-T) for the two kinds of devices. One can see from Figure 5.5(a) that, above the Verwey transition temperature, the devices with nano-gap contacts placed along the steps have higher resistivity compared with those with nano-gap contacts placed perpendicular to the steps, which suggests that a high density of APBs are formed along the step edges

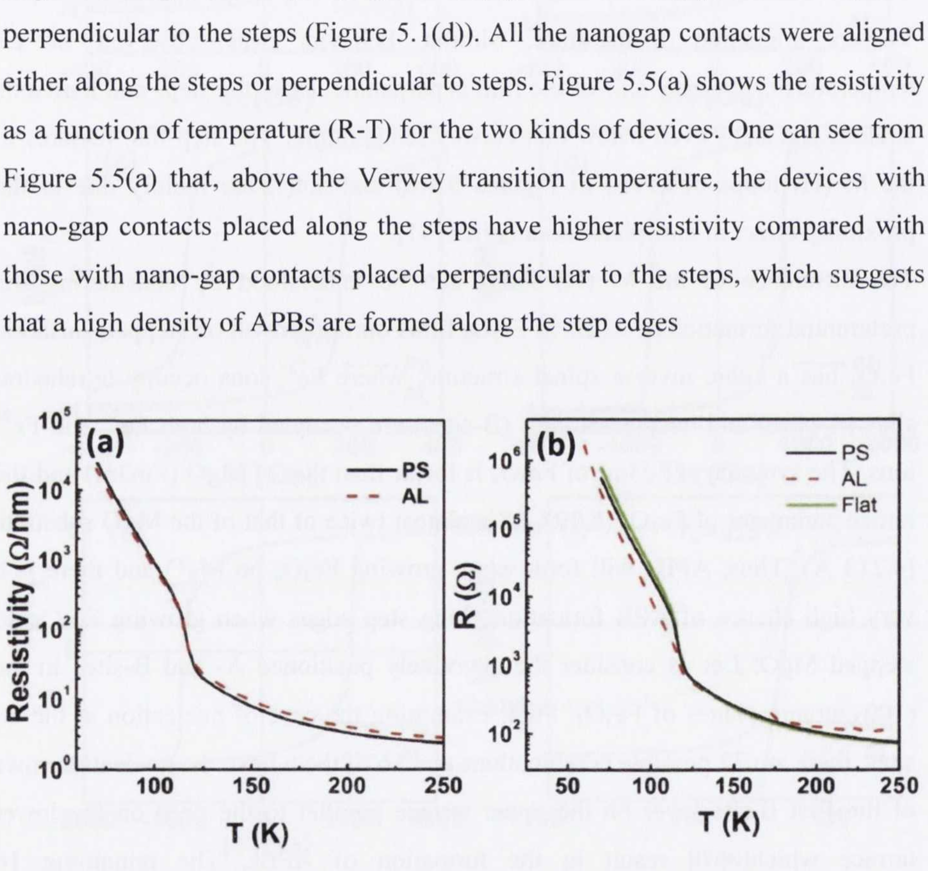

Figure 5.5(a) Resistivity as a function of temperature for both configurations with nano-gap contacts. (b) Resistance as a function of temperature for both configurations with large scale contacts and for a flat Fe_3O_4 film with large scale contacts.

Interestingly, below the Verwey transition temperature, the devices with nano-gap contacts placed along the steps have a smaller resistivity compared with the devices with nano-gap contacts placed perpendicular to the steps. Thus, it is also noted the resistivity change across the Verwey transition temperature for the devices with nano-gap contacts placed perpendicular to the steps is greater than for the devices with nano-gap contacts placed along the steps, which suggests that APBs distort the formation of long range charge-ordering in magnetite. The temperature-dependent resistivity curves can be divided into three temperature regions, i.e., T>200K (region I), 200K<T<120K (region II), and T<120K (region III), which correspond to three conduction mechanisms of magnetite [43]. We can fit the R-T curves in region II and region III with $R(\mathrm{T}) \approx R_0 \exp[(\frac{\mathrm{Ea}}{\mathrm{K_B T}})]$. Yielding activation energies Ea for the two device configurations of 48meV (AL) and 52 meV (PS) in region II and 65meV (AL) and 67meV (PS) in region III, respectively. The different activation energies for the two directions may also indicate that APBs distort long range charge-ordering formation in magnetite below and above the Verwey transition temperature. We also measured the same stepped Fe_3O_4 films with large scale contacts using the conventional four-probe method (Figure 5.5(b)). The distance between the adjacent contacts is around 1 mm. The R-T curves follow the same trend as the nano-gap contacts measurements since the steps are uniform, regular, and straight. To compare, we also measured a 60 nm flat Fe_3O_4 film with the same style of large scale contacts as for the stepped Fe_3O_4 film, with the current direction along the <001> and <010> directions. No difference in R-T curves was observed for the orthogonal current directions. Therefore, only one R-T curve for flat Fe_3O_4 film is shown in Figure 5.5(b). It can be clearly seen that the flat Fe_3O_4 film has a low resistance above the Verwey transition temperature and a high resistance below the Verwey transition temperature, which further indicates that APBs distort long range charge-ordering formation in magnetite.

5.4 Conclusion

In summary, we fabricated epitaxial stepped Fe_3O_4 thin films with different thicknesses and investigated their magnetic properties. Our magnetization measurements suggest that the steps induce additional anisotropy due to the high density of APBs formed at the step edges. Local transport measurements indicate that APBs distort the long range charge-ordering formation in magnetite.

References

[1] R. K. Kawakami, Ernesto J. Escorcia-Aparicio, and Z. Q. Qiu, Phys. Rev. Lett., 77, 2570 (1996).

[2] T. Leeb, M. Brockmann, F. Bensch, S. Miethaner, and G. Bayreuther, J. Appl. Phys., 85, 4964 (1999).

[3] J. Chen and J. L. Erskine, Phys. Rev. Lett., 68, 1212 (1992).

[4] H. J. Choi, Z. Q. Qiu, J. Pearson, J. S. Jiang, Dongqi Li, and S. D. Bader, Phys. Rev. B, 57, R12713 (1998).

[5] H. J. Elmers, J. Hauschild, and U. Gradmann J. Magn. Magn. Mater., 221, 219 (2000).

[6] D. M. Engebreston, J. Berezovsky, J. P. Park, L. C. Chen, C. J. Palmstrom, and P. A. Crowell, J. Appl. Phys., 91, 8040 (2002).

[7] R. K. Kawakami, M. O. Bowen, H. J. Choi, E. J. Escorcia Aparicio, and Z. Q. Qiu, Phys. Rev. B, 58, R5924 (1998).

[8] A Berger, U. Linke, and H. P. Oepen, Phys. Rev. Lett., 68, 839 (1992).

[9] B. B. Maranville, A. L. Shapiro, and F. Hellman, Appl. Phys. Lett., 81, 517 (2002).

[10] S. K. Arora, B. J. O'Dowd, B. Ballesteros, P. Gambardella, and I. V. Shvets, Nanotech., 23, 235702 (2012).

[11] S. Sugahara and M. Tanaka, Appl. Phys. Lett., 80, 1969 (2002).

[12] Y. Z. Wu, C. Won, and Z. Q. Qiu, Phys. Rev. B, 65, 184419 (2002).

[13] I. V. Shvets, H. C. Wu, V. Usov, F. Cuccureddu, S. K. Arora, and S. Murphy, Appl. Phys. Lett., 91, 023107 (2008).

[14] F. Walz, J. Phys.: Condens. Matter., 14, R285 (2002).

[15] M. Ziese, Rep. Prog. Phys., 65, 143 (2002).

[16] J. H. V. J. Brabers, F. Walz and H. Kronmuller, J. Phys.: Condens. Matter., 12, 5437 (2002).

[17] M. Monti, B. Santos, A. Mascaraque, O. R. Fuente, M. A. Niño, T. O. Menteş, A. Locatelli, K. F. McCarty, J. F. Marco, and J. Figuera, Phys. Rev. B, 85, 020404 (2012).

[18] W. Q. Liu, Y. B. Xu, P. K. J. Wong, N. J. Maltby, S. P. Li, X. F. Wang, J. Du, B. You, J. Wu, P. Bencok, and R. Zhang, Appl. Phys. Lett., 104, 142407 (2014).

[19] S. Arora, H. C. Wu, R. Choudhary, I. Shvets, O. Mryasov, H. Yao, and W. Ching, Phys. Rev. B 77, 134443 (2008).

[20] R. Ramos, T. Kikkawa, K. Uchida, H. Adachi, I. Lucas, M. H. Aguirre, P. Algarabel, L. Morellon, S. Maekawa, E. Saitoh, and M. R. Ibarra, Appl. Phys. Lett., 102, 072413 (2013).

[21] Z. M. Liao, Y. D. Li, J. Xu, J. M. Zhang, K. Xia, and D. P. Yu, Nano Lett., 6, 1087 (2006).

[22] J. Gooth, R. Zierold, J. G. Gluschke, T. Boehnert, S. Edinger, S. Barth, and K. Nielsch, Appl. Phys. Lett., 102, 073112 (2013).

[23] S. Lee, A. Fursina, J.T. Mayo, C.T. Yavuz, V.L. Colvin, R.G. Sofin, I.V. Shvets, D. Natelson, Nature Mater., 7, 130 (2008).

[24] J. J. I. Wong, A. G. Swartz, R.J. Zheng, W. Han, and R. K. Kawakami, Phys. Rev. B, 86, 060409 (2012).

[25] A. Fernández-Pacheco, J. M. De Teresa, J. Orna, L. Morellon, P. A. Algarabel, J. A. Pardo, M. R. Ibarra, C. Magen, and E. Snoeck, Phys. Rev. B, 78, 212402 (2008).

[26] H. C. Wu, R. Ramos, R. G. S. Sofin, Z. M. Liao, M. Abid, and I. V. Shvets, Appl. Phys. Lett., 101, 052402 (2012).

[27] H. C. Wu, O. N. Mryasov, M. Abid, K. Radican, and I. V. Shvets, Sci. Rep., 3, 1830 (2013).

[28] X. Li, A. Gupta, G. Xiao, W. Qian, and V. Dravid, Appl. Phys. Lett., 73, 3282 (1998).

[29] H. C. Wu, S. K. Arora, O. N. Mryasov, and I. V. Shvets, Appl. Phys. Lett., 92, 182502 (2008).

[30] D. T. Margulies, F. T. Parker, M. L. Rudee, F. E. Spada, J. N. Chapman, P. R. Aitchison, and A. E. Berkowitz, Phys. Rev. Lett., 79, 5162 (1997).

[31] D. T. Margulies, Parker, F. T. Spada, F. E. Goldman, R. S. Li, J. Sinclair, R. Berkowitz, A. E. , Phys. Rev. B, 53, 9175 (1996).

[32] W. Eerenstein, T. Hibma and S. Celotto, Phys. Rev. B, 70, 184404 (2004).

[33] F. C. Voogt, T. T. M. Palstra, L. Niesen, O. C. Rogojanu, M. A. James, and T. Hibma, Phys. Rev. B, 57, R8107 (1998).

[34] S. K. Arora, R. G. S. Sofin, and I. V. Shvets, Phys. Rev. B, 72, 134404 (2005).

[35] W. Eerenstein, T. T. M. Palstra, S. S. Saxena and T. Hibma Phys. Rev. Lett., 88, 247204 (2002).

[36] H. C. Wu, M. Abid, B. S. Chun, R. Ramos, O. N. Mryasov, and I. V. Shvets Nano Lett., 10, 1132 (2010).

[37] W.B. Mi, J.J. Shen, E.Y. Jiang, H.L. Bai, Acta Mater, 55 (2007) 1919-1926.

[38] L.B. Zhao, W.B. Mi, E.Y. Jiang, H.L. Bai, Appl. Phys. Lett., 91 (2007) 052113.

[39] M.S. Senn, J.P. Wright, J.P. Attfield, Nature, 481 (2012) 173-176.

[40] W. Mi, Z. Guo, Q. Wang, Y. Yang, H. Bai, Scripta Materialia, 68 (2013) 972-975.

[41] R.G.S. Sofin, H.-C. Wu, I.V. Shvets, Phys. Rev. B, 84 (2011) 212403.

[42] W. Eerenstein, T.T.M. Palstra, T. Hibma and S. Celotto Phys. Rev. B, 66, R201101 (2002).

[43] R. Ramos, S. K. Arora, I. V. Shvets, Phys. Rev. B, 78, 214402 (2008).

Chapter 6

Step induced anisotropic resistive switching in epitaxial Fe_3O_4 grown on stepped $SrTiO_3$ substrate

6.1 Introduction

Stepped and vicinal surfaces offer an interesting opportunity for use as templates for the growth of magnetic materials and manipulating them by altering the periodicity of the step edge array [1-6]. Periodicity and step height of the arrays can be effectively controlled via changing of the miscut angle and subsequent heat treatment [7, 8]. There have been a few reports on the investigation of the magnetic properties of epitaxial Fe_3O_4 thin films grown on stepped and vicinal surfaces, owing to their importance in technological applications and also from a fundamental viewpoint [2, 9-12]. The magnetic anisotropy of these films is affected by the presence of a regular step-edge array which induces a uniaxial anisotropy.

Fe_3O_4 thin films grown expitaxially on stepped and vicinal substrate surfaces have attracted much attention recently due to their interesting magnetic and transport properties [2, 9-12]. This is because due to so called Anti Phase Boundary (APB) defects, which have a higher density along the step edges when compared to the direction perpendicular to steps. The presence of anti-phase boundary defects in Fe_3O_4 contribute to its unusual magnetic and transport properties, such as the magnetization non-saturation even at very high field [13, 14] and a greater magnetoresistance (MR) response across the antiferromagnetic AF-APBs [15, 16].

Fe_3O_4, commonly known as magnetite is an important transition metal oxide with a nearly fully spin polarized electron band at the Fermi level (half-metallic character) and a high Curie temperature of 858 K, which make it a promising candidate for room temperature spintronic devices and applications [17-19]. Moreover, magnetic and transport properties in epitaxial Fe_3O_4 have been reported, i.e., giant magnetization in nanometer-thick magnetite [20], large transversal magnetoresistance (MR) [21, 22], magnetism in nanometer thick magnetite [23], large orbital moment in nanoscale magnetite [24], a spin filter effect [25], spin valve effect [26, 27], a spin Seebeck effect [28] and electrical field induced phase transition [29, 30].

RS in magnetite differs from the typical mechanisms presented when explaining resistance hysteresis. Bipolar and unipolar switching is not observed and there is no forming voltage typical for filament formation [31, 32]. The mechanism has been shown to be electrically driven [33] while joule heating only occurs in the 'ON' state. Other causes of the RS such as electrically induced changes in the Verwey temperature T_v are ruled out as an increase in T_v has only been observed under an applied electric field [34]. The resistive switching mechanism of Fe_3O_4 has been examined on flat samples [35-37]. However, there is no investigation into the resistive switching mechanism on stepped surfaces. For this reason, it is worth investigating the role of steps on the resistive switching effect.

Here I describe how stepped substrates are prepared, the growth of epitaxial Fe_3O_4 thin films on these substrates and measurements on the anisotropic resistive switching seen when using stepped surfaces. The surface morphology of $SrTiO_3$ before and after growth of Fe_3O_4 film was characterized by atomic force microscopy (AFM) and x-ray diffraction (XRD). I-V measurements along and perpendicular to steps suggested the steps induce additional anisotropy which causes a lowering of the switching voltage along the steps compared to the switching voltage in the direction perpendicular to the steps.

6.2 Results

6.2.1 Sample preparation and characterization

In this study, single crystalline $SrTiO_3$ (100) substrates with a miscut angle of 3° in the direction of <001> were used. To produce uniform and straight steps,

$SrTiO_3$ vicinal substrates were chemically cleaned and then annealed in air in a high temperature furnace at 1130˚C for 3 hours. The surface morphology of the $SrTiO_3$ vicinal substrates was examined with an Asylum Research MFP-3D Atomic Force Microscope (AFM). Figure 6.1(a) shows a typical AFM image of a single crystal $SrTiO_3$ (100) vicinal substrate after annealing. Uniform and straight steps with atomically flat terraces are formed along the direction of <010>. The steps height and width estimated from AFM characterization are ~4 nm and ~83 nm respectively. To investigate the RS behaviour, Fe_3O_4 thin films with a thickness of 95 nm were grown on stepped $SrTiO_3$ substrates using an oxygen-plasma assisted MBE system (DCA MBE M600, Finland) with a base pressure of 5×10^{-10} torr. The Fe_3O_4 films were grown by electron beam evaporation of metallic iron (99.99%) in the presence of free oxygen radicals generated by an electron cyclotron resonance plasma source with a growth rate of 0.3 Å/s. The substrate temperature during growth was kept at 250°C. Details of the film growth are given elsewhere [38, 39]. Figure 6.1(b) shows an AFM image of a 95 nm thick Fe_3O_4 film grown on the annealed stepped $SrTiO_3$ substrate. It is clear that the grown Fe_3O_4 film keeps the morphology of the substrate, where step and terraces did not change upon magnetite deposition. The steps remain parallel to the <010> direction.

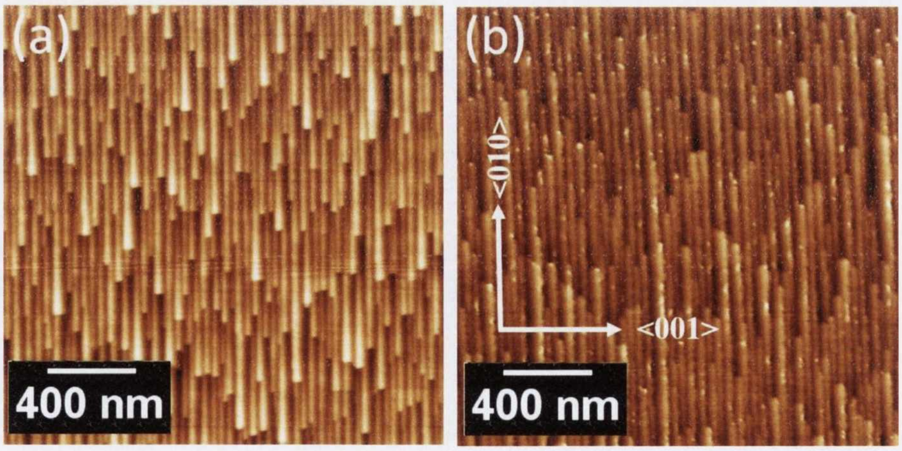

Figure 6.1 4x4 μm^2 (a) An AFM image of a $SrTiO_3$ substrate with a miscut angle of 3° annealed at 1130°C for 3 hours (b) AFM image of 95 nm thick Fe_3O_4 deposited on a stepped $SrTiO_3$ substrate. The steps are parallel to the <010> direction.

To further demonstrate the structural properties of the grown Fe_3O_4 thin films, Figure 6.2 shows full range XRD ω-2θ scan, from 10 to 100 degrees, for a 95 nm thick Fe_3O_4 film on a stepped $SrTiO_3$ substrate. Only (100), (200), and (300) peaks for $SrTiO_3$ substrate and (400) and (800) peaks for Fe_3O_4 film are observed indicating the epitaxial growth of the Fe_3O_4. The peak positions for $SrTiO_3$ (200) and Fe_3O_4 (400) located at 46.7° and 43.2° respectively, which are consistent with the well-established values. However, I could not find out what was the peak at 64°.

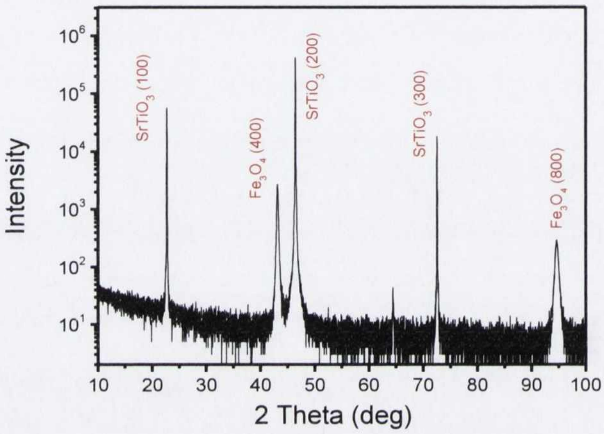

Figure 6.2 The ω-2θ scan of Fe_3O_4 film on stepped $SrTiO_3$ (100) substrate.

6.2.2 Resistive switching in magnetite

To investigate the effect of step on the RS behaviour in magnetite, I prepared devices with four probe contacts aligned either along the steps (AS) or perpendicular to steps (PS). The two outer electrodes correspond to the source lead and drain lead respectively and the two inner electrodes are used to sense the voltage drop across the contacts. A voltage is applied to the source lead with the drain grounded, and current passing through the channel is recorded. Figure 6.3(a) shows a typical SEM image of the device with four probe contacts in AS configuration. The steps between the contacts are uniform, continuous, and perpendicular to the electrodes which are critical in our study. The gaps between source and drain and the two sensing voltages are 2.03 μm and 1.15 μm respectively. The devices in this study were fabricated using standard e-beam lithography (EBL) with a positive tone resist, PMMA A3 supplied by MicroChem Corp. After development, thick metal contacts consisting of Cu (7 nm)/Au (40 nm) were deposited by e-beam evaporation, where the 7 nm thick Cu layer served as an adhesion layer for the Au contacts. Moreover, Cu has a low contact resistance with Fe_3O_4 compared to Au [40]. After lift-off with acetone, microscopy size electrodes were prepared with UV lithography. Electric characterization of the samples was performed in a closed cycle refrigeration system, with temperature varies from 50 K to 300 K.

Figure 6.3(b) shows the temperature dependent resistance measured with a constant bias current of 10 μA. The Verwey transitions for both configurations are observed at a temperature of 122 K which is close to the bulk value, thus furthering indicating the high quality of Fe_3O_4 thin films. Moreover, no significant difference in the R-T curves between two configurations has been observed which will help us to rule out any observed effect in RS due to different contacts configuration. Figure 6.3(c) shows the I-V characterization for device in AS configuration measured at 90 K. The device switches from a low conducting state to a high conducting state at a critical value (V_{SW}^{ON}) of 2.3 V which results in a sharp jump in current. Due to the effect of Joule heating, the device switches back to the low conducting state to at a critical value (V_{SW}^{ON}) of 2.3 V which is small the the (V_{SW}^{OFF}). As the distance between the two sensing contacts is around 1.15 μm, the electrical switching field is in the range of 10^4 V/cm, which is significant less than the value expected from Zener breakdown. Figure 6.3(d) shows the I-V characterization for device in PS configuration measured at 90 K. A voltage (V_{SW}^{ON}) of 3.5 V is needed to switch the device from a low conducting state to a high conducting state. It is clear, the steps induce an anisotropic behavior in resistive switching, where a higher switching voltage is required to switch Fe_3O_4 from a high conducting state to a low conducting state for electrical field applied perpendicular to the step compared to the case of electrical field applied along the step.

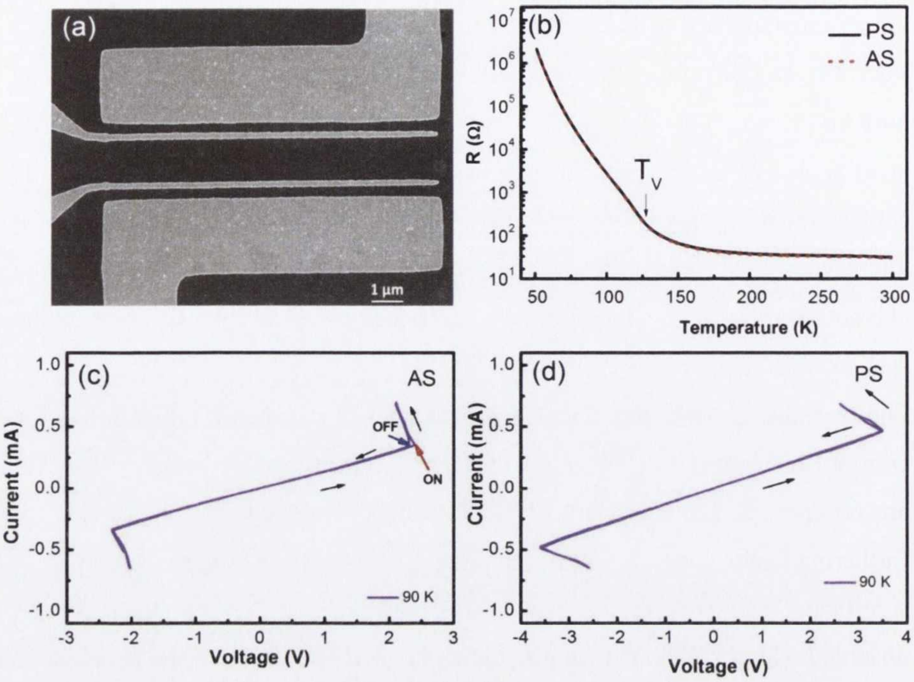

Figure 6.3 (a) SEM image of four probe electrodes on Fe_3O_4 grown on stepped $SrTiO_3$ (b) Temperature dependence of resistance demonstrated by applying current along the steps (AS) and perpendicular to steps (PS) with constant current of 10μA. The Verwey transition is shown at $T_V \sim$ 122 K (c) Demonstration of resistive switching along the steps and (d) perpendicular to the steps

Figures 6.4(a) and 6.4(b) plot the temperature dependent RS characterization for devices in both two configurations. The switching voltage increases with temperature decreasing for both configurations. I summarized the temperature dependent V_{SW}^{ON} in Figure 6.4(c). The anisotropic RS behavior has been observed at all temperatures below Verwey temperature. Moreover, the difference in V_{SW}^{ON} for both configurations increases with temperature decreasing. At 120 K, V_{SW}^{ON} for both configurations are almost the same but at 90 K, V_{SW}^{ON} for devices in PS configure is almost 50% higher than that for devices in AS configure. To demonstrate the reliability and reproducibility of the RS behaviour, a large number of switching cycles have been performed on devices in AS configure at 95 K. The V_{SW}^{ON} and V_{SW}^{OFF}at each cycle are shown in Figure 6.4(d). One can see that the RS behaviour in our devices is reliable and reproducible.

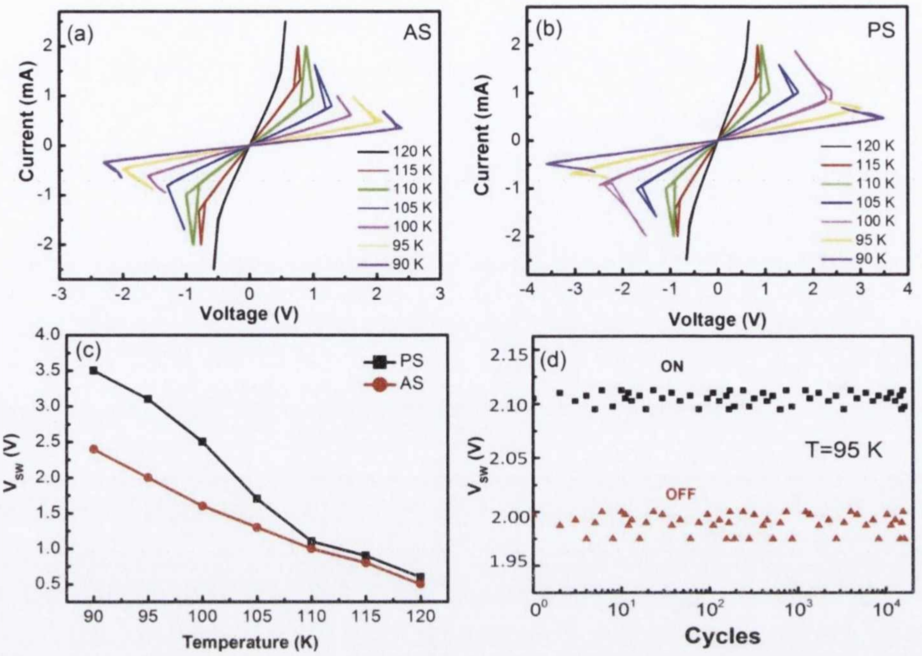

Figure 6.4. I-V measurement between temperatures 120K – 90K (a) electric field applied along the steps and (b) perpendicular to the steps. Difference in switching voltage on for the electric field applied along the steps and perpendicular to steps (c). Number of I-V cycles performed at temperature of 95K where electric field applied along the steps (d)

6.3 Conclusion

In conclusion, I have observed resistive switching on Fe_3O_4 grown on the stepped surface of $SrTiO_3$. Resistive switching has observed in both directions below the Verwey transition temperature (T_V). Because of the stepped surface, anisotropic resistive switching was seen whereby applying an electric field along the steps was lower than perpendicular to the steps in order to switch the resistance of the sample from high resistance to the low resistance. This is due to the high density of anti-phase boundaries that are aligned along the step edges. Moreover, the electric field applied along the steps was more stable in terms of damaging the sample and show more than 9,000 cycles without damage at a temperature of 95K.

References

[1] J. Oster, M. Kallmayer, L. Wiehl, H.J. Elmers, H. Adrian, F. Porrati, M. Huth, J. Appl. Phys., 97 (2005).

[2] H.C. Wu, A. Syrlybekov, O. Mauit, A. Mouti, C.Ó. Coileáin, M. Abid, M. Abid, I.V. Shvets, Appl. Phys. Lett., 105, 13 (2014).

[3] R. Kawakami, E. Escorcia-Aparicio, Z. Qiu, Phys. Rev. Lett., 77 (1996) 2570-2573.

[4] V. Usov, S. Murphy, I.V. Shvets, J. Appl. Phys., 95 (2004) 7312-7314.

[5] T. Leeb, M. Brockmann, F. Bensch, S. Miethaner, G. Bayreuther, J. Appl. Phys., 85 (1999) 4964-4966.

[6] B.B. Maranville, A.L. Shapiro, F. Hellman, D.M. Schaadt, E.T. Yu, Appl. Phys. Lett., 81 (2002) 517-519.

[7] R. Verre, R.G.S. Sofin, V. Usov, K. Fleischer, D. Fox, G. Behan, H. Zhang, I.V. Shvets, Surf. Sci., 606 (2012) 1815-1820.

[8] S. Benedetti, P. Torelli, P. Luches, E. Gualtieri, A. Rota, S. Valeri, Surf. Sci., 601 (2007) 2636-2640.

[9] S. K. Arora, R. G. S. Sofin, and I. V. Shvets, Phys. Rev. B, 72, 134404 (2005).

[10] V.O. Golub, V.V. Dzyublyuk, A.I. Tovstolytkin, S.K. Arora, R. Ramos, R.G.S. Sofin, I.V. Shvets, J. Appl. Phys., 107, 09B108 (2010).

[11] L. McGuigan, R.C. Barklie, R.G.S. Sofin, S.K. Arora, I.V. Shvets, Phys. Rev. B, 77 (2008) 174424.

[12] R.G.S. Sofin, S.K. Arora, I.V. Shvets, J. Appl. Phys., 97, 10D315 (2005).

[13] D. T. Margulies, F. T. Parker, M. L. Rudee, F. E. Spada, J. N. Chapman, P. R. Aitchison, and A. E. Berkovitz, Phys. Rev. Lett., 79, 5162 (1997).

[14] D. T. Margulies, Parker, F. T. Spada, F. E. Goldman, R. S. Li, J. Sinclair, R. Berkowitz, A. E. , Phys. Rev. B, 53, 9175 (1996).

[15] W. Eerenstein, T. T. M. Palstra, S. S. Saxena and T. Hibma Phys. Rev. Lett., 88, 247204 (2002).

[16] H. C. Wu, M. Abid, B. S. Chun, R. Ramos, O. N. Mryasov, and I. V. Shvets Nano Lett., 10, 1132 (2010).

[17] F. Walz, J. Phys.: Condens. Matter., 14, R285 (2002).

[18] M. Ziese, Rep. Prog. Phys., 65, 143 (2002).

[19] J. H. V. J. Brabers, F. Walz and H. Kronmuller, J. Phys.: Condens. Matter., 12, 5437 (2002).

[20] S. Arora, H. C. Wu, R. Choudhary, I. Shvets, O. Mryasov, H. Yao, and W. Ching, Phys. Rev. B 77, 134443 (2008).

[21] A. Fernández-Pacheco, J. M. De Teresa, J. Orna, L. Morellon, P. A. Algarabel, J. A. Pardo, M. R. Ibarra, C. Magen, and E. Snoeck, Phys. Rev. B, 78, 212402 (2008).

[22] H. C. Wu, R. Ramos, R. G. S. Sofin, Z. M. Liao, M. Abid, and I. V. Shvets, Appl. Phys. Lett., 101, 052402 (2012).

[23] M. Monti, B. Santos, A. Mascaraque, O. R. Fuente, M. A. Niño, T. O. Menteş, A. Locatelli, K. F. McCarty, J. F. Marco, and J. Figuera, Phys. Rev. B, 85, 020404 (2012).

[24] W. Q. Liu, Y. B. Xu, P. K. J. Wong, N. J. Maltby, S. P. Li, X. F. Wang, J. Du, B. You, J. Wu, P. Bencok, and R. Zhang, Appl. Phys. Lett., 104, 142407 (2014).

[25] Z. M. Liao, Y. D. Li, J. Xu, J. M. Zhang, K. Xia, and D. P. Yu, Nano Lett., 6, 1087 (2006).

[26] H. C. Wu, O. N. Mryasov, M. Abid, K. Radican, and I. V. Shvets, Sci. Rep., 3, 1830 (2013).

[27] X. Li, A. Gupta, G. Xiao, W. Qian, and V. Dravid, Appl. Phys. Lett., 73, 3282 (1998).

[28] R. Ramos, T. Kikkawa, K. Uchida, H. Adachi, I. Lucas, M. H. Aguirre, P. Algarabel, L. Morellon, S. Maekawa, E. Saitoh, and M. R. Ibarra, Appl. Phys. Lett., 102, 072413 (2013).

[29] J. Gooth, R. Zierold, J. G. Gluschke, T. Boehnert, S. Edinger, S. Barth, and K. Nielsch, Appl. Phys. Lett., 102, 073112 (2013).

[30] J. J. I. Wong, A. G. Swartz, R.J. Zheng, W. Han, and R. K. Kawakami, Phys. Rev. B, 86, 060409 (2012).

[31] K.L. Lin, T.H. Hou, J. Shieh, J.H. Lin, C.T. Chou, Y.J. Lee, J. Appl. Phys., 109 (2011).

[32] J. Yao, L. Zhong, D. Natelson, J.M. Tour, Sci. Rep., 2 (2012).

[33] A.A. Fursina, R.G.S. Sofin, I.V. Shvets, D. Natelson, Phys. Rev. B, 79 (2009).

[34] J.J.I. Wong, A.G. Swartz, R. Zheng, W. Han, R.K. Kawakami, Phys. Rev. B, 86 (2012) 060409.

[35] S. Lee, A. Fursina, J.T. Mayo, C.T. Yavuz, V.L. Colvin, R.G. Sofin, I.V. Shvets, D. Natelson, Nat Mater, 7 (2008) 130-133.

[36] J. Wei, D. Natelson, Nanoscale, 3 (2011) 3509-3521.

[37] C. Yun, X. Chen, J. Fu, C. Wang, H. Du, G. Xiong, G. Lian, Y. Yang, J. Yang, J. Appl. Phys., 113, (2013) 17C303.

[38] S.K. Arora, W. Han-Chun, Y. Hongzhi, W.Y. Ching, R.J. Choudhary, I.V. Shvets, O.N. Mryasov, Magnetics, IEEE Transactions on, 44 (2008) 2628-2631.

[39] Y. Zhou, X. Jin, I.V. Shvets, J. Appl. Phys., 95 (2004) 7357-7359.

[40] A.A. Fursina, R.G.S. Sofin, I.V. Shvets, D. Natelson, Phys. Rev. B, 82 (2010) 245112.

Chapter 7

Transport gap opening and high current on-off ratio in Bernal stacked trilayer graphene on vicinal SiC(001) substrate

7.1 Introduction

Graphene is a single-atom-thick carbon sheet with extraordinary properties unrivalled by any other known material, which will likely lead to a revolution in many areas of technology [1]. It displays a linear band dispersion [2, 3], massless Dirac fermions [4], extremely high mobility [5], and a special quantum Hall effect [4]. Potentially, graphene-based electronics could consist of just one or even a few layers of graphene; however, the absence of a band gap poses a conundrum for the implementation of conventional device architectures similar to those based on semiconducting materials [6-11]. Several methods have been proposed for opening a band gap in graphene, such as patterning single-layer graphene into narrow ribbons [12], introducing nanoholes into the graphene sheet [13], or applying a perpendicular electric field [6-11, 14-17]. Unlike bilayer graphene, gap-opening in trilayer graphene depends on the stacking order of the layers, and notably its ABA (Bernal) stacking order remains metallic even in a perpendicular electrical field [14-18]. Moreover, the fabrication and thus the stacking order of trilayer graphene devices mostly relies on the mechanical exfoliation of graphite crystals [19]. Although mechanical exfoliation of graphene from graphite is an effective and successful sample preparation method for fundamental research, it is found that roughly 60% of trilayer samples prepared by exfoliation are of purely ABA stacking order, while the rest exhibit mixed ABA-ABC stacking orders. Alternatively, chemical vapor deposition (CVD) [20, 21] and vacuum synthesis on silicon carbide surfaces [18, 22, 23] are excellent ways to fabricate large-area monolayer and few layer graphene. It is known that the graphene produced by these techniques contains grain boundaries (GBs) [23-28], which can remarkably modify the electronic transport in graphene [27, 28]. Recent theoretical investigations show that, depending on the structure of the grain-boundary, there are two distinct transport behaviors: either high transparency, or perfect reflection of charge carriers over remarkably large energy ranges [29]. Although it would provide a new way to control the charge carriers without the need to introduce bulk band gaps, there has however been no direct experimental evidence so far to support a grain boundary-induced transport gap. In this chapter, we present electrical measurements on ABA-stacked trilayer graphene synthesized on vicinal cubic-SiC(001) by thermal decomposition in ultra-high vacuum (UHV) [23, 26, 27]. Our electrical measurements give a clear demonstration of the existence of a transport gap in ABA-stacked trilayer graphene on vicinal SiC(001) with a specific preferential GB direction. These results confirm that the grain boundaries in trilayer graphene on SiC(001) perfectly reflect charge carriers over a remarkably wide range of energies (0.25 – 0.75 eV), and pave the way for tailoring the transport properties of trilayer graphene. Moreover, a high current on-off ratio of 10^4 was achieved with a voltage of 0.7 V below 50 K and with a voltage of 0.25 V at 100 K.

7.2 Experimental and device fabrication part

Uniform trilayer graphene was fabricated on SiC(001) thin films, grown on low-index and vicinal (2° miscut) Si(001) wafers, using Si-atom sublimation followed by high temperature surface graphitization in the UHV preparation chamber of a room temperature.

Electron beam lithography (EBL) has been used to fabricate the hall bar structure and nanocontacts. Firstly the fabrication procedure for the hall bar device shall be discussed. After gentle cleaning with acetone and IPA, a single layer negative tone resist ma-N 2403 supplied by MicroChem Corp was spin coated on the thin film at 3000 rpm for 30 seconds, (thickness around 300 nm) and then baked at 90°C for 1 minute on a hotplate. Two hall bar designs (so that the better one of the two could be chosen) with 500 μm separation were exposed using electron beam lithography on graphene using 15 keV accelerating voltage with area dose of 150 $\mu C/cm^2$ (in this case less dose was used in order to avoid hard baking of resist so that it would be easy to remove resist after O_2 plasma etching). The pattern used for the hall bars is shown in Figure 7.1(a). Once the sample had been exposed by the electron beam, electrode designs were developed by a ma-D 525 (TMAH based) for 60 seconds and 70 seconds in DI water, then blown dry with nitrogen. Following this procedure, areas which were exposed to the e-beam were retained while the rest of the negative tone resist is removed. Subsequently O_2 plasma etching treatment was carried out to remove unwanted graphene except in the region of the hall bar using the Diener PICO barrel Asher (for 60 sec, 8 W at P = 20 mTorr). After plasma etching, the sample was kept in acetone for 30 min and then washed with IPA, and again blown dry with nitrogen.

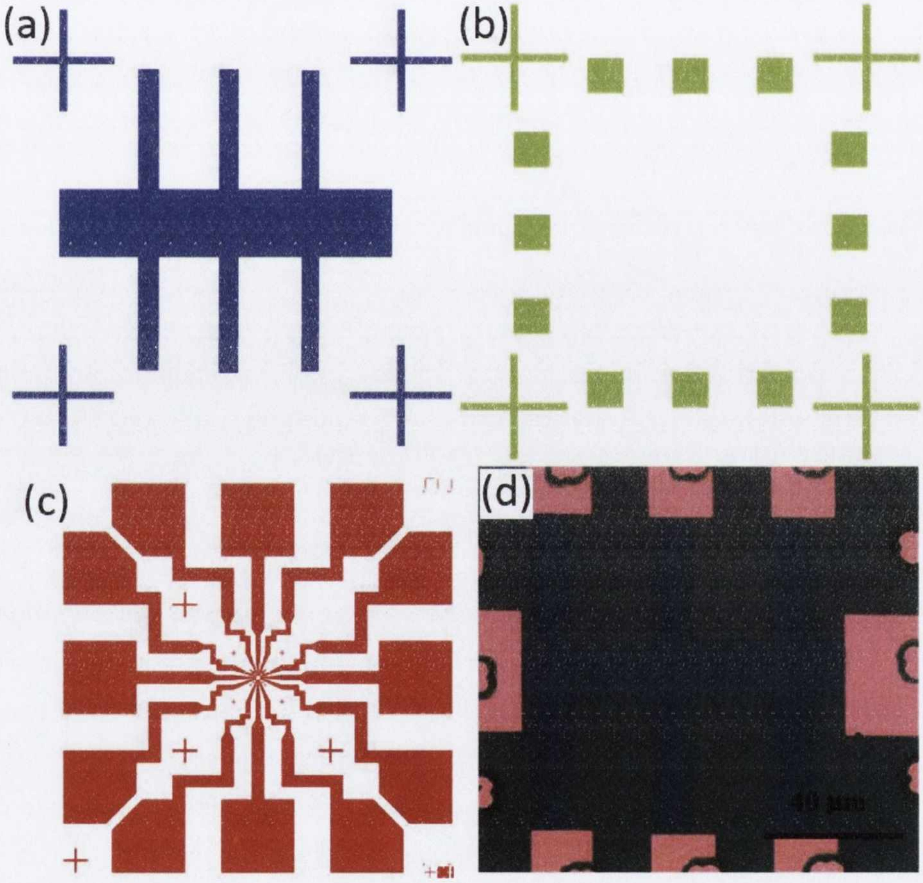

Figure 7.1 (a) Hall bar design (b) alignment marks (c) big UV design of the mask will be connected to the hall bar structure (d) final view of hall bar structure taken by optical microscope

In order to perform measurements using the hall bar device it was necessary to connect it to the larger electrodes fabricated by UV lithography. In order to carry this out, it is necessary to align the EBL pattern with a mask for UV lithography using an optical microscope. However, it was very difficult to see the positive resist coated graphene hall bar through the optical microscope due to the low contrast between the trilayer graphene and SiC. A different approach was therefore required. It was decided to use EBL once more in order to create additional alignment marks near the hall bars, which, unlike the hall bars themselves would be visible under an optical microscope. The pattern used for the alignment marks is shown in Figure 7.1(b). For the alignment marks, EBL was carried out using a positive resist, and following development depositions of 5 nm of Ti and 30 nm of Au were carried out. The final view of the hall bar structure connected to the contacts by UV lithography is shown in Figure 7.1(c). A close-up SEM image of the final hall bar structure is shown in Figure 7.1 (d)

7.3 Results and discussion

For this study, uniform trilayer graphene with a preferential GB direction was fabricated on vicinal SiC(001)/Si(001) wafers using Si-atom sublimation followed by high temperature surface graphitization in ultra-high vacuum (UHV) [23, 26, 27]. Low energy electron microscopy (LEEM), micro low energy electron diffraction (micro-LEED), scanning tunnelling microscopy (STM), and angle resolved photoelectron spectroscopy (ARPES) were used to characterize the trilayer graphene synthesized on the vicinal SiC(001). Figures 7.2(a-c) show bright-field (BF) and tilted BF LEEM micrographs and the corresponding micro-LEED patterns taken from graphene grown on the vicinal SiC(001) substrate. One can see from Figure 7.2(a) that the UHV-synthesized graphene contains intrinsic SiC antiphase domain (APD) boundaries (typical APD size for this sample is 0.5–1 μm). Figure 7.2(d) shows the electron reflectivity spectra acquired in a 7 eV energy window for different sample regions. Three grouped minima are observed across all the curves, which can be attributed to the presence of three graphene monolayers across the whole SiC surface according to references [30] and [31] A micro-LEED pattern taken from a 5×5 μm^2 surface area (inset in Figure 7.2(a)) also revealed that there are 12 double-split diffraction spots originating from the graphene layer.

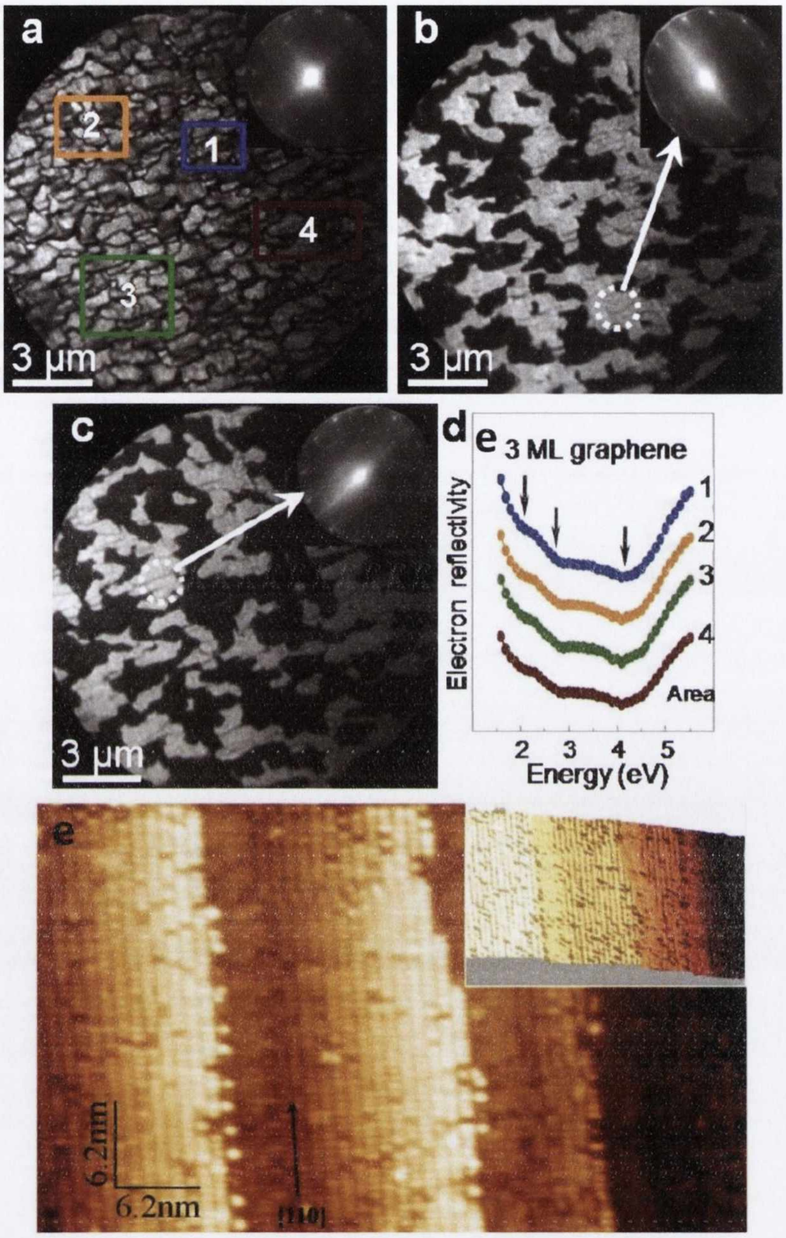

Figure 7.2 LEEM characterization of the graphene grown on vicinal SiC(001). (a) 15×15 μm^2 BF LEEM image. The dark lines in the image are the APD boundaries. Inset: micro-LEED pattern from a 5×5 μm^2 surface area. The probing area covers nanodomain systems with the lattices rotated by ±13.5° relative to the [110] and [1-10] directions. All 24 graphene spots are present in the diffraction pattern. The (1,0) and (0,1) SiC substrate spots are clearly seen. (b) and (c) tilted BF LEEM images acquired by deflecting the incident (0,0) electron beam. The reverse contrast in the images is due to the presence of two orthogonal nanodomain families. Insets: micro-LEED patterns taken from the bright areas on the corresponding LEEM images. (d) The electron reflectivity curves acquired from the areas indicated in panel (a). All curves demonstrate three consistent minima (indicated by arrows) proving the uniform trilayer thickness of the graphene overlayer. (e) 2D- and

3D-representations (inset) of a 51×31 nm^2 atomically resolved STM image of the SiC(001) 3×2 reconstruction. The image demonstrates that the step direction is close to the [110] direction of the SiC crystal lattice.

In previous STM studies [26, 27] proved that the 12 double-split diffraction spots arise from nanodomains in the graphene trilayer, which have four preferential lattice orientations. The individual micrometer-sized areas, separated by the APD boundaries, usually contain systems of nanodomains with two preferential lattice orientations rotated relative to one another by approximately 27°. According to the micro-LEED data (insets in Figures 7.2(b) and (c)) the lattices in these surface areas are rotated by ±13.5° from the two orthogonal [110] and [1-10] directions. The micro-domains are contrasted as bright and dark regions in the tilted BF LEEM micrographs.

Large area STM images in Figures 7.3(a) and 7.3(b) show that the micro-domains contain systems of nanodomains which are elongated in one direction, which is very close to one of the <110> directions and the step direction of the vicinal SiC(001) sample before graphene synthesis (Figure 7.2(e)). The trilayer graphene domains on the vicinal SiC(001) sample are self-aligned with a preferential GB direction (Figures 7.3(a) and 7.3(b)). Remarkably, those nanodomain structures are continuous even at the APD boundaries and intrinsic surface defects as observed in Figure 7.3(e). Figure 7.3(c) shows a typical STM image containing several nanometer-scale domains connected to each other through the GBs. Detailed analysis of the atomically resolved STM images measured near the GBs shows that, in most cases, the nanodomain lattices are asymmetrically rotated relative to the GBs (Figure 7.3(c)) which, in turn, are rotated by 3.5° relative to one of the <110> directions as depicted in Figure 7.3(e). In this case the lattices in neighbouring domains are rotated by 10° anticlockwise and 17° clockwise relative to the GB. This asymmetric rotation leads to the formation of a periodic structure on the GBs, with a period of 1.37 nm. The periodic structure consists of distorted heptagons and pentagons (Figure 7.3(e)), which produce modulations in the atomically resolved STM image measured at the GB (Figure 7.3(d)).

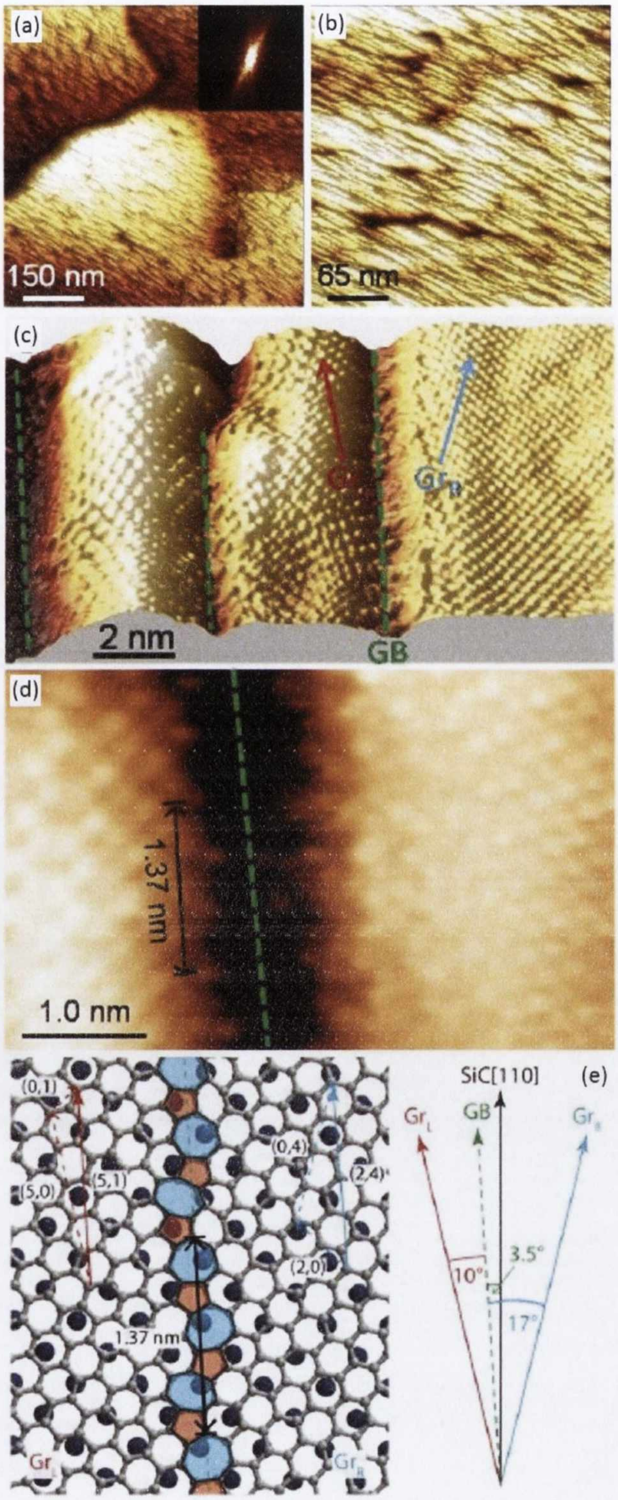

Figure 7.3 STM characterization of the graphene grown on vicinal SiC(001). (a) and (b) Large area STM images of graphene nanoribbons synthesized on the vicinal SiC(001). Inset in panel (a) proves one preferential direction of the GBs on the vicinal sample. (c) and (d) Atomically resolved STM

images of graphene nanoribbons showing the system of domains rotated 17° clockwise (GrR) and 10° anticlockwise (GrL) relative to the GB which is rotated 3.5° anticlockwise from the [110] direction (c) and the atomic structure of the GB (d). (e) Schematic model of the GB for the asymmetrically rotated nanodomains in panels (c) and (d). For the angles shown a periodic structure of distorted pentagons and heptagons is formed.

In order to extract information about the electronic structure and the stacking order of the nanostructured trilayer graphene synthesized on cubic-SiC(001), we performed ARPES measurements (Figure 7.4) and analysed the fine structure of the multiple bands seen near the K_A and $K_{B'}$ points in Figure 7.4(c).

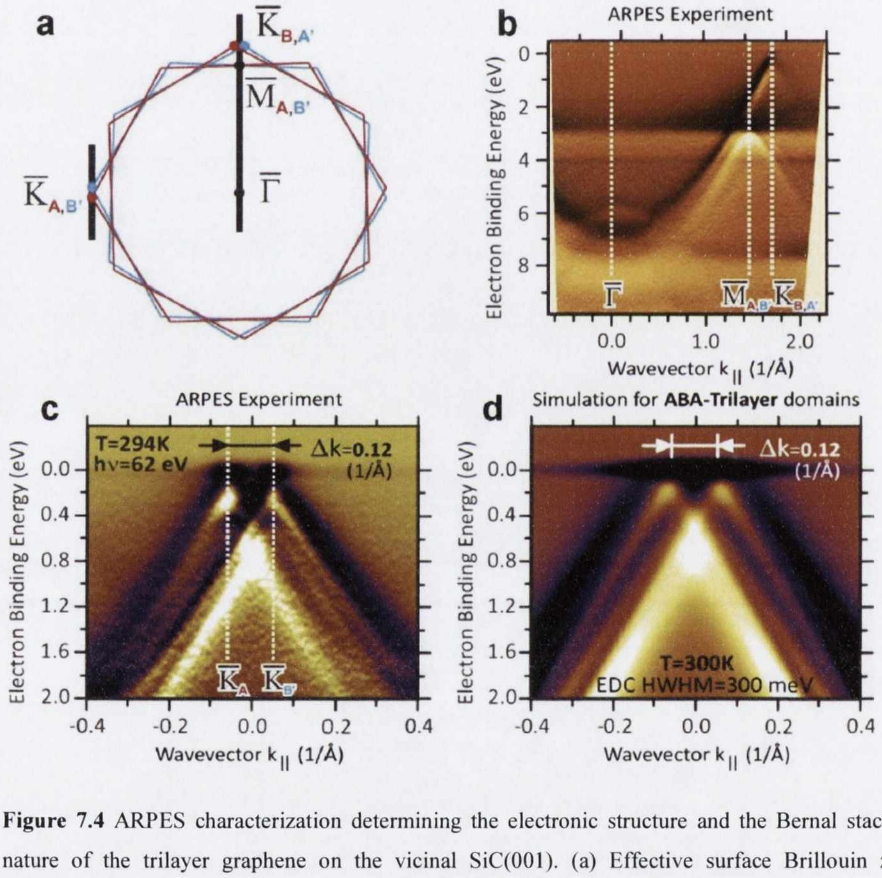

Figure 7.4 ARPES characterization determining the electronic structure and the Bernal stacking nature of the trilayer graphene on the vicinal SiC(001). (a) Effective surface Brillouin zone corresponding to four rotated domain variants. (b) and (c) Dispersions of π-band in graphene along the directions indicated in panel (a). (d) Simulations for ABA-stacked trilayer graphene with a high density of GBs. A Half Width at Half Maximum (HWHM) of 300 meV was used for the Energy Distribution Curves (EDC) to match the experimental data.

To gain a better understanding of the experimental data we performed simulations of photoemission from samples hosting two rotational domains of the trilayer, accounting for the observed momentum splitting $\Delta k=0.12$ Å^{-1}. Simulations were performed for the band structure of graphene corresponding to each of the Bernal or Rhombohedral stackings. Our simulations were set up with an enhanced photoemission peak width arising from the π-bands of the graphene trilayer. Such an assumption allows the simulation of "effective" defects (GBs) occurring in graphene. In particular, the enlarged peak width accounts for the interaction of the trilayer with the SiC substrate, as well as for geometric effects in the angular distribution of photoelectrons caused by non-systematic rotational variants and non-systematic facets. Very good correlation between measured ARPES dispersions (Figure 7.4(c)) and simulations (Figure 7.4(d)) was achieved for the full width at half maximum (FWHM) of π-bands as large as 600 meV and for an initial band structure corresponding to the ABA-trilayer. Thus it can be concluded, unambiguously, that the stacking order of the graphene trilayer on the cubic-SiC(001) is of ABA-type.

Figure 7.5(a) shows a schematic drawing of a typical graphene hall bar device. The bias voltage was applied perpendicular to the GBs to measure the local transport properties due to the GB defects. Figure 7.5(b) shows the temperature dependent resistance (R-T) measured with a bias voltage of 0.5 V. The resistance is around 1000 Ω at room temperature and increases significantly with decreasing temperature. Moreover, below 100 K, we cannot detect any reasonable current signal with a bias voltage of 0.5 V, which clearly demonstrates that the GBs induce a transport gap. We fitted the R-T curve with $R(\mathrm{T}) \approx R_0 \exp(\frac{-E_a}{\mathrm{K_B T}})$ where R_0 is the fitting parameter, K_B is the Boltzmann constant and E_a is the activation energy. The fitting gives an activation energy of 130 meV. To further demonstrate the existence of the transport gap, we measured an I-V curve at 10 K (Figure 7.5(c)) and plotted the corresponding dI/dV in Figure 7.5(d). Interestingly, for a small bias voltage, we cannot detect any reasonable current signal and the corresponding dI/dV is around 0.01 μS, indicating the existence of a transport gap. The transport gap derived from the dI/dV plot is approximately 0.7 eV at 10 K.

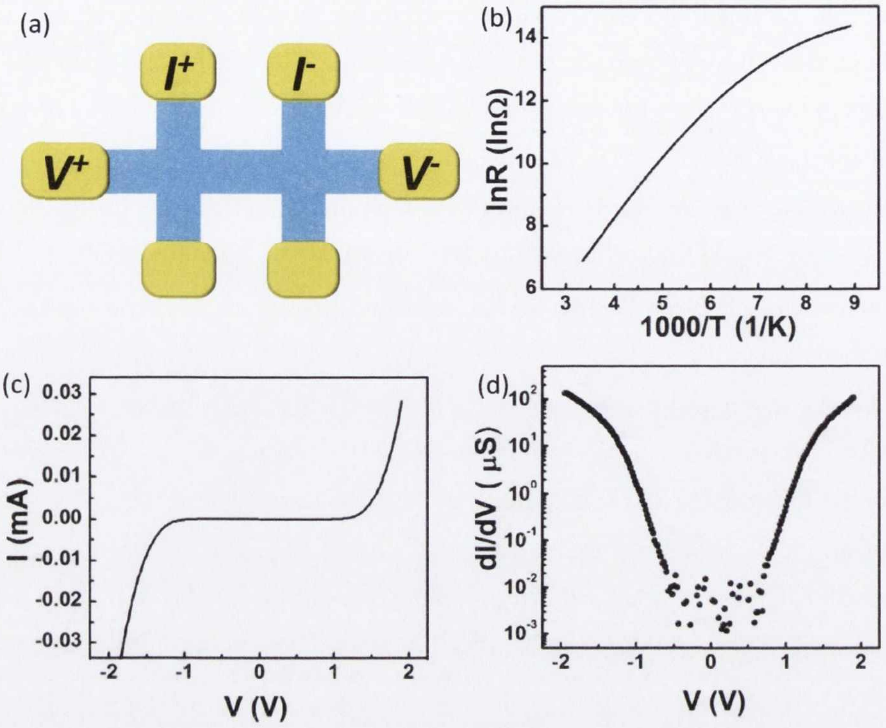

Figure 7.5 Electrical detection of the transport gap opening in Bernal stacked trilayer graphene on a vicinal SiC substrate. (a) Schematic drawing of the nano-gap device. (b) R-T curve measured with a bias voltage of 0.5 V. (c) I-V curve measured at 10 K and the corresponding dI/dV curve (d) to demonstrate the existence of a transport gap.

To further illustrate the formation of the transport gap at low temperatures, we show in Figures 7.6(a) and (b) the temperature dependent I-V curves. We also plotted the corresponding dI/dV curves in Figure 7.6(c) for temperatures below 150 K. Remarkably, the transport gap is approximately the same at 50 K and 10 K but substantially lower (0.25 eV) at 100 K. Applying a bias voltage smaller than the transport gap, the conductivity of the device is only 10^{-2} μS and increases to 10^{2} μS when the bias voltage is larger than the transport gap, which gives a high current on-off ratio of 10^{4}. Moreover, the GBs are uniform and defined by the step direction of the vicinal substrate which gives this system the potential for high-density memory applications. The observed transport gap disappears at temperatures above 150 K. It is proposed that the temperature dependence of the transport gap is related to the presence of defects in the trilayer graphene on SiC(001). It is known that defects can modify the transport properties of graphite and graphene [30]. In STM experiments (Figures 7.3(c) and 7.3(d)), we observed defects at the GBs that were found to be stable at room temperature and so cannot have an impact on the temperature dependence of the trilayer graphene's conductivity (Figures 7.6 and 7.6). However, interstitial defects in subsurface layers (Figure 7.6(d)) cannot be detected by STM but they can be anticipated by taking into account the method of graphene synthesis on SiC(001). In graphite, the migration activation energy of interstitials depends on the presence of GBs and the stress in the layer, which is usually below 0.03 eV [31-34]. In our trilayer graphene on vicinal SiC, defects and interstitials may exist which may be frozen under 100 K and migrate at higher temperatures (100-300 K) [31]. The mobility of such interstitial defects can be responsible for the disappearance of the transport gap at temperatures above 100 K (Figure 7.6). A transport gap can be opened by patterning graphene into nanoribbons [12] or the formation of periodic GBs between asymmetrically rotated graphene lattices [29]. It was suggested by Yazyev and Louie [29] that a charge transport gap of $E_g = \hbar v_F \dfrac{2\pi}{3d} \approx \dfrac{1.38}{d(\mathrm{nm})}(\mathrm{eV})$ can be formed by a non-symmetric grain boundary associated with a lattice mismatch at the boundary line, where $\hbar$ is the reduced Planck's constant, v_F is the Fermi velocity, and d is the periodicity along the GB. They also suggest that this asymmetric GB is related to out of plane buckling, which relieves the in-plane compressive strain. Figures 7.3(c) and (d), show that the boundaries of all the individual domains on SiC(001) indeed possess such a rippled morphology. Moreover, as indicated in Figures 7.3(d) and (e), the asymmetric rotation of the graphene lattices in the neighbouring domains leads to a 1.37 nm periodicity along the GB. According to the theory [29], this periodicity should produce a transport gap of approximately 1.0 eV, which can be obtained from the crossing point in ARPES dispersions. For our Bernal-stacked trilayer graphene, the crossing point in the ARPES dispersions from the rotated domains is around 0.4 eV (Figure 7.4), indicating a transport gap of 0.8 eV which is consistent with our transport measurements [29]. Therefore, our electrical, STM and ARPES characterizations support the explanation of the transport gap being based on the Yazyev and Louie theory of asymmetrically rotated domains [29] for our Bernal-stacked trilayer graphene with the GBs oriented close to the [110] direction (Figure 7.3(e)). The electron mobility in our sample is about 250 $\mathrm{cm}^2/\mathrm{Vs}$ at 10 K, which is of the same order as trilayer graphene prepared by mechanical exfoliation1. Notably, the existence of a transport gap in our trilayer graphene does not depend on the stacking order. Therefore, our experiment opens a very promising route towards semimetallic graphene, especially in trilayer graphene.

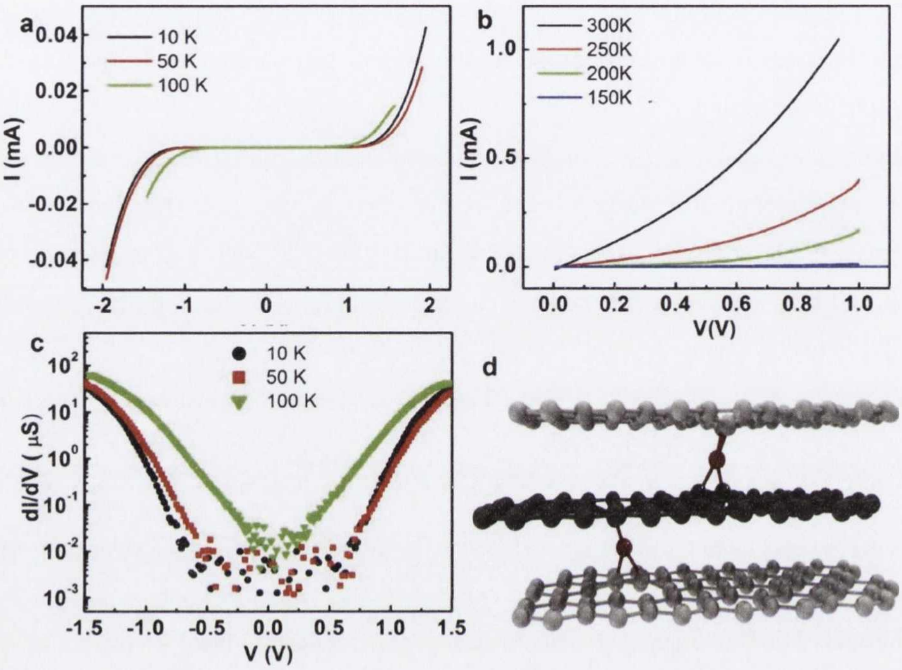

Figure 7.6 I-V curves measured at different temperatures. (a) I-V curves measured at 10 K, 50 K, and 100K. (b) I-V curves measured at 150 K 200 K, 250 K and 300K. (c) Corresponding dI/dV curves for temperatures below 150 K. (d) Schematic drawing of interstitial defects in trilayer graphene.

7.4 Conclusion

In conclusion, we have presented transport studies on trilayer graphene synthesized on vicinal cubic-SiC(001) substrates. Our electrical measurements clearly demonstrate of the opening of a transport gap in the nanostructured graphene synthesized on this stepped surface. Remarkably, the effect can be observed even at 100 K and produces a current on-off ratio of 10^4. This behavior shows that it is possible to create new tunable electronic nanostructures with graphene on cubic SiC, thus creating an opportunity for a wide range of new electronic applications.

References

[1] A.H. Castro Neto, F. Guinea, N.M.R. Peres, K.S. Novoselov, A.K. Geim, Rev. Mod. Phys., 81 (2009) 109-162.

[2] A. Bostwick, F. Speck, T. Seyller, K. Horn, M. Polini, R. Asgari, A.H. MacDonald, E. Rotenberg, Science, 328 (2010) 999-1002.

[3] K.S. Novoselov, A.K. Geim, S.V. Morozov, D. Jiang, M.I. Katsnelson, I.V. Grigorieva, S.V. Dubonos, A.A. Firsov, Nature, 438 (2005) 197-200.

[4] Y.B. Zhang, Nature, 438 (2005) 201-204.

[5] K.I. Bolotin, Sikes, K. J. Jiang, Z. Klima, M. Fudenberg, G. Hone, J. Kim, P. Stormer, H. L., Solid State Commun., 146 (2008) 351-355.

[6] E.V. Castro, Phys. Rev. Lett., 99 (2007) 216802.

[7] T. Ohta, A. Bostwick, T. Seyller, K. Horn, E. Rotenberg, Science, 313 (2006) 951-954.

[8] Y. Zhang, T.-T. Tang, C. Girit, Z. Hao, M.C. Martin, A. Zettl, M.F. Crommie, Y.R. Shen, F. Wang, Nature, 459 (2009) 820-823.

[9] K.F. Mak, C.H. Lui, J. Shan, T.F. Heinz, Phys. Rev. Lett., 102 (2009) 256405.

[10] J.B. Oostinga, H.B. Heersche, X. Liu, A.F. Morpurgo, L.M.K. Vandersypen, Nat Mater, 7 (2008) 151-157.

[11] F. Xia, D.B. Farmer, Y.-M. Lin, P. Avouris, Nano Lett., 10 (2010) 715-718.

[12] M.Y. Han, B. Özyilmaz, Y. Zhang, P. Kim, Phys. Rev. Lett., 98 (2007) 206805.

[13] A.J.M. Giesbers, E.C. Peters, M. Burghard, K. Kern, Phys. Rev. B, 86 (2012) 045445.

[14] M. Aoki, H. Amawashi, Solid State Commun., 142 (2007) 123-127.

[15] A.A. Avetisyan, B. Partoens, F.M. Peeters, Phys. Rev. B, 80 (2009) 195401.

[16] A.A. Avetisyan, B. Partoens, F.M. Peeters, Phys. Rev. B, 79 (2009) 035421.

[17] K. Zou, F. Zhang, C. Clapp, A.H. MacDonald, J. Zhu, Nano Lett., 13 (2013) 369-373.

[18] W. Bao, L. Jing, J. Velasco, Y. Lee, G. Liu, D. Tran, B. Standley, M. Aykol, S.B. Cronin, D. Smirnov, M. Koshino, E. McCann, M. Bockrath, C.N. Lau, Nat Phys, 7 (2011) 948-952.

[19] M. F. Craciun, S. Russo, M. Yamamoto, J. B. Oostinga, A. F. Morpurgo and S. Tarucha, Nat. Nano., 4 (2009) 383-388.

[20] X. Li, W. Cai, J. An, S. Kim, J. Nah, D. Yang, R. Piner, A. Velamakanni, I. Jung, E. Tutuc, S.K. Banerjee, L. Colombo, R.S. Ruoff, Science, 324 (2009) 1312-1314.

[21] S. Bae, H. Kim, Y. Lee, X. Xu, J.-S. Park, Y. Zheng, J. Balakrishnan, T. Lei, H. Ri Kim, Y.I. Song, Y.-J. Kim, K.S. Kim, B. Ozyilmaz, J.-H. Ahn, B.H. Hong, S. Iijima, Nat Nano, 5 (2010) 574-578.

[22] C. Berger, Z. Song, T. Li, X. Li, A.Y. Ogbazghi, R. Feng, Z. Dai, A.N. Marchenkov, E.H. Conrad, P.N. First, W.A. de Heer, J. Phys. Chem. B, 108 (2004) 19912-19916.

[23] V.Y. Aristov, G. Urbanik, K. Kummer, D.V. Vyalikh, O.V. Molodtsova, A.B. Preobrajenski, A.A. Zakharov, C. Hess, T. Hänke, B. Büchner, I. Vobornik, J. Fujii, G. Panaccione, Y.A. Ossipyan, M. Knupfer, Nano Lett., 10 (2010) 992-995.

[24] P.Y. Huang, C.S. Ruiz-Vargas, A.M. van der Zande, W.S. Whitney, M.P. Levendorf, J.W. Kevek, S. Garg, J.S. Alden, C.J. Hustedt, Y. Zhu, J. Park, P.L. McEuen, D.A. Muller, Nature, 469 (2011) 389-392.

[25] K. Kim, Z. Lee, W. Regan, C. Kisielowski, M.F. Crommie, A. Zettl, ACS nano, 5 (2011) 2142-2146.

[26] A. Chaika, O. Molodtsova, A. Zakharov, D. Marchenko, J. Sánchez-Barriga, A. Varykhalov, I. Shvets, V. Aristov, Nano Res., 6 (2013) 562-570.

[27] A.N. Chaika, O.V. Molodtsova, A.A. Zakharov, D. Marchenko, J. Sánchez-Barriga, A. Varykhalov, S.V. Babenkov, M. Portail, M. Zielinski, B.E. Murphy, S.A. Krasnikov, O. Lübben, I.V. Shvets, V.Y. Aristov, Nanotechnol., 25 (2014) 135605.

[28] A.W. Tsen, L. Brown, M.P. Levendorf, F. Ghahari, P.Y. Huang, R.W. Havener, C.S. Ruiz-Vargas, D.A. Muller, P. Kim, J. Park, Science, 336 (2012) 1143-1146.

[29] O.V. Yazyev, S.G. Louie, Nat Mater, 9 (2010) 806-809.

[30] Banhart, F., Kotakoski, J., and Krasheninnikov, A. V., ACS nano, 5, 26 (2011).

[31] Thrower P. A., and Mayer R. M., Phys. Stat. Sol., 47, 11 (1978).

[32] I. Suarez-Martinez, A.A. El-Barbary, G. Savini, M.I. Heggie, Phys. Rev. Lett., 98 (2007) 015501.

[33] Y. Ma, Phys. Rev. B, 76 (2007) 075419.

Chapter 8

Conclusions and outlook

Magnetite, Fe_3O_4 is an important ferromagnetic oxide and has a metal-insulator transition known as the Verwey transition. Due to its relatively high Curie temperature (858 K) and half metallic nature Fe_3O_4 attracts great interest for spin electronic applications. Moreover, Fe_3O_4 has recently demonstrated the resistive switching phenomenon. Most of these studies used magnetite in the form of thin films. Understanding the role of defects in resistive switching phenomena and to control the defect density is of great importance. Therefore, Fe_3O_4 has been used as a thin film to study the role of defects in resistive switching phenomena. The stoichiometry, strain, defect structure etc., are expected to play a crucial role in determining the electric and magnetic properties of magnetite [1]. MgO substrates are an ideal template for the epitaxial growth of Fe_3O_4 because it has a small lattice mismatch of 0.33%. However, it suffers from antiphase boundaries (APBs) which are defects occurring during growth of Fe_3O_4 on MgO. In order to control the APBs defects, we have used vicinal MgO substrates which we annealed at high temperature in order to change the surface morphology into a step and terrace structure. In this way we can control the defects densities and their direction. Trilayer graphene has attracted a lot of attention because of its unique electronic properties that are interesting both for fundamental science and for electronic applications [2-8]. The main challenges is to open a band gap [9-14]. Trilayer graphene remains metallic upon the application of an electrical field perpendicular to the graphene layers [3, 15-18]. Trilayer graphene has defects such as grain boundaries (GB) [19-24] that can change the electronic properties in graphene [23, 24]. Recent theoretical investigations show that transport gaps can be introduced and tuned by engineering periodic GBs into the graphene layers [25]. However, there is no direct experimental evidence for the existence of a transport gap.

In chapter 4 we presented the details of our investigation of high temperature annealing of vicinal MgO substrates. Single crystalline one-side polished MgO (100) substrates miscut along the <010> axis with three different miscut angles have been used. Periodicity as a function of temperature was studied at temperature ranges between 1100 – 1580°C annealed at a fixed time of 3 hours. The role of miscut was compared using 2° and 4° samples annealed at a temperature of 1200°C. Larger miscuts result in smaller step periodicity and a higher average step height. Moreover, the cross section of the faceted surface was examined using TEM and all the steps appear inclined at an angle of 10±2° with respect to the [010] direction. The role of impurities have been examined by XPS before and after annealing of samples. A small amount of Ca was detected before annealing and after annealing it increased up to 4 %. Al impurities have detected after annealing giving suggestion that it may come from the alumina tube. There was a large surface covering of hydroxyls and carbonates contaminants after a long exposure to the atmospheric environment. However, these contaminants can be removed by a short thermal treatment.

In chapter 5 we have shown fabrication of different thicknesses of expitaxially grown Fe_3O_4 on step surfaces and their magnetic properties. The morphology of Fe_3O_4 thin films were characterized by AFM and high resolution STEM. Magnetisation and electric measurements have been performed in the PPMS system. The M-H measurements show that the steps induce additional anisotropy which has its easy axis perpendicular to the steps and the hard axis along the steps. Local transport measurements with a nano-gap along the steps and perpendicular to the steps suggest that the step induced anisotropy is mainly due to APBs formed at the step edges.

In chapter 6 we have presented a study of anisotropic resistive switching in Fe_3O_4 expitaxially grown on stepped $SrTiO_3$ (100) single crystal substrates. Four – terminal measurements, RT and I-V measurements were also performed at low temperatures by applying the electric field along the steps and perpendicular to the steps. We have observed hysteresis in the I-V curves of magnetite below the Verwey transition ($T<T_V$). Furthermore, we have seen anisotropic resistive

switching when applying the electric field along the steps and perpendicular to the steps. Switching along the steps required lower voltages to switch to the lower conducting state than perpendicular to the steps. This is attributed to the high density of anti-phase boundaries present at step edges. An electric field applied along the steps was stable and shows more than 9000 cycles at 95 K.

In chapter 7 we propose a simple method to achieve a current on-off ratio of 10^4 by opening a transport gap in Bernal stacked trilayer graphene. We synthesized Bernal stacked trilayer graphene with periodic GBs on a technologically relevant vicinal cubic-SiC(001) substrate and performed electrical measurements. Our transport measurements clearly demonstrate that the GBs induce a charge transport gap larger than 0.7 eV, which agrees well with theory [25]. More remarkably, the transport gap can persist even at 100 K. Our results pave the way to create new electronic nanostructures with high current on-off ratios using graphene on cubic SiC.

8.1 Preliminary results and future work

The electronic structure of two-dimensional (2D) crystals such as graphene and molybdenum disulfide (MoS_2) depends strongly on thickness and stacking sequence of the individual layers [26, 27]. The band structure of MoS_2 and its isoelectronic compounds of the group 6 transition metal dichalcogenide (TMD) family, such as $MoSe_2$, WS_2, and WSe_2, is distinctly different from that of graphene. The 2D-layered transition metal dichalcogenide semiconductor MoS_2 has been investigated extensively over the last few years. Monolayer MoS_2 is a direct band gap semiconductor with a band gap of 1.9 eV [28], while bulk MoS_2 has an indirect band gap of 1.29 [29]. Recently, monolayer and multilayer MoS_2 have been shown to have a carrier mobilities of 200 cm^2/Vs and 100 cm^2/Vs at room temperature, respectively, and a current on/off ratio of $1x10^8$, which makes MoS_2 a promising candidate for incorporation into a new generation of more efficient transistors [30]. MoS_2 is also promising for photonic detectors, photoluminescence sensors, and integrated circuit devices owing to intriguing electrical and optical properties. In order to achieve few- or single-layer MoS_2 devices, most studies focus on mechanical exfoliation and intercalation-assisted exfoliation of bulk MoS_2, procedures whereby the lateral size and the total output of the MoS_2 films are extremely restricted. To achieve large-scale and mass production of high quality MoS_2 films on the other hand, chemical vapor deposition and physical vapor deposition methods have been demonstrated. Here we would like to demonstrate a few preliminary results of the growing multilayers of $WS_2/MoS_2/WS_2$ on the large scale 10×10 mm sample with Molecular beam epitaxial (MBE) system where growth rate can be controlled layer by layer and with good quality. Secondly, the idea behind using a stepped surface is to make nanoribbons that will be covered by multilayers on the terrace region and on the step region will not be covered by multilayers. In this way no lithography method is required to make nanoribbons and with the step surface of Al_2O_3 it can be achieved easily.

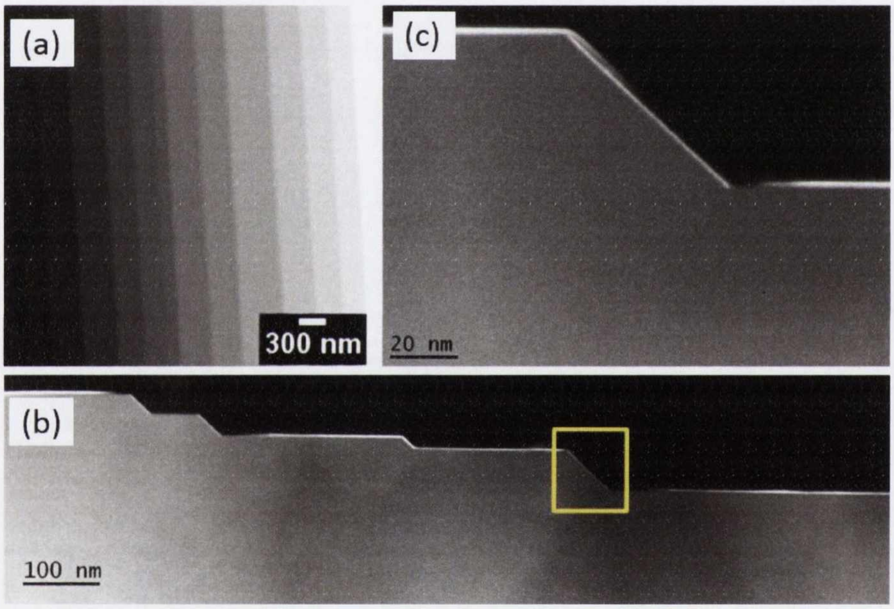

Figure 8.1 (a) 4×4 μm_2 AFM images of Al_2O_3 (0001) miscut 6° after annealing at 1550°C (b) Low-magnification HAADF image from the combined layers on stepped substrate (c) Magnified view of the outlined area in (b).

Here we would like to give a brief description how the samples were prepared and characterized them. Single crystalline one-side polished c-plane Al_2O_3 (0001) substrates miscut along the <1-210> axis with miscut angle of 6° (±0.3°) were used. The samples were cleaned in methanol, acetone and high purity propan-2-ol in an ultrasonic bath prior to annealing. Thermal treatments were performed in a high-temperature alumina tube furnace (for substrate use only). The sample was annealed at 1550°C for 15 hours in air. A heating and cooling rate of 5°C/min was used for both ramping up and down, to reach the required annealing temperature. The samples were characterized with an AFM (Asylum Research MFP-3D instrument) in tapping mode and the periodicity and height of the annealed sample were L= 330 ± 120 nm and h = 33 ± 15 nm (see Figure 8.1(a)). Subsequently, it was loaded into the MBE system for the growth of 4 monolayer W, 2 monolayer Mo and 4 monolayer W. Afterwards it was oxidized inside the MBE chamber in order to expand the unit cell of the W and Mo in order to fully sulfurize the material. For the sulfurization process a CVD chamber was used and lasted for a short time; 2 minutes at a temperature of 750°C. Once the sample was sulfurized high resolution TEM was performed on the sample. Figure 8.1(b) shows a low-magnification TEM image from the multilayers on stepped substrate. (c) Magnified view of the outlined area in (b) where no multilayer is apparent on the step region. However, when the step height is small then there will be covered with a multilayer of $WS_2/MoS_2/WS_2$.

Now we will concentrate on the terrace region where multilayers were grown. As shown from Figure 8.2, we have seen two layer and three layers of WS_2MoS_2 and $WS_2/MoS_2/WS_2$. Once the growth of the multilayer is optimised, the measurement of the electric and optical properties of the multilayer of $WS_2/MoS_2/WS_2$ will be attempted

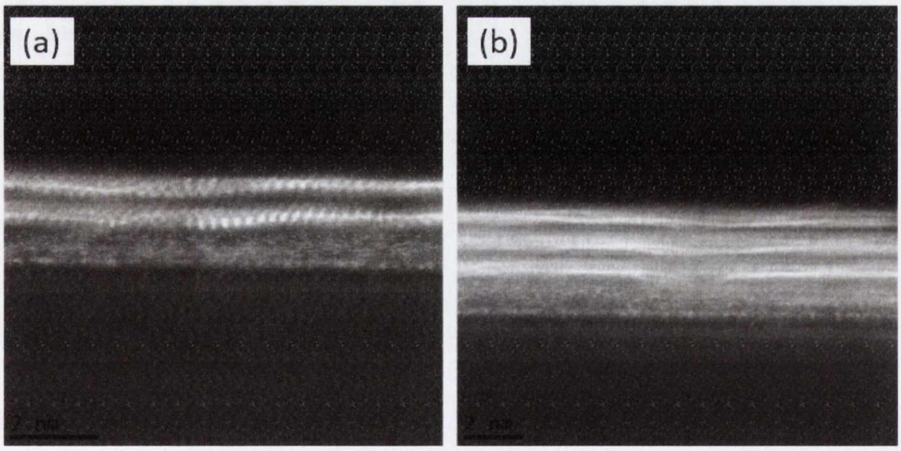

Figure 8.2 High Resolution HAADF images of two thicknesses: (a) 2 monolayers on the left and (b) 3 on the right. The presence of an intermediate fuzzy looking layer is indicative of non-sulfurized W metal or WO_2.

References

[1] R.G. Sumesh Sofin, Thesis, Trinity Colloge Dublin, Ireland, (2006).

[2] M. F. Craciun, S. Russo, M. Yamamoto, J. B. Oostinga, A. F. Morpurgo and S. Tarucha, Nat. Nano., 4 (2009) 383-388.

[3] W. Bao, L. Jing, J. Velasco, Y. Lee, G. Liu, D. Tran, B. Standley, M. Aykol, S.B. Cronin, D. Smirnov, M. Koshino, E. McCann, M. Bockrath, C.N. Lau, Nat Phys, 7 (2011) 948-952.

[4] C.H. Lui, Z. Li, Z. Chen, P.V. Klimov, L.E. Brus, T.F. Heinz, Nano Lett., 11 (2010) 164-169.

[5] C.H. Lui, Z. Li, K.F. Mak, E. Cappelluti, T.F. Heinz, Nat Phys, 7 (2011) 944-947.

[6] T. Taychatanapat, K. Watanabe, T. Taniguchi, P. Jarillo-Herrero, Nat Phys, 7 (2011) 621-625.

[7] F. Zhang, J. Jung, G.A. Fiete, Q. Niu, A.H. MacDonald, Phys. Rev. Lett., 106 (2011) 156801.

[8] L. Zhang, Y. Zhang, J. Camacho, M. Khodas, I. Zaliznyak, Nature Physis, 7 (2011) 953-957.

[9] E.V. Castro, Phys. Rev. Lett., 99 (2007) 216802.

[10] T. Ohta, A. Bostwick, T. Seyller, K. Horn, E. Rotenberg, Science, 313 (2006) 951-954.

[11] Y. Zhang, T.-T. Tang, C. Girit, Z. Hao, M.C. Martin, A. Zettl, M.F. Crommie, Y.R. Shen, F. Wang, Nature, 459 (2009) 820-823.

[12] K.F. Mak, C.H. Lui, J. Shan, T.F. Heinz, Phys. Rev. Lett., 102 (2009) 256405.

[13] J.B. Oostinga, H.B. Heersche, X. Liu, A.F. Morpurgo, L.M.K. Vandersypen, Nat Mater, 7 (2008) 151-157.

[14] F. Xia, D.B. Farmer, Y.-m. Lin, P. Avouris, Nano Lett., 10 (2010) 715-718.

[15] M. Aoki, H. Amawashi, Solid State Commun., 142 (2007) 123-127.

[16] A.A. Avetisyan, B. Partoens, F.M. Peeters, Phys. Rev. B, 80 (2009) 195401.

[17] A.A. Avetisyan, B. Partoens, F.M. Peeters, Phys. Rev. B, 79 (2009) 035421.

[18] K. Zou, F. Zhang, C. Clapp, A.H. MacDonald, J. Zhu, Nano Lett., 13 (2013) 369-373.

[19] P.Y. Huang, C.S. Ruiz-Vargas, A.M. van der Zande, W.S. Whitney, M.P. Levendorf, J.W. Kevek, S. Garg, J.S. Alden, C.J. Hustedt, Y. Zhu, J. Park, P.L. McEuen, D.A. Muller, Nature, 469 (2011) 389-392.

[20] K. Kim, Z. Lee, W. Regan, C. Kisielowski, M.F. Crommie, A. Zettl, ACS nano, 5 (2011) 2142-2146.

[21] V.Y. Aristov, G. Urbanik, K. Kummer, D.V. Vyalikh, O.V. Molodtsova, A.B. Preobrajenski, A.A. Zakharov, C. Hess, T. Hänke, B. Büchner, I. Vobornik, J. Fujii, G. Panaccione, Y.A. Ossipyan, M. Knupfer, Nano Lett., 10 (2010) 992-995.

[22] A. Chaika, O. Molodtsova, A. Zakharov, D. Marchenko, J. Sánchez-Barriga, A. Varykhalov, I. Shvets, V. Aristov, Nano Res., 6 (2013) 562-570.

[23] A.N. Chaika, O.V. Molodtsova, A.A. Zakharov, D. Marchenko, J. Sánchez-Barriga, A. Varykhalov, S.V. Babenkov, M. Portail, M. Zielinski, B.E. Murphy, S.A. Krasnikov, O. Lübben, I.V. Shvets, V.Y. Aristov, Nanotechnol., 25 (2014) 135605.

[24] A.W. Tsen, L. Brown, M.P. Levendorf, F. Ghahari, P.Y. Huang, R.W. Havener, C.S. Ruiz-Vargas, D.A. Muller, P. Kim, J. Park, Science, 336 (2012) 1143-1146.

[25] O.V. Yazyev, S.G. Louie, Nat Mater, 9 (2010) 806-809.

[26] A. H. Castro Neto, Guinea, F. Peres, N. M. R. Novoselov, K. S. Geim, A. K., Rev. Mod. Phys., 81, 109−162 (2009).

[27] K. F. Mak, K. L. He, J. Shan, T. F. Heinz, Nat. Nanotechnol., 7(8), 494−498 (2012).

[28] K. F. Mak, C. Lee, J. Hone, J. Shan and T. F. Heinz, Phys. Rev. Lett., 105, 136805 (2010).

[29] K. K. Kam, B. A. Parkinson J. Phys. Chem. B, 86, 463. (1982).

[30] B. Radisavljevic, A. Radenovic, J. Brivio, V. Giacometti, A. Kis, Nature Nanotech., 6, 147 (2011).

Appendix A

Resistive switching on NiO thin film

Stepped surfaces may play an important role in the soft breakdown of forming voltage. Current passing along and perpendicular to the steps, should result in anisotropic effects when creating conducting filaments in the NiO. Thus preventing the device from being damaged and require less forming voltage. When current passes along the steps it can be easier to create conducting filaments. This is due to different types of defects. If we can control the defect direction and densities it would be interesting not only in the field of resistive switching but also in the field of electronic engineering. It have been reported that filament formation in NiO took place in the gran boundaries of the thin film. Therefore, we report results of resistive switching on NiO grown on stepped MgO (100) substrates.

The NiO thin film was deposited on the stepped MgO substrate by an Edwards e-beam evaporating system and then post-annealed in air. Afterwards it has been characterized by AFM and SEM. Once it was characterized, contacts were deposited by using UV and EBL lithography and then I-V measurements were performed in a probe station.

In this section we used a vicinal 5° miscut MgO substrate as a template for the growth of the NiO thin film. The MgO substrate was annealed in the furnace at 1200°C for 3 hours in air in order to create terrace and step morphology on the surface. Once the sample was annealed, an AFM scan was carried out to observe the surface of the annealed substrate. Figure 1(a), shows an AFM image of the MgO substrate which was annealed at 1200°C for 3 hours. The periodicity of the annealed MgO substrate was calculated by using the AFM images. The periodicity and height of the MgO substrate were ~85 nm and ~7 nm respectively. Once we prepared a stepped surface on the vicinal MgO substrate, the NiO thin film was deposited on the stepped MgO surface. The Edwards e-beam evaporating system has been used to grow the NiO thin film from NiO pellets. The base pressure before the deposition was approximately 4.0×10^{-6} Torr. During the deposition the oxygen pressure inside the process chamber was between 2.5×10^{-5} Torr and 3.2×10^{-5} Torr, while the substrate temperature was maintained at room temperature (RT). The substrate was rotated during the deposition in order to achieve a homogeneous thin film. In the Edwards evaporating system we cannot heat the substrate holder, therefore we deposited at room temperature. The thickness of the film was monitored with the crystal balance and we deposited around 30 nm of NiO thin film. The surface morphology was examined by using an atomic force microscope (AFM). Figure 1(b) shows the NiO thin film deposited on the stepped MgO substrate.

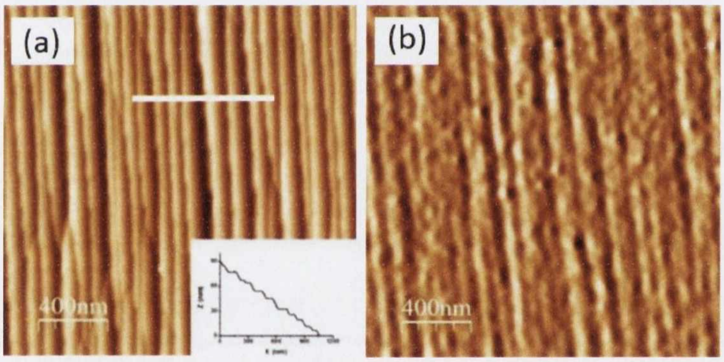

Figure 1 2x2 μm^2 size images of 5° miscut of MgO (110). (a) Vicinal MgO substrate annealed at 1200°C for 3 hours. (b) NiO thin film on stepped MgO substrate

The resistance of the sample deposited at room temperature was more than 200 MΩ. The sample was post annealed in the furnace for 1 hour at 400°C in air to observe any decrease in the resistance of the thin film. The resistance of the sample was measured with the probe station and we could see that annealing in air resulted in decreasing the resistance of the sample. The resistance of the sample was 25 MΩ. This was because of the low concentration nickel vacancies, and the fact the deposition was at low atmospheric pressure ($3.2\text{x}10^{-5}$ Torr). As we increased the oxygen content by annealing the sample in air, nickel vacancies increased which makes it a highly doped p-type semiconductor [1, 2] and the quality of the film increased which also resulted in the decrease of the resistance.

Figure 2 shows SEM images of Ag electrodes which were deposited on top of the NiO thin film. The electrodes were placed parrallel to electric field (a), and perpendicular to electric field (b). The width of electrodes was 500 nm and the gap between two electrodes was 180 nm.

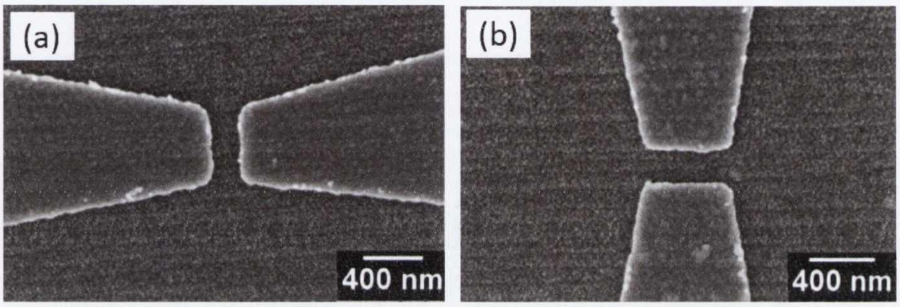

Figure 2 A SEM images of Ag electrodes on top of the NiO thin film (a) steps are parallel to the electric field (b) steps are perpendicular to the electric field.

Electrical measurement were carried out using a two probe method with a Keithley 2400 source meter. Two standard cables were plugged in the input/output sockets on the front side of the device and the end of the other side of the cable connected to the two tungsten probes mounted in a probe station. The two tungsten probes were connected, chosing the pads with 100×100 μm dimensions on the sample for the measurement. We prefered dc-voltage sweep measurements for the Ag/NiO/Ag contacts at room temperature. During the forming voltage, we limited the current to 2μA to avoid permanent damage of the samples.

Electric field applied perpendicular to the steps

As an activation process for resistive switching, a high electric field was needed for applying to the oxide material. Intitially we measured the electric forming process which was applied perpendicular to the steps testing eight devices (see Figure 3(a)). In order to activate the resistive switching in NiO, a high electric field was needed to apply to the oxide material to create a conducting filament. The process is crucial and in order to preserve the oxide material the maximum current which passes throuth the NiO film was limited. The current compliance was set to 2 μA, to prevent the device from the permenent breakdown. The dc voltage was applied and the current was measured.For all samples 120 V was applied and CC was set to 2 μA. From the I-V measurements we can see that the forming voltage are different and some of did not reach the compliance current. This means that during the application of the forming volatge all devices had not survived as shown in Figure 3(b). Only one SEM image was put here because all devices looked the same after the forming voltage. In the SEM image a big hole with a width of 100 nm is clearly seen and the electrodes and NiO thin film were destroyed after the forming voltage. None of these devices survived. Afterwards the electric field was applied parallel to the steps.

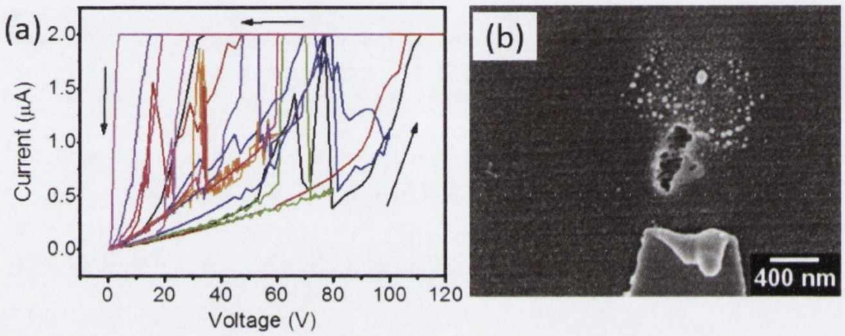

Figure 3 Forming voltage, electric field applied perpendiculat to the steps (a), SEM image after the forming voltage on one of the samples (b).

Electric field applied parallel to the steps

In this case, electric field was applied parallel to the steps in order to observe any difference in comparison to the electric field applied perpendicular to the steps. The same parameters were set as mentioned above, complaiance current set at 2 μA but the forming volatge was less than for the voltage applied perpendicular to the steps. Figure 4(a) shows the forming voltage for the electric field applied parallel to the steps. The initial resistance of the devices was around 30 MΩ before the forming voltage and once the conducting filament was created the resistance of the sample was 1 MΩ. Eight devices have been tested and all of them survived after the forming voltage. However the forming voltages were not as predicted, with forming voltages between 20-70 V. In Figure 4(b), we demonstrated the set voltage which is much less than the forming voltage. Once the sample was activated, it can be switched between set (LRS) and reset (HRS). However in Figure 4(b) we have demosntrated that only the set voltage was present at ± 5 V. This implies that the type of switching is unipolar, because the set and reset takes place at both polarities.

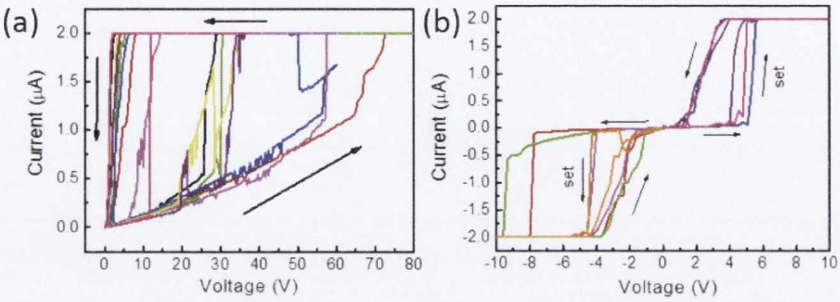

Figure 4 Forming voltage, electric field applied parallel to the steps (a), set voltage (b)

We found that steps plays an important role in the forming process. Electric field applied perpendicular to the steps showed that it was impossible to form conducting filament on the NiO film. Moreover, NiO thin film and electrodes have been destroyed after applying high electric field. However, when electric field was applied parallel to the steps, all of devices survived and the forming voltages were less. Using a stepped substrate as a template for the resistive switching mechanism we could see the anisotropic effect of the steps. In the future, we will use different step densities and demonstrate how much forming voltage is required to form the conducting filament and determine the influence of steps.

Appendix B

Resistive switching on stepped $SrTiO_3$ (100) substrate

We also tried to measure resistive switching on stepped $SrTiO_3$ substrates. First we will give a short description about how the sample was prepared for the electrical measurements. The vicinal 2° miscut sample of $SrTiO_3$ along the <010> direction have been used in this experiment. The sample has been annealed in the high temperature furnace at 1300°C for 3 hours in air. After thermal treatment, surface morphology have been examined by AFM and periodicity and height were ~78 nm and 3.1 nm respectively (see Figure 5(a)). Contact pads were fabricated through EBL and UV lithography technique. This is shown in the images in Figure 5(b, c) taken by SEM, where two terminal electrodes with gap widths of 280 nm and electrodes widths of 10 µm.

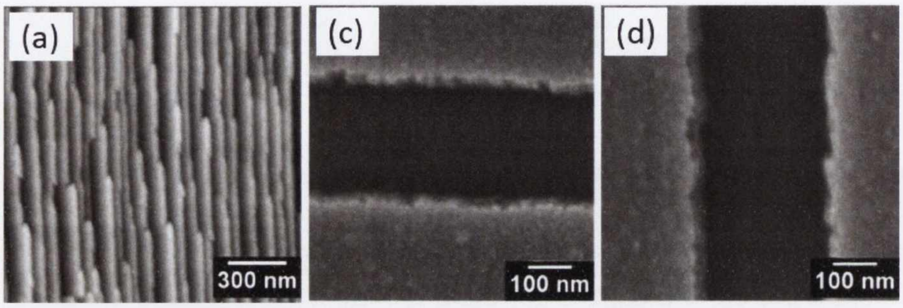

Figure 5 AFM image of vicinal $SrTiO_3$ after high temperature annealing. (a) SEM images of two terminal measurements where the electrodes were fabricated by EBL technique, and the electrodes were placed perpendicular to the steps (b) electrodes placed parallel to the steps (c).

Electrical measurements were performed at room temperature with the two probe method. High electric field was applied in order to form the initial conducting filament in the oxide material. High voltage was applied along the steps and perpendicular to the steps and no difference in voltage has been observed. The same voltage was required to activate the conducting filament. Once the conducting filament was activated, the resistance of the sample can be switched on and off by applying a voltage to the positive and negative polarity.

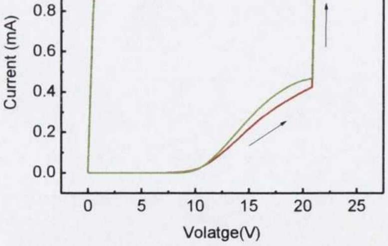

Figure 6 Forming of the conducting filament in $SrTiO_3$ where the electric field is applied perpendicular to the steps and parallel to the steps.

The resistance of the sample can be changed from high resistance to low resistance by connecting and rupturing the conducting filament. Resistive switching in $SrTiO_3$ is the bipolar type of switching where SET occurs in one polarity and RESET occurs in the other polarity. During SET the compliance current has to be set in order to prevent the sample from being destroyed, where in the RESET case compliance current can be removed. Figure 7(a, b) shows where a few cycles have been performed applying the electric field along the steps and the same for the perpendicular to the steps. However, after a few cycles resistive switching was not reproducible and the shape of the hysteresis became noisy. This is an indication that both the substrate and the electrodes have been destroyed.

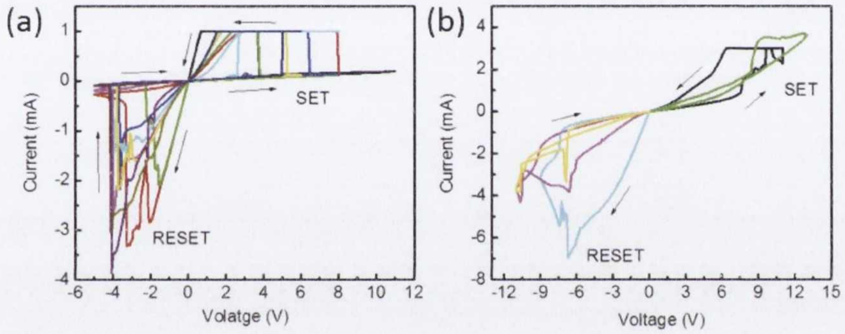

Figure 7 SET and RESET switching demonstrated by applying electric field along the steps (a) and perpendicular to the steps (b)

SEM images show that the electrodes and substrate itself were heavily damaged after a few I-V cycles. It is due to oxygen bubbles that are accumulated on the anode.

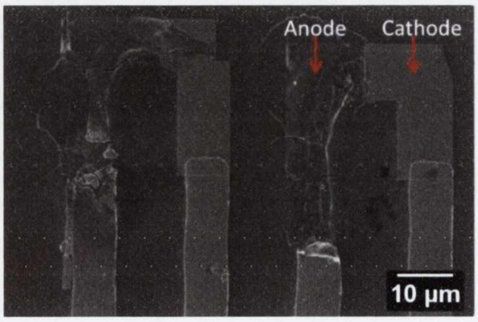

Figure 8 SEM images of the damaged electrodes after a few cycles

References

[1] S. Stanescu, C. Boeglin, A. Barbier, J.P. Deville, Phys. Rev. B, 67 (2003) 035419.

[2] S. Seo, M.J. Lee, D.H. Seo, E.J. Jeoung, D.-S. Suh, Y.S. Joung, I.K. Yoo, I.R. Hwang, S.H. Kim, I.S. Byun, J.-S. Kim, J.S. Choi, B.H. Park, Appl. Phys. Lett., 85 (2004) 5655-5657.